Stony Brook University

A Hydrodynamic Analysis of Collective Flow in Heavy-Ion Collisions

A Dissertation Presented

by

Li Yan

to

The Graduate School

in Partial Fulfillment of the Requirements

for the Degree of

Doctor of Philosophy

in

Physics

Stony Brook University

August 2013

Stony Brook University

The Graduate School

Li Yan

We, the dissertation committee for the above candidate for the Doctor of Philosophy degree, hereby recommend acceptance of this dissertation.

Derek Teaney – Dissertation Advisor
Professor, Department of Physics and Astronomy

Edward Shuryak – Chairperson of Defense
Professor, Department of Physics and Astronomy

Matthew Dawber
Professor, Department of Physics and Astronomy

Paul Sorensen
Physicist
Physics Department, BNL

This dissertation is accepted by the Graduate School.

Charles Taber
Interim Dean of the Graduate School

Abstract of the Dissertation

A Hydrodynamic Analysis of Collective Flow in Heavy-Ion Collisions

by

Li Yan

Doctor of Philosophy

in

Physics

Stony Brook University

2013

Recent progress in the hydrodynamic simulation of heavy-ion collisions have characterized the fluctuating initial state and the viscous corrections to the corresponding collective flow. These fluctuations naturally explain the "ridge" and "shoulder" structure of the measured two-particle correlation functions at RHIC and the LHC.

We introduce a cumulant expansion for analyzing the azimuthal fluctuations in the initial state. The cumulant definitions systematically describe the azimuthal anisotropy order by order. In particular, the dipole asymmetry ϵ_1 appears at third order in the expansion, and the response to this initial fluctuation produces a radipity even dipole flow v_1, which has been subsequently confirmed by experiment.

In addition, the cumulant expansion organizes the study of the nonlinear response to the initial conditions. The linear and nonlinear response coefficients to a given initial state were calculated with ideal and viscous hydrodynamic simulations. The collective

flow is generated either linearly or nonlinearly, and the relative contribution of these two mechanisms to the observed flow pattern is calculated as a function of harmonic order, collision centrality, and the shear viscosity. For non-central collisions and high harmonic orders $n \geq 4$, the nonlinear response is the dominant mechanism. This result is also seen in event-by-event hydrodynamic simulations. Using the cumulant expansion and the corresponding linear and nonlinear response coefficients, we determine the event plane correlations and compare to first measurements of this type. The observed event plane correlations are rooted in the initial state participant plane correlations, but a large fraction of the observed correlations are determined by harmonic mixing during the bulk expansion.

Viscous corrections to the hydrodynamic formulation of collective flow are reflected in hydrodynamic equations of motion, as well as the correction to the distribution function at freeze-out, $\delta f(x, \boldsymbol{p})$. Taking into consideration of the connection between kinetic theory and hydrodynamics, the consistent form of $\delta f(x, \boldsymbol{p})$ is determined through second order in the gradient expansion, $\delta f(x, \boldsymbol{p}) = \delta f_{(1)}(x, \boldsymbol{p}) + \delta f_{(2)}(x, \boldsymbol{p}) + \dots$. The effect of $\delta f_{(2)}(x, \boldsymbol{p})$ is found to be small for lower order harmonic flows $n \leq 3$, but is significant for the higher harmonics, $n \geq 4$. In addition, the effect of $\delta f_{(2)}(x, \boldsymbol{p})$ is small for nucleus-nucleus collisions at the LHC, but is more pronounced at RHIC and in small collision systems such as proton-nucleus collisions. $\delta f_{(2)}(x, \boldsymbol{p})$ delineates the domain of applicability of viscous hydrodynamics, and systematically improves the hydrodynamic description of heavy ion collisions.

Contents

List of Figures vii

List of Tables x

Acknowledgements xi

1 Introduction 1
- 1.1 QCD under extreme conditions . . . 1
- 1.2 QGP in heavy-ion collisions . . . 2
- 1.3 Hydrodynamics and QGP . . . 8
  - 1.3.1 Initial condition . . . 9
  - 1.3.2 Hydrodynamic description of the hot medium . . . 11
  - 1.3.3 Freeze-out and resonance decay . . . 18
- 1.4 Outline of this work . . . 19

2 Fluctuations in the initial state 21
- 2.1 Cumulant expansion . . . 24
- 2.2 Application of cumulant expansion . . . 29
- 2.3 Monte Carlo simulations of the initial state . . . 32

3 Flow response 43
- 3.1 Linear flow response . . . 44
  - 3.1.1 Flow development during the medium expansion . . . 45
  - 3.1.2 Linear flow response coefficients . . . 49
  - 3.1.3 Application of linear flow response . . . 53
- 3.2 Nonlinear flow response . . . 57
  - 3.2.1 Nonlinear flow response coefficients . . . 59
  - 3.2.2 Origins of the nonlinear flow generation . . . 63
  - 3.2.3 Application of the nonlinear flow generation . . . 67
- 3.3 Discussion . . . 73

4 Event plane correlations **75**
4.1 Formulation of event plane correlations 76
4.2 Predictions 78
4.3 Discussion 82

5 Second order viscous corrections, $\delta f_{(2)}$ **86**
5.1 2nd order corrections to $f(x, \boldsymbol{p})$ 88
5.1.1 Hydrodynamics 88
5.1.2 Kinetics 89
5.2 Implementation in simulations of heavy ion collisions 94
5.3 Discussion 98

6 Conclusions and outlook **103**

A Notations and conventions **106**

B 3-dimensional cumulant analysis **108**

C Tensor decomposition of $\delta f_{(2)}$ **110**

D Convergence check of viscous hydrodynamic simulations **113**

Bibliography **115**

List of Figures

1.1 A schematic QCD phase diagram taken from [1]. 2
1.2 Space-time evolution of a heavy-ion collision with QGP phase 3
1.3 A summary of the measured nuclear modification factor R_{AA} of charged hadrons from LHC Pb-Pb. [2] 5
1.4 Initial geometric configuration of heavy-ion collisions. 6
1.5 A comparison of the observed harmonic flow of mid-central heavy-ion collisions from different collaborations [3]. 7
1.6 A summary of the theoretical estimates of η/s. Figures taken from [4]. 9
1.7 A fit of charged particle multiplicity from viscous hydrodynamic simulations with the initial parameter C_s taken in Table 1.1, with respect the ALICE measurement [5]. 12
1.8 A summary of lattice EoS. Figures taken from [6]. 14

2.1 The fluctuating initial state of one typical collision event, for the event-by-event hydrodynamic simulations. The blue arrows indicate the direction and magnitude of gradients. 22
2.2 Decomposition of the fluctuating initial state into Gaussian background plus perturbations. 24
2.3 A schematic picture of the dipole asymmetry. 28
2.4 (a) Spectra in the smooth (optical) Glauber model compared to the cumulant expansion. The coefficients of the Gaussian and fourth-order cumulant expansions have been adjusted to reproduce $\{r^2\}$, $\{r^2\cos 2\phi_r\}$ and $\{r^4\cos 2\phi_r\}$, $\{r^4\cos 4\phi_r\}$, respectively. The total entropy of the cumulant expansion is also matched to the total entropy of the Glauber distribution. (b) Elliptic flow in the Glauber model compared to the cumulant expansion. 31

2.5 Eccentricities from Monte Carlo Glauber simulations for LHC Pb-Pb collisions. The momentum based (the left figure) and the cumulant based (the right figure) definitions result in differences that grows with centrality, for the higher order eccentricities. . 33
2.6 Distribution of the angles Φ_1 and Φ_3 with respect to the reaction plane for three different impact parameters 34
2.7 Initial participant plane correlation functions, from MC-Glaber simulations for RHIC Au-Au collisions. 35
2.8 Geometric alignment of triangularity, dipole and ellipticity . . 36
2.9 The conditional probability distribution $P(\Phi_3|\Phi_1, \Psi_R)$ for impact parameter $b = 10.5$ fm. The dashed curves are fit with parameter $C_2 = -0.53$. 38
2.10 Initial state two-plane correlations of LHC Pb-Pb collisions . . 39
2.11 Initial state three-plane correlations of LHC Pb-Pb. 40

3.1 (a) The spatial anisotropy of the entropy distribution ϵ_{1x} , ϵ_{2x} , and ϵ_{3x} (see text) as a function of time for $b = 7.6$ fm. (b) The momentum anisotropy ϵ_{1p}, ϵ_{2p} , and ϵ_{3p} (see text) as a function of time. The time scale in these figures should be compared to $\sqrt{\{r^2\}}/c_s \simeq 5.4$ fm. 47
3.2 Flow profile evolution 48
3.3 p_T dependence of linear response coefficients. 50
3.4 Centrality dependence of linear response coefficients 51
3.5 Linear flow response dependence on η/s 52
3.6 $V_{3\Delta}/V_{2\Delta}$ and $V_{1\Delta}/V_{2\Delta}$ as a function of N_{part}. 54
3.7 $\langle\langle\cos(\phi_a + \phi_b - 2\Psi_R)\rangle\rangle$ from hydrodynamic simulation. 55
3.8 Differential $\langle\cos(\phi_a - 3\phi_b + 2\Psi_R)\rangle$ of mid-central collisions. . . 56
3.9 Angle dependence of nonlinear flow response coefficients. . . . 60
3.10 p_T dependence of nonlinear flow response coefficients. 61
3.11 Centrality dependence of nonlinear flow response coefficients . 62
3.12 Nonlinear flow response dependence on η/s 63
3.13 Participant plane angle time evolution 64
3.14 $v_n\{2\}$ as a function of centrality. 69
3.15 $v_1\{2\}(p_T)$ of mid-central collisions of LHC Pb-Pb experiments 71
3.16 Scaling behavior of v_4 and v_5 72

4.1 Two-plane event plane correlations. The solid curves are the predictions based on a high resolution assumption. The dashed curves are obtained in the low resolution limit. Data points are taken from the ATLAS measurements [7]. 79

4.2 Three-plane event plane correlations. The solid curves are the predictions based on a high resolution assumption. The dashed curves are obtained in the low resolution limit. Data points are taken from the ATLAS measurements [7]. 80
4.3 Decomposition of the event-plane correlations into the 'linear limit' and 'nonlinear limit', corresponding to the formation of event-plane correlations from initial geometry and medium expansion. 81
4.4 Two-plane event plane correlations based on PHOBOS Glauber [8] and Glissando Glauber [9] models. The solid curves correspond to the 'non-cut' calculations, while the dashed curves correspond to the 'cut' calculations. (See text) 83
4.5 Three-plane event plane correlations based on PHOBOS Glauber [8] and Glissando Glauber [9] models. The solid curves correspond to the 'non-cut' calculations, while the dashed curves correspond to the 'cut' calculations. (See text) 84

5.1 $w_4(p_T)$ and $w_{4(22)}(p_T)$ from hydrodynamics with different η/s. 87
5.2 Differential $v_2(p_T)/\epsilon_2$ at RHIC and LHC, with CEOS and LEOS 100
5.3 Differential v_n/ϵ_n at RHIC and LHC 101
5.4 Differential v_n/ϵ_n at RHIC and LHC 102

D.1 Convergence of harmonic flow v_5 and v_6 in our numerical calculations. The grid sizes are set to be 0.1 fm, 0.075 fm and 0.05 fm for these three simulations. While v_n^c tends to converge (the left figure), the v_n^s approaches zero (the right figure). 113

List of Tables

1.1 Parameter C_s used in our work for LHC Pb-Pb collisions. . . . 11

3.1 Nonlinear terms considered in this work 59
3.2 Geometrical ratios in Eq. (3.34) as a function of centrality. . . 73

5.1 Second order transport coefficients 96

Acknowledgements

First and foremost I would like to express my sincere gratitude to my advisor Prof. Derek Teaney, for his thoughtful guidance during my Ph.D study and research. My research work with him during the past several years was a great experience. Without his patience, encouragement and continuous support this dissertation would not have been possible. I have greatly benefited from his enthusiasm for physics and lightening ideas. I also want to thank him for providing me with all these opportunities to broaden my horizons in the area of heavy-ion collisions.

I am also indebted to all the rest of members in the nuclear theory group. The instructive discussions during lunch time, group seminars and under many other circumstances, with Edward Shuryak, Ismail Zahed, Dmitri Kharzeev Jacobus Verbaarschot and Thomas Kuo enriched my knowledge and sharpened my understanding on physics in general. In particular, I would like to thank Edward Shuryak and Dmitri Kharzeev for their help for writing me the reference letters. I am also grateful to the interesting and helpful discussions with Gokce Basar and Ho-Ung Yee. I also want to thank the other graduate students Alexander Stoffers, Savvas Zafeiropoulos, Pilar Staig and Frasher Loshaj for the enjoyable working atmosphere in the office. I also want to thank the former graduate students Huan Dong, Shu Lin and especially Jinfeng Liao for their warm-hearted help.

For the work covered in this thesis, I gratefully acknowledge the fruitful and enlightening discussions with J. Jia, S. Mohapatra, U. Heinz, Z. Qiu, J. Ollitrault, P. Sorensen and K. Dusling.

I also want to take this chance to thank Nu Xu and my M. S. thesis advisors Prof. Pengfei Zhuang, who gave me the early scientific training and advices.

Finally and most importantly, I would like to thank my family, my wife Ruhan Jia and my parents for their unconditional love and support.

Chapter 1

Introduction

1.1 QCD under extreme conditions

Quantum Chromodynamics(QCD), which is responsible for the description of strong interaction in standard model, has particular properties regarding the associated energy scale Λ. In contrast to the electroweak theory, the coupling constant of the strong interaction α_s monotonically decreases as the momentum scale of the measurement, Λ increase. Especially, when the momentum scale of the measurement is large, $\Lambda \gg \Lambda_{\mathrm{QCD}}$, QCD exhibits asymptotic freedom [10, 11], and the dynamics of QCD is conveniently described with weakly coupled color degrees of freedom, quark and gluons. Asymptotic freedom has been extensively tested and analyzed in collisions of elementary particles [12]. For instance, asymptotic freedom can be confirmed with the Bjorken scaling observed in the deep inelastic scattering [13]. In the opposite low energy limit, QCD exhibits infrared slavery which states that color degrees of freedom must be confined in low energy processes. Despite the apparent consistency of QCD with high energy experiments, isolated colored particles have never been found experimentally, and the theoretical treatment of color confinement is difficult. The problem is that the running coupling constant becomes of order one, deteriorating the applicability of perturbative calculations. Consequently, many effective theoretical models and non-perturbative techniques have been developed, such as chiral perturbation theory [14] and Lattice QCD (LQCD) [15]. Nevertheless, the existence of these two distinct limits in QCD dynamics implies a complex transition region at some intermediate energy scale Λ_c, in which color degrees of freedom are excited and begin to dominate the constituents of a system. This transition, commonly known as the color deconfinement phase transition, is one of the central interests in the present studies of nuclear physics.

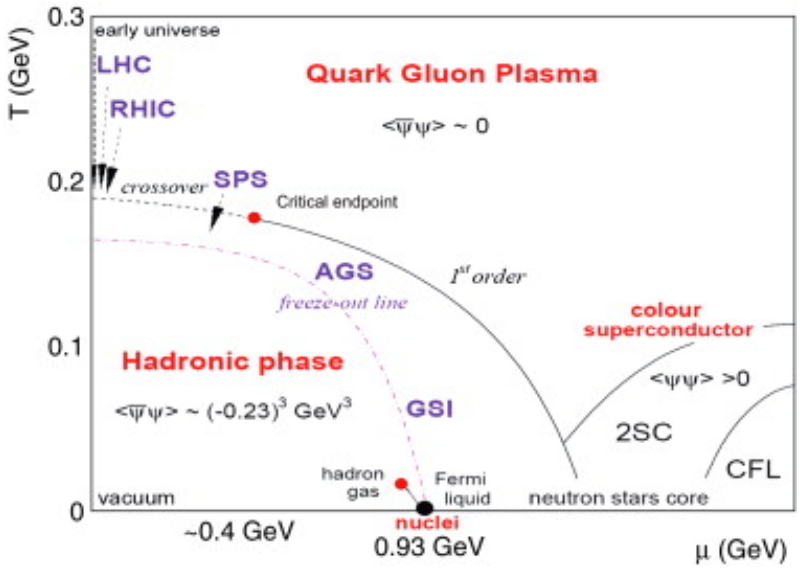

Figure 1.1: A schematic QCD phase diagram taken from [1].

In Fig. 1.1, the appropriate energy scale is set by the temperature T or baryon chemical potential μ_b. An overall review of the recent theoretical work on the QCD phase diagram can be found, for example in [16]. Starting from the ordinary hadronic matter, increasing either temperature or baryon chemical potential will eventually lead the system to phases with pure color degrees of freedom, *e. g.* color superconductor [17] and Quark-Gluon Plasma(QGP) [18]. The former phase is expected when baryon chemical potential μ_b exceeds a critical value μ_b^c. The latter phase prevails in systems with extremely high temperature. In particular, with negligible baryon chemical potential $\mu_b \sim 0$, LQCD simulations have confirmed the existence of a rapid crossover instead of a first phase transition, between QGP and the hadron gas at $T_c \simeq 170$MeV [19]. This high temperature existed in nature in the first second of the early universe [20], during which the temperature of QGP cooled down to T_c and colorless matter was originated through hadronization.

1.2 QGP in heavy-ion collisions

High energy nucleus-nucleus(AA) collisions carried out at Relativistic Heavy-Ion Collider (RHIC) at Brookhaven National Laboratory [21–24], and Large Hadron Collider (LHC) at CERN [25], provide an opportunity to create QGP in the laboratory. In heavy-ion collisions, highly accelerated heavy nucleus

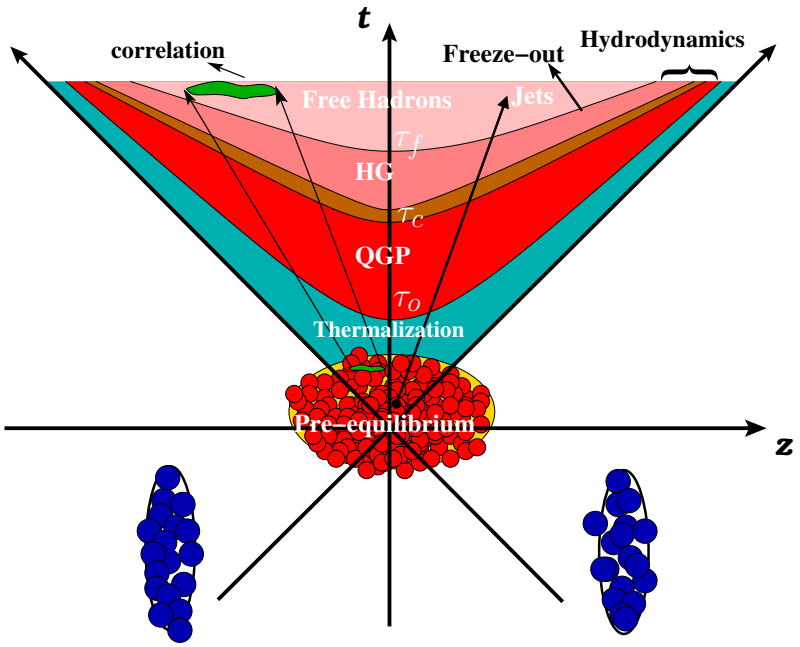

Figure 1.2: Space-time evolution of a heavy-ion collision with QGP phase

deposit a large fraction of their energy in a small volume, generating a system with pronounced energy density. Although there is no direct measurement associated to the initial stage of such a system, evidences from experimental observations strongly indicate that an approximately thermal QGP is formed in heavy ion events with an estimated initial temperature $T_o \simeq 320\,\mathrm{MeV}$. Since $T_o > T_c$, the first several fm/c of the created fireball is in the QGP phase. During subsequent expansion of the fireball the plasma cools and passes through the color confinement transition. Since this expansion resembles in many ways the evolution of the early universe (see for example Chapter 19 in [26]), the nucleus-nucleus collision is commonly referred to as the 'little bang'.

Fig. 1.2 illustrates the collision process for one typical event in space and time. Note that in this figure, Bjorken boost invariance [27] of the high energy collision is assumed. As a convenient and reliable approximation for heavy-ion collisions, Bjorken boost invariance simplifies the relativistic transformation along the longitudinal direction, leading to a trivial dependence on the spatial rapidity,

$$\eta_s = \frac{1}{2}\ln\left(\frac{t+z}{t-z}\right) . \tag{1.1}$$

Correspondingly the proper time is defined as

$$\tau = \sqrt{t^2 - z^2}\,, \tag{1.2}$$

which separates the stages of the space-time evolution in Fig. 1.2. In this figure τ_o indicates when the pre-equilibrium state ends (*i. e.* when the thermodynamic variables are well defined). The temperature of the system decreases as a result of the medium expansion. When T reaches the critical temperature around τ_c, the hot medium experiences color confinement phase transition and hadronizes, changing from the QGP phase to a hadron gas (HG). In the HG, the collectivity of the medium can be sustained due to the interactions between the stable and unstable hadrons, and hadron resonances. However, as the expansion overwhelms the hadron-hadron correlations around τ_f, the dilute HG system starts to decouple. This so-called kinetic freeze-out is generally recognized as the end of the collective expansion. In general, the whole evolution of the collision event in heavy-ion collisions is expected to take from several fm/c to about 10 fm/c.

Many observables of have been proposed to understand the evolution of the QGP and the HG discussed in the previous paragraph. The most successful observables can roughly be divided into hard probes and soft probes, both of which have particular connections to the dynamics of the QGP medium.

Hard probes

Hard probes, including jets [28] and heavy flavor production [29], are modified by their strong interactions with the QGP medium.

For instance, since jets are generated in the initial hard processes of heavy-ion collisions, energetic jets undergo energy loss in QGP before they are measured. As a result, the interactions between jets and the QGP can be studied by comparing jet yields in AA collisions and the corresponding PP collisions. The nuclear modification factor $R_{\rm AA}$ is formally defined as

$$R_{\rm AA}(p_T) \sim \frac{\text{Spectrum of AA}}{\text{Spectrum of PP}},$$

with proper normalizations. $R_{\rm AA} < 1$ indicates that the jets lost energy to the QGP medium. Shown in Fig. 1.3 is a summary of the nuclear modification factor $R_{\rm AA}$ of inclusive charged hadrons observed from LHC Pb-Pb collisions. In central collisions, from which QGP is formed with high probability, the spectra of the observed hadrons are found to be strongly suppressed. Especially the energy loss of particles with high transverse momentum ($\gtrsim 6$ GeV) implies the dynamics of jets penetrating the QGP.

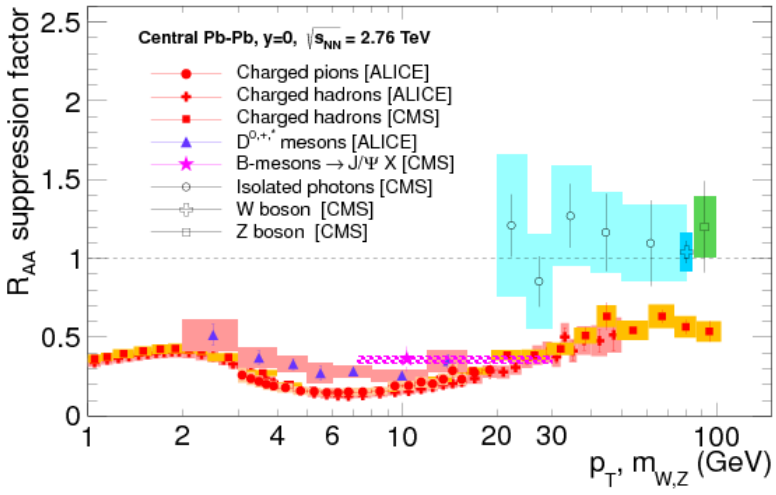

Figure 1.3: A summary of the measured nuclear modification factor R_{AA} of charged hadrons from LHC Pb-Pb. [2]

Soft probes

Soft probes such as the collective flow [30, 31] which is the major subject of this dissertation, characterizes the bulk collective expansion, with respect to a specified initial geometry.

Fig. 1.4 illustrates the initial state geometric configuration generally seen in heavy-ion collisions. The beam axis, along which the two nuclei move and collide, is conventionally set as the z-direction. The plane perpendicular to the beam axis is known as the transverse plane. Viewed along the beam axis, the collision of two nuclei in the transverse plane is referred as the overlap region.

The size of the overlap region is crucial for the analysis of heavy-ion collision. First, since more initial energy is deposited in the collision event with a larger overlap region, a higher initial temperature T_o and a larger measured multiplicity are expected. In addition, the size of the overlap region is related to the AA collision probability. To describe the collision geometry the impact parameter $\boldsymbol{b}$ is commonly introduced. Set as the x-direction as in Fig. 1.4, $\boldsymbol{b}$ is a vector that measures the displacement of the centers of the two colliding nuclei in the transverse plane, pointing from one to the other. Then the differential collision cross-section can be roughly estimated as $d\sigma = 2\pi|\boldsymbol{b}|d|\boldsymbol{b}|$. In experiment, accounting for a distribution of the observed multiplicity production of different collision events, a quantity called centrality can be introduced instead. There is an one-to-one, and monotonic correspondence between $\boldsymbol{b}$ and

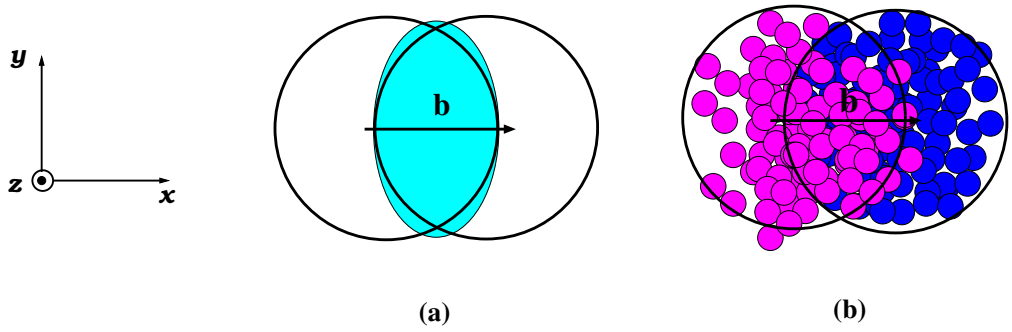

Figure 1.4: Initial geometric configuration of heavy-ion collisions.
The smooth initial geometry (a) and the initial geometry with fluctuations (b). In (b), the nucleons from the target and projectile are distinguished in different colors.

the centrality, that $\boldsymbol{b} = 0$ is related to centrality = 0% and $|\boldsymbol{b}| \to \infty$ is related to centrality= 100%.

The beam axis and $\boldsymbol{b}$ span the reaction plane Ψ_R, [1] The reflection symmetry of a smooth initial geometry as in Fig. 1.4 (a), with respect to x-axis and y-axis as a result of the almond shape, is broken due to fluctuations in a random event as in Fig. 1.4 (b). The azimuthally asymmetric distribution leads to initial spatial gradients. During bulk expansion, information of initial spatial distribution is translated into momentum space due to these gradients, and collective correlations are developed. In particular, the azimuthal anisotropies of initial state generate anisotropic flow, v_n. Formally the definition of v_n is from the harmonic decomposition of the observed particle spectrum,

$$\frac{d^3N}{p_T dp_T d\phi_p d\mathrm{y}} = \frac{dN}{2\pi p_T dp_T d\mathrm{y}} \left[1 + \sum_{n=1}^{\infty} v_n(\mathrm{y}, p_T) e^{in(\phi_p - \Psi_n(\mathrm{y}, p_T))} + c.c. \right] , \quad (1.3)$$

where here and below *c.c.* denotes complex conjugate. $p_T = \sqrt{p_x^2 + p_y^2}$ is the transverse momentum. For the convenience of considering Bjorken boost invariance, the rapidity

$$\mathrm{y} = \frac{1}{2} \ln \left(\frac{E + p_z}{E - p_z} \right) , \quad (1.4)$$

[1] Without considering initial state fluctuations, *i. e.* for the event averaged smooth initial density, only even order harmonics in the particle spectrum can be expected. In particular, the observed elliptic flow v_2 defines the reaction plane Ψ_R, which reflects the almond shape of initial geometry.

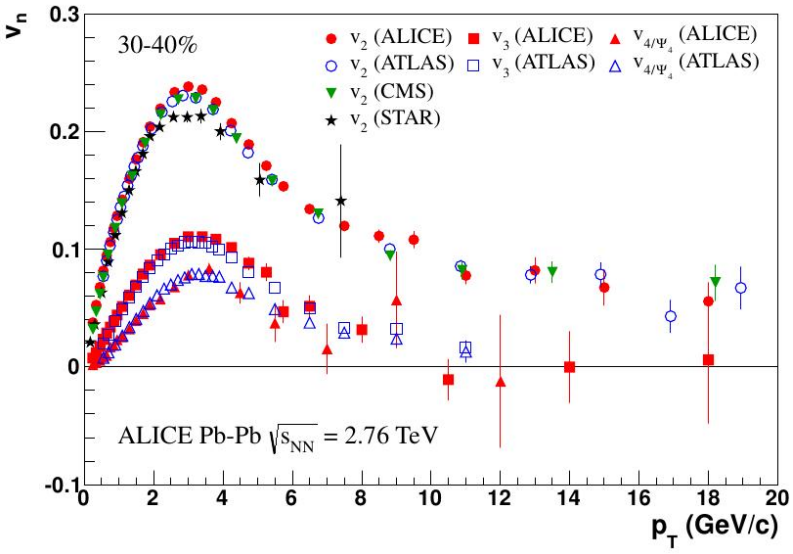

Figure 1.5: A comparison of the observed harmonic flow of mid-central heavy-ion collisions from different collaborations [3].

is often used instead of p_z. In Eq. (1.3), v_n can be experimentally measured as the expectation $v_n = \langle \cos(n\phi_p - n\Psi_n) \rangle$, with respect to the associated event plane angle Ψ_n of n-th order harmonics. The angle brackets around a scalar indicates the averaged value with respect to the particle spectrum. v_n characterizes the azimuthal anisotropy of particle spectrum in the momentum space. For instance, elliptic flow, $v_2(\mathrm{y}, p_T)$ estimates the differences of particle yields between in-plane direction ($\phi_p - \Psi_2(\mathrm{y}, p_T) = 0$) and out-of-plane direction ($\phi_p - \Psi_2(\mathrm{y}, p_T) = \pi/2$). When reflection symmetry of the system is strict, the odd order harmonics in Eq. (1.3) are zero by symmetry, and the event plane angles are aligned trivially with $\Psi_n(\mathrm{y}, p_T) = 0$. However, on an event-by-event basis the initial geometry is perturbed by fluctuations, resulting in an actual entropy initial distribution as shown in Fig. 1.4 (b). As a result, in Eq. (1.3) all of the harmonic orders should be expected. Fig. 1.5 exhibits the measured elliptic flow v_2, triangular flow v_3 and quadrapole flow v_4 from several collaborations from a set of selected collision events at RHIC and LHC [3]. Note that the observed flow in the low p_T region ($p_T \lesssim 3$GeV) in Fig. 1.5 is expected to be dominated by the collective behavior of the bulk expansion.

There are several aspects related to harmonic flow v_n that supports the existence of QGP phase in heavy-ion collisions. First, the QGP phase plays an essential role in the establishment of harmonic flow. Based on the analyses of theoretical models, such as relativistic hydrodynamics and transport theory, to

obtain harmonic flow predictions comparable to the experimental observations, especially for higher order harmonic flow v_3, v_4, *etc.*, a strong QGP expansion is indispensable [32, 33]. In addition, the observed long range correlations in AA from RHIC Au-Au [34–36] and LHC Pb-Pb [37, 38], and even some pA collisions with high multiplicity yields [39, 40], can be naturally explained in terms of harmonic flow. As sketched in Fig. 1.2, the harmonic flow is the medium response to the initial geometry and is generated during the bulk expansion. Since the initial correlation is long range in rapidity, this correlation is maintained from the earliest stages of the event to the final observation.

1.3 Hydrodynamics and QGP

The relative success of relativistic hydrodynamics with vanishing shear viscosity in predicting the elliptic flow [41–45] indicates that the mean free path of the QGP is small compared to the expansion time scales of the nuclear collision. An estimate of the expansion rate and the temperature [46] shows that unless the mean free path is comparable to a thermal wavelength $\sim \hbar c/T$ then expansion will be to rapid to support a strong hydrodynamic response.

The qualitative success of ideal hydrodynamics motivates further experimental and theoretical study of the transport properties of QCD. In particular, the determination of shear viscosity to entropy density ratio η/s of the color deconfined medium in heavy-ion collisions, supplies a direct measurement of the fundamental property of QCD at high temperature. In hydrodynamics, dissipation is characterized via a number of transport coefficients. Most importantly, shear viscosity η is associated with the shear tensor of the first viscous correction. As input parameters of hydrodynamics, these transport coefficients are constrained by the underlying fundamental theory [46]. For a strongly coupled colorful system, like QGP, there is no analytical solution in QCD, but it is possible to estimate the corresponding transport coefficients using lattice QCD [47], and other model theories. For instance, the shear viscosity of $\mathcal{N} = 4$ SYM at strong coupling was calculated using gauge gravity duality [48],

$$\frac{\eta}{s} = \frac{1}{4\pi}\frac{\hbar}{k_B}. \tag{1.5}$$

Kovtun, Son and Starinets suggest that Eq. (1.5) is a lower bound of η/s for a variety of theories, including QCD, and thus Eq. (1.5) is often referred as the KSS bound [49]. A summary of the possible values of η/s as a function of temperature for a variety of different models is shown in Fig. 1.6. To get

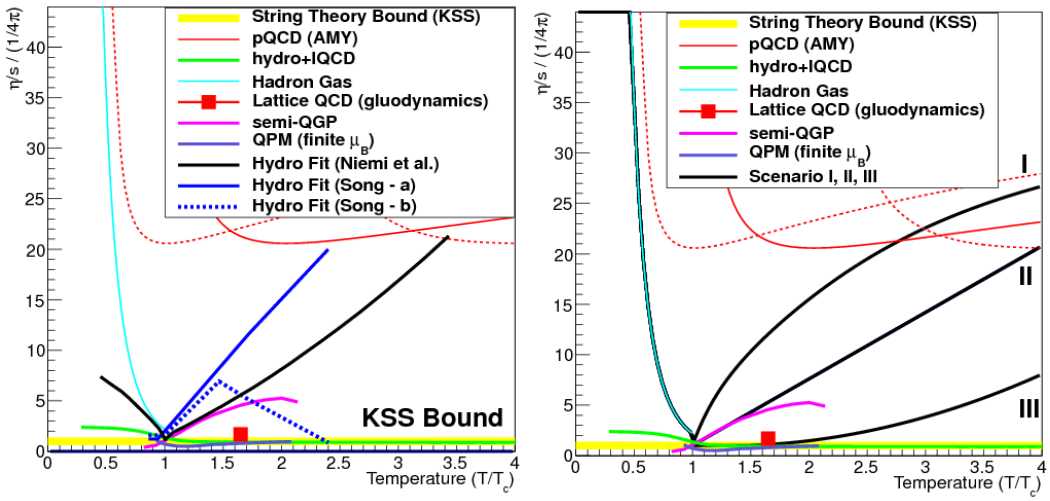

Figure 1.6: A summary of the theoretical estimates of η/s. Figures taken from [4].

a further understanding of QCD dynamics, and a quantitative estimate η/s of QGP, one needs serious viscous hydrodynamic simulations of heavy-ion collisions.

Examining the stages of a heavy ion collision shown in Fig. 1.2, we see that a complete hydrodynamic simulation for a collision event consists the following three ingredients: initial condition, hydrodynamic equations of motion, and freeze-out. The conventions and notations used in this following section are summarized in Appendix A.

1.3.1 Initial condition

To initialize the hydrodynamic equations of motion, the energy density and flow velocities must be specified at an initial time τ_o. However, due to the lack of knowledge of the bulk thermalization, detailed information, such as the initial energy density $\epsilon(\tau_o, x, y)$ and entropy density $s(\tau_o, x, y)$, has to be deduced from effective models. Two models which are commonly used to estimate the initial energy density are the Glauber model [8] and the KLN model [50–52]. We will briefly review the Glauber model in this section.

The Glauber model takes into account the nuclear geometry and the straight line propagation of nucleons in high energy collisions. Since the nucleons are

distributed in the nucleus according to the Woods-Saxon profile,

$$\rho(\boldsymbol{x}) = \frac{\rho_o}{1+\exp[(r-R)/a]}\,, \tag{1.6}$$

the collision probability and total cross section can be inferred by geometry. In Eq. (1.6) the parameters ρ_o, R, and a characterize the normalization, the size of the nucleus, and the stiffness of the edge of nucleon distribution profile respectively. The probability density of finding a nucleon in a nucleus in the transverse plane at $s = (x, y)$ is known as the thickness function

$$\hat{T}_A(\boldsymbol{s}) = \int_{-\infty}^{+\infty} dz \rho(\boldsymbol{s}, z)\,. \tag{1.7}$$

Given the thickness function we obtain

$$\sigma_{\rm in}^{\rm NN} T_{AB}(x, y|\boldsymbol{b}) = \sigma_{\rm in}^{\rm NN} \hat{T}_A(\boldsymbol{s}) \hat{T}_B(\boldsymbol{s}-\boldsymbol{b})\,, \tag{1.8}$$

which is the probability per area of finding a nucleon-nucleon collision at the transverse position $\boldsymbol{s}$ of the overlap region for a nucleus-nucleus collision with impact parameter $\boldsymbol{b}$. For hard collision process, the number of collisions, $N_{\rm coll}(x, y)$, which counts the number of nucleon-nucleon collisions in each AA collision event, is introduced. By contrast, the number of participants $N_{\rm part}(x, y)$, records the number of nucleons that are involved in the collisions, characterizes the soft processes. It is also known as the number of wounded nucleons. Both $N_{\rm coll}$ and $N_{\rm part}$ can be used to characterize the collision centrality. Then in the Glauber model, with the inclusive nucleon-nucleon cross-section $\sigma_{\rm in}^{\rm NN}$, we obtain for a collision between two nuclei with mass number A and B,

$$N_{\rm coll}(x, y|\boldsymbol{b}) = \sigma_{\rm in}^{\rm NN} AB T_{AB}(x, y|\boldsymbol{b}) \tag{1.9}$$

and

$$\begin{aligned} N_{\rm part}(x, y|\boldsymbol{b}) =& A\hat{T}_A(\boldsymbol{s}) \left\{1 - \left[1 - \sigma_{\rm in}^{\rm NN} \hat{T}_B(\boldsymbol{s}-\boldsymbol{b})\right]^B\right\} \\ &+ B\hat{T}_B(\boldsymbol{s}-\boldsymbol{b}) \left\{1 - \left[1 - \sigma_{\rm in}^{\rm NN} \hat{T}_A(\boldsymbol{s})\right]^A\right\}\,. \end{aligned} \tag{1.10}$$

In our calculations, for the RHIC and LHC collision energy, $\sigma_{\rm in}^{\rm NN}$ is taken to be 40mb and 64mb respectively.

For the thermalized system at τ_o, entropy density in the transverse plane

Table 1.1: Parameter C_s used in our work for LHC Pb-Pb collisions.

$b_{\rm imp}$(fm)	1.65	4.00	5.25	6.25	7.45	8.80	10.00	11.10
$C_s/N_{\rm part}$	34.97	33.84	32.88	32.15	31.75	31.72	31.59	31.30

can be emperically assumed as

$$s(\tau_o, x, y) = \frac{C_s}{\tau_o} \left[\alpha N_{\rm coll}(x, y) + (1 - \alpha) N_{\rm part}(x, y)\right] , \tag{1.11}$$

in which the free parameter α is taken to constrain the faction of contributions from hard and soft processes, and C_s is a normalization constant. To fit the observed data from experiment, both α and C_s can be adjusted. In our work, we take $\alpha = 0$ to consider only soft process initial contribution, and vary C_s for different centralities. With C_s taken according to the values in Table 1.1, the charged multiplicity $dN_{ch}/d\eta/(N_{\rm part}/2)$ of LHC Pb-Pb collision with $\sqrt{s_{\rm NN}} = 2.76$TeV [5] is reproduced by our viscous hydrodynamic simulations, in combination with with a resonance decay description.

As one recent progress in heavy-ion collisions, and also one subject in our work, fluctuations in initial state are found to play a significant role in explaining many of the observed phenomena in experiment [53–55]. In each collision event, the position of nucleons in a nucleus fluctuates, leading to event-by-event initial state fluctuations. To capture these fluctuations, randomness in models needs to be considered. For example, optical Glauber model and KLN model can be extended to their Monte Carlo versions, by introducing the fluctuations of nucleon positions with respect to the distribution profile, Eq. (1.6). On an event-by-event basis, fluctuating initial geometry breaks the rotational and reflection symmetry of the averaged distributions. A detailed discussion on this will be given in Chapter 2.

1.3.2 Hydrodynamic description of the hot medium

For recent reviews of the viscous hydrodynamics and its applications to heavy-ion collisions, see [56, 57].

Hydrodynamic equations of motion

The essential concept of hydrodynamics consists of the conservation of energy-momentum and conserved charges, which leads to the following equations of

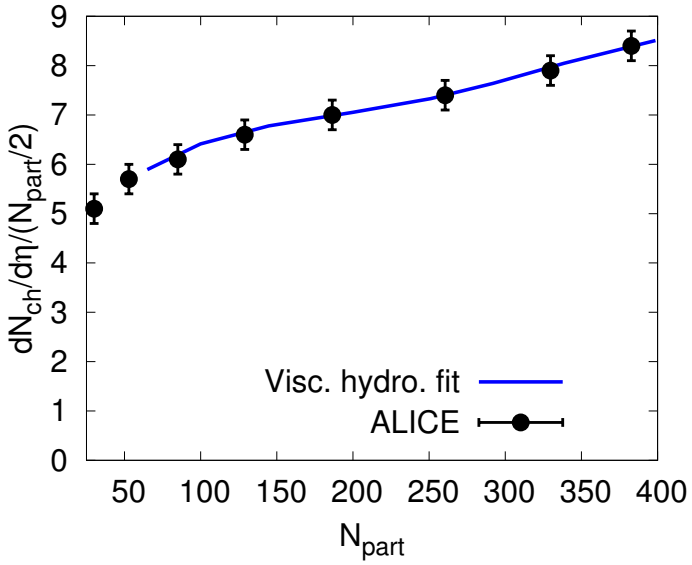

Figure 1.7: A fit of charged particle multiplicity from viscous hydrodynamic simulations with the initial parameter C_s taken in Table 1.1, with respect the ALICE measurement [5].

motion (EOM),

$$d_\mu T^{\mu\nu} = 0\,, \tag{1.12a}$$
$$d_\mu J^{\mu a} = 0\,, \qquad a = 1, 2, \ldots, N \tag{1.12b}$$

where the index a runs from 1 to N, labelling the types of conserved charge. Here d_μ denotes covariant derivative, which is introduced to treat the Bjorken coordinate system, τ and η_s. Given the forms of stress tensor $T^{\mu\nu}$ and conserved current $J^{\mu a}$ of type a, Eq. (1.12) give rise to $4 + N$ coupled equations of motion.

For a full characterization of the fluid system, with respect to the physics of conservation laws, a set of hydrodynamic variables containing flow 4-velocity u^μ, charge density of type a n^a (or its canonical conjugate chemical potential μ_a), energy density ε (or its canonical conjugate temperature T) and pressure $\mathcal{P}$ must be determined according to the space-time evolution. Following the basic properties in relativity, the components of the flow velocity can be parameterized as

$$u^\mu = \gamma(1, \boldsymbol{v}_\perp, v_\parallel), \qquad \gamma = \frac{1}{\sqrt{1 - \boldsymbol{v}^2}}\,. \tag{1.13}$$

The normalization of flow velocity

$$u^\mu u_\mu = -1, \tag{1.14}$$

reduces the number of independent hydrodynamic variables from $6 + N$ to $5 + N$. In the relativistic version of hydrodynamics, just as its classical counterpart, there is a freedom in the definition of the flow 4-velocity u^μ. For example, in the Eckart frame u^μ is associated to the flow of conserved charge current. On the other hand, when u^μ denotes the energy flow, we obtained the hydrodynamics in the Landau-Lifshitz frame. In the previous case, it is expected that

$$u^\mu J^a_\mu = n^a \,, \tag{1.15}$$

while in the latter case we have

$$u_\mu T^{\mu\nu} u_\nu = \varepsilon \,. \tag{1.16}$$

The choice of frames to define the flow 4-velocity in hydrodynamics leads to no physical difference in the applications, but it simplifies the analysis for particular problems. Throughout this work, we stick to the Landau-Lifshitz definition in which the general forms of the stress tensor and the conserved current are constructed in terms of these hydrodynamic variables as [58],

$$T^{\mu\nu} = (\varepsilon + \mathcal{P}) u^\mu u^\nu + \mathcal{P} g^{\mu\nu} + \Pi^{\mu\nu} \,, \tag{1.17a}$$

$$J^{\mu a} = n^a u^\mu + I^{\mu a} \,. \tag{1.17b}$$

$\Pi^{\mu\nu}$ and $I^{\mu a}$ in Eq. (1.17) stand for dissipative corrections, satisfying

$$u^\mu \Pi_{\mu\nu} = 0 \,, \quad \text{and} \quad u^\mu I^a_\mu = 0 \,. \tag{1.18}$$

Equation of State

The apparent excessive one degree of freedom of the hydrodynamic system is fixed by the equation of state (EoS), relating the thermodynamic variables, *e. g.* ε and $\mathcal{P}$. Corresponding to the bulk system created in heavy-ion collisions, the equation of state which mirrors the dynamical properties of the QCD medium, needs to be taken from the underlying theory. For instance, considering the system in a simplified picture, that the expanding medium is a pure conformal quark-gluon gas without phase transition, we have the typical conformal EoS, $\varepsilon = 3\mathcal{P}$. And it is not difficult to generalize this result for all the rest of thermodynamic variables.

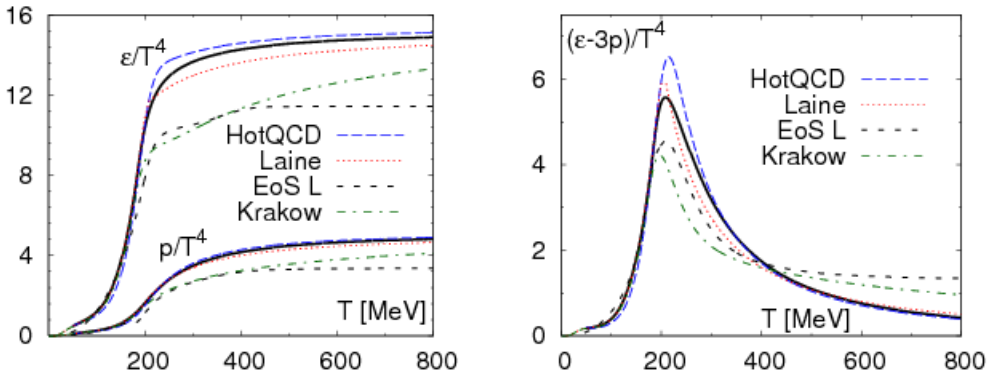

Figure 1.8: A summary of lattice EoS. Figures taken from [6].

More realistically, since color confinement phase transition as well as the hadron gas need to be characterized at low temperature, *i. e.* the later time of medium evolution, EoS from lattice QCD simulations are considered [6]. In Fig. 1.8, a number of parameterizations are shown from different lattice QCD results. In our work, the 'Laine' curve [59] which was first used by Luzum and Romatschke [45] is applied and found very limited difference comparing to the latest *s95p*-v1 parametrization [6], which is the solid black line in Fig. 1.8. Parameterizations of lattice EoS cover a sufficiently wide range for the application of hydrodynamics, with $T_c \sim 200$MeV commonly taken into account despite the detailed difference in these lattice simulations, as seen in Fig. 1.8.

There are two prominent properties of the lattice EoS, as well as the QCD medium that hydrodynamics is to be applied to in heavy-ion collisions. First is the negligible conserved charges. In the bulk medium in heavy-ion collision of QGP phase, the baryon number which is the potential conserved charge is expected to be small. On the other hand, fluidity of the bulk medium, even in hadron gas phase, demands a strong interaction between constituents, which prevents the whole system from chemical equilibrium. It is only at very low temperature, *i. e.* $T \lesssim 120$ MeV, fluid system kinetically decouples and conservations of, *e. g.* strangeness, become significant. This property of the medium introduces a strong constraint and also simplification to the hydrodynamic equations of motion, rendering the equation of motion in Eq. (1.12b) trivial. Thereby, in our work we neglect the constraint from the conservation of conserved charges in hydrodynamics, which is also one general consideration taken in present hydrodynamic simulations.

Second, the conformality of a medium is one of the fundamental symmetries, which constrains the dynamics dramatically. Especially, conformality

strongly bounds the value of bulk viscosity ζ. Seen in Fig. 1.8, the trace anomaly $\varepsilon - 3\mathcal{P}$ which measures the magnitude of deviations from conformality is scaled by T^4, rises only around T_c. This expectation is to some extent consistent with the analyses on bulk viscosity in predicting harmonic flow in heavy-ion collisions [60]. Nonetheless, as the study on bulk viscous correction is beyond the scope of this work, we will focus on the shear tensor by taking $\zeta = 0$, thus $\Pi^{\mu\nu} = \pi^{\mu\nu}$.

Solving hydrodynamic equations of motion

It is very convenient to decompose 4-vector in hydrodynamics with respect to the flow 4-velocity in Eq. (1.13), which in the local rest frame (LRF) is time-like, $(1, \mathbf{0})$. For instance, by defining the following projection operator,

$$\Delta^{\mu\nu} = u^\mu u^\nu + \eta^{\mu\nu} \,, \tag{1.19}$$

any vector V^μ can be decomposed as

$$V_\perp^\mu = \Delta^{\mu\nu} V_\nu \,, \tag{1.20}$$

and

$$V_\parallel^\mu = V^\mu - V_\perp^\mu \,. \tag{1.21}$$

Since $\Delta^{\mu\nu}$ reduces to $(0, 1, 1, 1)$ in the LRF, it is not difficult to see that $V_\parallel^\mu$ is time-like, $V_\perp^\mu$ is space-like and $V_\perp \cdot u = 0$. In particular, for the covariant derivatives we define

$$\nabla^\mu = \Delta^{\mu\nu} d_\nu \qquad \xrightarrow{\text{LRF}} \qquad d^i \tag{1.22a}$$

$$D = u^\mu d_\mu \qquad \xrightarrow{\text{LRF}} \qquad d^0 \tag{1.22b}$$

With these decompositions, and $\Pi^{\mu\nu} = 0$, the ideal hydrodynamic equations of motion can be re-expressed as

$$D\varepsilon = -(\varepsilon + \mathcal{P}) \nabla \cdot u \,, \tag{1.23a}$$

$$Du^\nu = -\frac{\nabla^\nu \mathcal{P}}{\varepsilon + \mathcal{P}} = -\nabla^\nu \ln T \,, \tag{1.23b}$$

which are the relativistic version of the constituent relation and Euler equation in the classical hydrodynamics. In obtaining the second equality in Eq. (1.23b),

we have used the thermodynamic relation,

$$\sum_{a=1}^{N} \frac{n^a}{\varepsilon + \mathcal{P}} d\left(\frac{\mu_a}{T}\right) = \frac{d\mathcal{P}}{T(\varepsilon + \mathcal{P})} + d\left(\frac{1}{T}\right) = 0\,. \tag{1.24}$$

The form of Eq. (1.23) has particular implications, that the time derivative of a quantity can always be expressed in terms of spatial gradients. Writing all time derivatives into spatial gradients is sometimes referred as the solubility condition in kinetic theory [61], which has significant application in the theory of hydrodynamics, and will be discussed in details in Chapter 5.

Generally there is no analytical solution to the coupled hydrodynamic equations of motion, Eq. (1.12) and EoS, especially when dissipative effects are involved. The more approachable way is the computation on a computer. In doing so, some further simplifications can be practically introduced, based on the approximations and symmetries. For example, with Bjorken boost invariance, with respect to the space-time configuration in heavy-ion collisions, the η_s dependence is trivial which reduces the hydrodynamics to 2+1 dimensions. This simplification, leads to the basic form of hydrodynamic equations of motion in the (τ, x, y, η_s) coordinate system,

$$\begin{aligned}
\partial_\tau T^{\tau\tau} + \partial_x T^{x\tau} + \partial_y T^{y\tau} &= -\frac{1}{\tau} T^{\tau\tau} - \tau T^{\eta_s\eta_s}\,, \\
\partial_\tau T^{\tau x} + \partial_x T^{xx} + \partial_y T^{yx} &= -\frac{1}{\tau} T^{x\tau}\,, \\
\partial_\tau T^{\tau y} + \partial_x T^{xy} + \partial_y T^{yy} &= -\frac{1}{\tau} T^{\tau y}\,.
\end{aligned} \tag{1.25}$$

In the extreme case of 1+1 dimension, with the translational invariance along η_s we have the ideal hydrodynamic equation of motion

$$\frac{\partial \varepsilon}{\partial \tau} = -\frac{\varepsilon + \mathcal{P}}{\tau}\,, \tag{1.26}$$

which has an analytical solution for a conformal fluid, $\varepsilon \sim \tau^{-4/3}$.

The construction of shear tensor $\pi^{\mu\nu}$, which contains all of the dissipative effects in hydrodynamics in our work, has no particular constraints except the second thermodynamic law, *i. e.* $\Delta s \geq 0$ [58]. To the first order in the gradient expansion, we have the well-known Navier-Stokes hydrodynamics, in which the shear tensor is uniquely formed as

$$\pi^{\mu\nu} = -\eta\sigma^{\mu\nu}\,, \tag{1.27}$$

where

$$\sigma^{\mu\nu} = 2\langle \nabla^{\mu} u^{\nu} \rangle \,. \tag{1.28}$$

Throughout this work, the tensor indices inside the angle brackets $\langle \ldots \rangle$, as in Eq. (1.28), stand for being symmetric, traceless and orthogonal to the flow 4-velocity. More details of the definition and decomposition of tensor indices can be found in Appendix A.

However, this first order viscous hydrodynamics in Eq. (1.27) has defects for realistic hydrodynamic simulations, for two reasons. First, only including first order in gradient in hydrodynamics breaks causality, which is reflected from the existence of the superluminal mode [56]. Second, the algorithm of solving first order viscous hydrodynamics on a computer in not stable. Although either of these two issues devastates the application of hydrodynamics, it is necessary to have rigorous treatment in physical study. The remedy to both of these problems is to go beyond first viscous corrections in hydrodynamics, to include as well second order terms. Following the rule of second thermodynamic law, a great number of second order viscous corrections to hydrodynamics can be deduced. In particular, adapting specifically some of these second order terms results in a variety of types of second order viscous hydrodynamics, such as the widely used Israel-Stewart hydrodynamics [62]. Taking into account of conformal symmetry, Baier, Romatschke, Son, Starinets, and Stephanov developed the BRSSS hydrodynamics [63], in which only those second order terms obeying conformal symmetry are selected in the formulation,

$$\begin{aligned} \pi^{\mu\nu} = -\eta\sigma^{\mu\nu} + \eta\tau_{\pi} \left[\langle D\sigma^{\mu\nu} \rangle + \frac{1}{d-1} \sigma^{\mu\nu} \nabla \cdot u \right] \\ + \lambda_1 \langle \sigma^{\mu}{}_{\lambda} \sigma^{\nu\lambda} \rangle + \lambda_2 \langle \sigma^{\mu}{}_{\lambda} \Omega^{\nu\lambda} \rangle + \lambda_3 \langle \Omega^{\mu}{}_{\lambda} \Omega^{\nu\lambda} \rangle + O(\nabla^3) \,. \end{aligned} \tag{1.29}$$

In Eq. (1.29), the tensor structure called vorticity $\Omega^{\mu\nu}$ is defined as anti-symmetric, and orthogonal to flow 4-velocity,

$$\Omega^{\mu\nu} = \frac{1}{2} \Delta^{\mu\alpha} \Delta^{\nu\beta} \left(\nabla_{\alpha} u_{\beta} - \nabla_{\beta} u_{\alpha} \right) \,. \tag{1.30}$$

In analogus to the shear viscosity η, second order transport coefficients τ_{π}, λ_1, λ_2 and λ_3 need to be determined from the underlying theory, as the input parameters for hydrodynamic simulations. Considering the relation

$$\pi^{\mu\nu} = -\eta\sigma^{\mu\nu} + O(\nabla^2) \,, \tag{1.31}$$

it is legal to iteratively substitute the σ's with π on the right hand side of

Eq. (1.29), with the cost of errors of third order in the gradient expansion. We obtain the following equations of motion with $\pi^{\mu\nu}$ as a dynamical variable,

$$\pi^{\mu\nu} = -\eta\sigma^{\mu\nu} - \tau_\pi \left[\langle D\pi^{\mu\nu} \rangle + \frac{4}{3}\pi^{\mu\nu}\nabla \cdot u \right] + \frac{\lambda_1}{\eta^2}\langle \pi_\lambda^{\ \mu}\pi^{\lambda\nu} \rangle - \frac{\lambda_2}{\eta}\langle \pi_\lambda^{\ \mu}\Omega^{\lambda\nu} \rangle + \lambda_3 \langle \Omega^\mu_{\ \lambda}\Omega^{\nu\lambda} \rangle + O(\nabla^3)\,. \tag{1.32}$$

Solving BRSSS equations of motion Eq. (1.32), in combination with Eq. (1.25), give rise to a causual description of the hydrodynamic evolution of bulk medium in heavy-ion collisions. This 2+1 dimensional, viscous hydrodynamics is the baseline of our work.

1.3.3 Freeze-out and resonance decay

The fluid system created in heavy-ion collisions will eventually decouple and all sorts of observables in experiment are supposed to be the consequence after decoupling. The potential mechanism of sustaining the collectivity of medium is microscopic dynamical interactions, such as elastic and inelastic collisions of partons in QGP phase and hadrons in HG phase. As the temperature of the system decreases along with system expansion, which weakens the scattering processes accordingly, a series of (phase) transitions take place. As is roughly stated in the following line,

$$\underbrace{T_0 \longrightarrow T_c \longrightarrow}_{\text{elastic+inelastic+radiative}} \quad T_{\text{chem}} \quad \underbrace{\longrightarrow}_{\text{elastic+radiative}} \quad T_{\text{fo}} \quad \underbrace{\longrightarrow}_{\text{radiative}}$$

there are two major decoupling processes need to be considered: chemical freeze-out at T_{chem}[64] and kinetic freeze-out at T_{fo}. Chemical freeze-out means that the species composition of the hadronic matter is fixed in equilibrium, though this equilibrium is approximated by neglecting inelastic collisions between hadrons. After kinetic freeze-out the system size becomes much larger than the mean free path λ_{mfp}, thereby kinetic behavior of particles is stabilized.Kinetic freeze-out is generally regarded as the end of the hydrodynamic description, and incorporated by Cooper-Frye formula [65],

$$E\frac{d^3N_i}{dp^3} = \frac{g_i}{(2\pi)^3}\int_\Sigma p \cdot d\sigma f_i(x, \boldsymbol{p}, M_i, \mu_i), \tag{1.33}$$

in which i is particularly used to indicate the particle species, *e. g.* g_i stands for the degeneracy factor of particle i. Eq. (1.33) is a Lorentz invariant form, with the integral element $pd\sigma$ defined on a specified hyper-surface Σ. Σ is

determined by the kinetic freeze-out creterian. Generally, this creterian can be selected as a specified freeze-out entropy density $s_{\rm fo}$ or a freeze-out temperature $T_{\rm fo}$. In our simulations, we take a constant freeze-out temperature, so that the following equation

$$T(t, \boldsymbol{x}) = T_{\rm fo}\,, \tag{1.34}$$

defines a hyper-surface in the 3+1 dimensional space-time.

The basic function of Cooper-Frye formula Eq. (1.33) is to transform the space-time dependence of the hydrodynamic fields into the momentum dependence of particle spectrum, as long as the phase space distribution function $f_i(x, \boldsymbol{p}, M_i, \mu_i)$ is entirely known. As the major subject to be discussed in details in Chapter 5, the form of $f_i(x, \boldsymbol{p}, M_i, \mu_i)$ needs to be consistently considered with respect to the corresponding hydrodynamics, in parallel with kinetic theory. For ideal hydrodynamics, local equilibrium requires the equilibrated distribution function $n_p^i(x, \boldsymbol{p})$, which can be Fermi-Dirac, Bose-Einstein, or classical Boltzmann distributions, with respect to the specified case under consideration. Similarly, dissipative effects in hydrodynamics leads to corrections to the distribution function δf. The form [66]

$$\delta f_\pi = \frac{n_p(1 \pm n_p)}{2(e + \mathcal{P})T^2} p^\mu p^\nu \pi_{\mu\nu}, \tag{1.35}$$

which was originally proposed based on a kinetic theory approach, is presently used a lot for viscous hydrodynamic simulations.

Before the 'ultimate' stabilized particle spectrum in experiment is reached, unstable particles like resonances will decay and change the particles production. Therefore, in a strict manner, Cooper-Frye formula should be applied by including all possible particle species listed in the PDG table [26], followed by resonance decay processes. However in practice it is sufficient to cut the particle list to some massive particle (*e. g.*, let $M_R \leq 2\text{GeV}$) to simplify the calculation. Taking the scheme based on the analyses in [67, 68], predictions comparable to experiment, such as charged particle multiplicity, can be achieved, as shown in Fig. 1.7.

1.4 Outline of this work

Based on our work published in [69–72], this thesis is organized as follows. For initial state fluctuations in heavy-ion collisions, in Chapter 2 we discuss the cumulant expansion formalism. In our work, cumulants are used to classify and characterize the azimuthal anisotropies induced by these fluctuations, so that

eccentricities and the participant plane angles are defined systematically. With Monte-Carlo simulations of PHOBOS Glauber model, effects of fluctuations in the initial state are reflected in the centrality dependent eccentricities, as well as participant plane correlations.

With the initial state fluctuations characterized with cumulants, in Chapter 3 the medium response to initial anisotropies is investigated in terms of the linear flow response and the nonlinear flow response. Flow response coefficients are analyzed as a function of the transverse momentum, centrality and especially shear viscosity to entropy ratio. p_T and centrality dependence of the flow response coefficients determines the behavior of the observed harmonic flow signatures, such as $v_n\{2\}$. η/s dependence reveals the medium transport property. When the flow response formalism is applied to the realistic heavy-ion collisions, the predictions can be analytically understandable.

In Chapter 4, we analyze event plane correlations based on the flow response formalism, with respect to the recent measurements by ATLAS collaboration [7]. Although the rigorous formulation of these plane correlations relies on the resolution of the measurement, it is possible in our work to calculate either in the high resolution limit or in the low resolution limit. We also examine the contributions to the obtained event plane correlations from linear flow response and nonlinear flow response separately, which we refer as the 'linear limit' and 'nonlinear limit' respectively.

The inconsistency of the viscous hydrodynamics framework is studied in Chapter 5. Viscous hydrodynamic simulations provide an indispensable tool for the analysis of the medium property in heavy-ion collisions. However, as we will detail in Chapter 5, regarding the widely used second order viscous hydrodynamics, the viscous corrections to the phase space distribution is just consistent at first order. By kinetic theory, second order correction $\delta f_{(2)}$ is obtained in this work, with respect to the BRSSS hydrodynamics. The effect of $\delta f_{(2)}$ is investigated for the linear flow response coefficients.

As mentioned earlier, notations and conventions we take throughout this work are summarized in Appendix A.

Chapter 2

Fluctuations in the initial state

In the past several years, the significance of initial state fluctuations was gradually realized [53–55]. In particular, Alver and Roland [54] proposed initial state fluctuations as the generic origin of the "ridge" and "shoulder" structures in the two-particle correlation functions in nucleus-nucleus collisions. In their analysis, odd order harmonics of the collective flow, such as triangular flow v_3 [73], arise due to the medium response to a fluctuating initial state. In the Fourier decomposition of the observed two-particle correlation spectrum, a large fraction of the contribution was found from v_3, which naturally explains the general features of long-range two-particle correlations.

The realization of initial state fluctuations generalizes the investigation of harmonic flow. First, accounting for the medium response to a initial geometry with no particular symmetry, harmonics of all possible orders are expected. In addition to the triangular flow, in recent years, extensive endeavors on harmonic flows have been devoted experimentally and theoretically. From RHIC Au-Au [74, 75] and LHC Pb-Pb [76–78] collisions, dipole flow v_1, quadrapole flow v_4, and pentagonal flow v_5, *etc.* were measured. Correspondingly, theoretical analyses based on hydrodynamics [69, 73, 79, 80] and transport theory [73, 81] calculations were applied. Second, the fluctuating initial state has a complex geometry, which leads to non-trivial event plane correlations of the final state [7, 82–84]. The combined investigation of harmonic flows and event plane correlations provide new constraints on properties of the medium produced in heavy-ion collisions.

The fluctuations in the initial stage of heavy-ion collisions, alters the theoretical modeling of the initial state. A bumpy profile, instead of a smooth and symmetric initial density distribution, controls the initial geometry on an event-by-event basis. As discussed in Section 1.3, to initialize the dynamical description of the medium expansion with respect to a fluctuating initial state, we should generalize the effective models of initial state with randomness. The

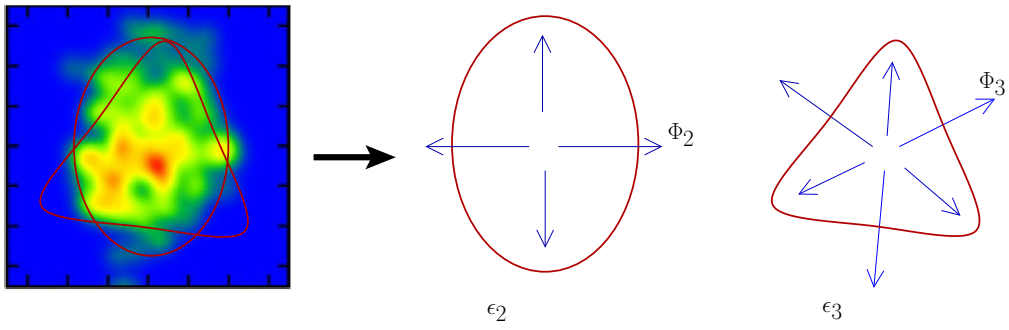

Figure 2.1: The fluctuating initial state of one typical collision event, for the event-by-event hydrodynamic simulations. The blue arrows indicate the direction and magnitude of gradients.

Monte Carlo version of Glauber model, for instance, is constructed by sampling the nucleon distribution inside a nucleus. With respect to a fluctuating initial condition, there are two types of hydrodynamic simulations can be applied for realistic calculations – event-by-event hydrodynamics[79, 85] and single-shot hydrodynamics.

In the event-by-event hydrodynamics, the initial conditions are sampled on an event-by-event basis. For each particular event a bumpy distribution like the one shown in Fig. 2.1 is generated and is evolved. Solving hydrodynamic equations of motion for this particular initial profile, leads to a particle spectrum containing all harmonics. In analogy to the data analysis carried out in experiment, final state observables from the event-by-event hydrodynamics are subsequently extracted from event averages of the accumulated particle spectra. To a large extent, event-by-event hydrodynamic calculations resemble realistic heavy-ion events. With parameters of the hydrodynamic simulations appropriately selected (*i. e.* with $\eta/s \lesssim 2/4\pi$), a number of predictions have been made. For example, the harmonic flow v_n [86] and event-plane correlations [87] have been calculated in the event-by-event hydrodynamic framework and are comparable to the experimental observations

In linearized single-shot hydrodynamics (or the linear response), the fluctuations in the initial state are treated as perturbations of the average geometry, and the response to a given perturbation is studied. Thus, In the single-shot hydrodynamic simulations, the harmonic flow of final state is assumed to be proportional to its corresponding initial state anisotropy. Therefore, the treatment of the initial state fluctuations is simplified. The initial stage of heavy-ion collisions can be studied by these initial state Monte Carlo simulations, which is independent of the hydrodynamic description of the medium

expansion. Single-shot hydrodynamics separates initial stage and the medium evolution afterwards, and thus has the advantage of theoretically analyzing initial state fluctuations, the flow generation during the medium expansion, and their mutual relations. As will be stated in details in Chapter 3 and Chapter 4, these direct investigations on initial state, and flow generations are crucial for theoretical analyses, especially the extraction of η/s.

The first step in developing the response formalism is to characterize the initial perturbations of the average geometry. Subsequently the response the these perturbations can be determined. The n-th order azimuthal anisotropy, ϵ_n, is defined as

$$\epsilon_n e^{in\Phi_n} = -\frac{\{r^m e^{in\phi_r}\}}{\{r^m\}}\,, \tag{2.1}$$

where

$$\{\ldots\} = \frac{\int d\boldsymbol{s}\ldots\rho(\boldsymbol{s})}{\int d\boldsymbol{s}\rho(\boldsymbol{s})} \tag{2.2}$$

indicates the average over the transverse plane with the fluctuation. The minus sign in Eq. (2.1) is conventionally taken so that the associated participant angle Φ_n points to the shorter axis, along the direction with the largest spatial gradient and therefore the direction of the associated event plane angle Ψ_n of n-th order harmonic flow in a linear response approximation. ϵ_n basically describes a n-th regular polygon, which can be abstracted from a bumpy distribution and originates a n-th order anisotropic flow in analogous to v_2, as illustrated in Fig. 2.1. Note that Eq. (2.1) is a empirical formula, in which the power of r in both the denominator and numerator is left arbitrary. A widely accepted definition of ϵ_n is to take $m = n$ in Eq. (2.1), which we refer as the moment definition.

In this chapter, on the other hand, we introduce the cumulant expansion formalism for the classification and definition of these anisotropies. The cumulant expansion for a fluctuating initial state and its implementation to the hydrodynamic calculations is formulated in Section 2.1 and Section 2.2. The systematic characterization of the initial anisotropies with cumulants, leads to distinct results. Especially, in Section 2.3 the difference between the moment and the cumulant definitions are discussed based on the averaged eccentricities and participant plane correlations from the Monte Carlo simulations.

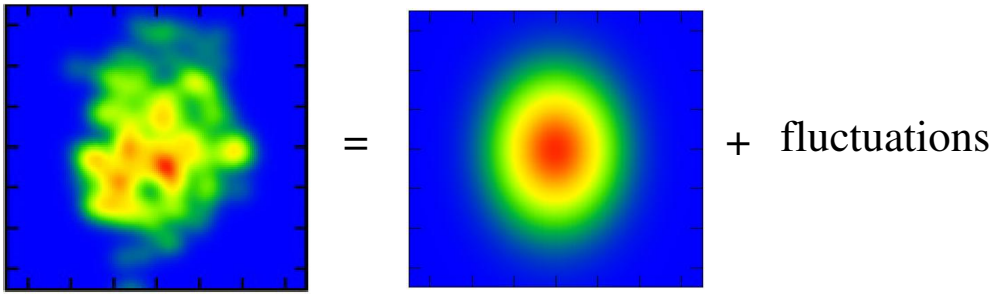

Figure 2.2: Decomposition of the fluctuating initial state into Gaussian background plus perturbations.

2.1 Cumulant expansion

In this section, we present the basic concepts of the cumulant expansion formalism. The idea of applying cumulant expansion to a fluctuating initial state stems from an approximated decomposition. As illustrated in Fig. 2.2, fluctuations in a bumpy initial density profile of heavy-ion collisions can be separately recognized as perturbations on top of a smooth Gaussian background. This decomposition into background and fluctuations corresponds to the order-by-order cumulant expansion.

Formulation of the cumulant expansion formalism

Let us start with a normalized initial entropy density $\rho(\boldsymbol{x}_\perp)$ in the 2-dimensional transverse plane, *i. e.*, $\rho(\boldsymbol{x}_\perp) = \tau_o s(\tau_o, \boldsymbol{x}_\perp)/\int \tau_o d^2\boldsymbol{x}_\perp s(\tau_o, \boldsymbol{x}_\perp)$ [1]. The Fourier transformation of the spatial distribution is,

$$\rho(\boldsymbol{x}_\perp) \quad = \int d^2\boldsymbol{k}_\perp e^{i\boldsymbol{k}_\perp\cdot\boldsymbol{x}_\perp}\hat{\rho}(\boldsymbol{k}_\perp)\,. \tag{2.3}$$

From the Fourier transformation, we define $\hat{W}(\boldsymbol{k}_\perp)$ as the generating functional of cumulants,

$$\hat{\rho}(\boldsymbol{k}_\perp) \quad = e^{\hat{W}(\boldsymbol{k}_\perp)} = \int d^2\boldsymbol{x}_\perp e^{-i\boldsymbol{k}_\perp\cdot\boldsymbol{x}_\perp}\rho(\boldsymbol{x}_\perp)\,. \tag{2.4}$$

The spatial fluctuations in $\rho(\boldsymbol{x}_\perp)$ are related to the $\boldsymbol{k}_\perp$ dependence of $\hat{W}(\boldsymbol{k}_\perp)$. We will expand $\hat{W}(\boldsymbol{k}_\perp)$ at small $k_\perp$. This is because we wish to determine the long distance perturbations to the Gaussian background. For the sake of of

[1] We have used the entropy density distribution to define $\rho(\boldsymbol{x}_\perp)$. Alternative formulation with energy density is straightforward.

convenience, we introduce the following complex notations

$$\bar{k} = ke^{i\phi_k}, \qquad \bar{r} = re^{i\phi_r}\,, \tag{2.5}$$

so that,

$$\boldsymbol{k}_\perp \cdot \boldsymbol{x}_\perp = \mathbf{Re}(\bar{k}\bar{r}^*) = \frac{1}{2}(\bar{k}\bar{r}^* + \bar{k}^*\bar{r}) = kr\cos(\phi_k - \phi_r)\,. \tag{2.6}$$

In the long wavelength limit, we expand the exponential factor with respect to $|\boldsymbol{k}_\perp|$,

$$\begin{aligned} e^{-i\boldsymbol{k}_\perp\cdot\boldsymbol{x}_\perp} &= 1 + \sum_{n=1}^{\infty} \frac{(-i)^n}{n!2^n}(\bar{k}\bar{r}^* + \bar{k}^*\bar{r})^n \\ &= \sum_{n=0}^{\infty}\sum_{l=0}^{n} \frac{(-i)^n C_n^l}{n!2^n}(\bar{k}\bar{r}^*)^l(\bar{k}^*\bar{r})^{n-l}\,, \end{aligned} \tag{2.7}$$

from which and the original Fourier transformations we obtain the expansion of $\hat{\rho}(\boldsymbol{k}_\perp)$

$$\hat{\rho}(\boldsymbol{k}_\perp) = \sum_{n=0}^{\infty}\sum_{l=0}^{n} \frac{(-i)^n C_n^l}{n!2^n}\bar{k}^l(\bar{k}^*)^{n-l}\{(\bar{r}^*)^l r^{n-l}\}\,. \tag{2.8}$$

Note that $\{\ldots\}$ appears in the above equation as a result of the weighted integral by $\rho(\boldsymbol{x}_\perp)$ in the transverse plane. The geometric information of the original spatial distribution is contained in these averages. Correspondingly the cumulant expansion is formulated in the expansion of $\hat{W}(\boldsymbol{k}_\perp)$,

$$\begin{aligned} \hat{W}(\boldsymbol{k}_\perp) &= \sum_{n,m}(-i)^n\hat{W}_{n,m}(\boldsymbol{k}_\perp) = \ln\hat{\rho}(\boldsymbol{k}_\perp) \\ &= \sum_{j=1}^{\infty}\frac{(-1)^{j-1}}{j}\left(\sum_{n=0}^{\infty}\sum_{l=0}^{n}\frac{(-i)^n C_n^l}{n!2^n}\bar{k}^l(\bar{k}^*)^{n-l}\{(\bar{r}^*)^l r^{n-l}\}\right)^j\,. \end{aligned} \tag{2.9}$$

In Eq. (2.9) the pair of indices (n, m) in $\hat{W}_{n,m}(\boldsymbol{k}_\perp)$ denote the order of long wavelength expansion k^n (the order of perturbavie corrections) and the order of azimuthal angle $m\phi_k$ respectively. Correspondingly, in the configuration space they denote the deformations along radial (r^n) and azimuthal ($m\phi_r$) directions. Considering the combination in Eq. (2.9)

$$\bar{k}^l(\bar{k}^*)^{n-l} = k^n e^{-i(n-2l)\phi_k} \quad \longleftrightarrow \quad (\bar{r}^*)^l r^{n-l} = r^n e^{i(n-2l)\phi_r}\,, \tag{2.10}$$

we recognize the relation $m = |n - 2l|$, which implies that for a m-th order azimuthal deformation, there exist in principle a series of higher order cumulant terms weighted by r^n with $n = m, m+2,\ etc.$. By imposing $\langle \bar{r} \rangle = \langle \bar{r}^* \rangle = 0$, so that the system center is redefined to be the center of mass, we rewrite the terms in the cumulant expansion,

$$\hat{W}_{n,m}(\boldsymbol{k}_\perp) = \frac{1}{n!2^n} C_n^{(n-m)/2} \left[k^n e^{-im\phi_k} W_{n,m} + c.c. \right] . \tag{2.11}$$

In Eq. (2.11) the factors with spatial averages are absorbed in the so-called cumulant $W_{n,m}$. Our goal of cumulant expansion is to systematize the detailed structure of $W_{n,m}$, from which the anisotropy of a fluctuating initial state can be defined. A simple rule of writing the forms of Eq. (2.11) and the cumulants $W_{n,m}$ is as follows.

1. There is an overall constant coefficient, $\frac{1}{n!2^n} C_n^{(n-m)/2}$.

2. $W_{n,m}$ is formed in terms of the averages of powers of $\bar{r}$ and $\bar{r}^*$:

$$\{ \underbrace{\bar{r} \ldots \bar{r}}_{(n+m)/2} \underbrace{\bar{r}^* \ldots \bar{r}^*}_{|n-m|/2} \} + \sum_\alpha (-1)^{N-1} C_\alpha \underbrace{\{\bar{r} \ldots\} \ldots \{\ldots \bar{r}^*\}}_{N \text{ sets of brackets}} + c.c., \tag{2.12}$$

   - In each term the total number of $\bar{r}$ is $(n+m)/2$, and the number of $\bar{r}^*$ is $|n-m|/2$.
   - For each term with N sets of average brackets, there is an extra factor $(-1)^{N-1}$.
   - The coefficient C_α is determined by the combinatorial counting of the average brackets in the term.

As a simple summary, we list some of these lowest order cumulants which we will encounter in this work frequently,

$$W_{2,2} = \{\bar{r}^2\} + c.c. , \tag{2.13a}$$
$$W_{3,1} = \{\bar{r}^2 \bar{r}^*\} + c.c. , \tag{2.13b}$$
$$W_{3,3} = \{\bar{r}^3\} + c.c. , \tag{2.13c}$$
$$W_{4,4} = \left[\{\bar{r}^4\} \underline{-3\{\bar{r}^2\}^2} \right] + c.c. , \tag{2.13d}$$
$$W_{5,5} = \left[\{\bar{r}^5\} \underline{-C_5^3 \{\bar{r}^3\}\{\bar{r}^2\}} \right] + c.c. , \tag{2.13e}$$
$$W_{6,6} = \left[\{\bar{r}^6\} \underline{-C_6^2 \{\bar{r}^4\}\{\bar{r}^2\} - \frac{C_6^3}{2} \{\bar{r}^3\}^2 + \frac{C_6^2 C_4^2}{3!} \{\bar{r}^2\}^3} \right] + c.c. . \tag{2.13f}$$

Note that these underlined nonlinear terms in Eq. (2.13) appear when $n \geq 4$.

Classification of anisotropies and the dipole asymmetry

From the complex form of cumulant, we define eccentricities and the associated participant plane angles for a fluctuating initial state,

$$\mathcal{C}_{n,m} e^{im\Phi^c_{n,m}} = -\frac{W_{n,m}}{\{r^n\}}\,, \tag{2.14}$$

or equivalently

$$\mathcal{C}_{c,m} = \frac{|W_{n,m}|}{\{r^n\}}\,, \tag{2.15a}$$

$$\Phi^c_{n,m} = \frac{\arg(W_{n,m})}{m} + \frac{\pi}{m}\,. \tag{2.15b}$$

In additional to the index m which characterizes the azimuthal deformation, in the cumulant definition with $W_{n,m}$, the index n is also included for the description of fluctuations along the radial direction. In the cumulant expansion, higher order perturbation terms (which characterize short distance fluctuations) are assumed to be damped. This expansion is supported by the observed suppression of higher order harmonic modes. In particular, as we will show in the discussion on the viscous effect in hydrodynamics, the medium response to higher order cumulant is significantly damped. As a consequence, it is natural to stick to the lowest order terms in the cumulant expansion, and consider only the $n = m$ case, for the m-th order azimuthal asymmetry. The cumulant definition differs from the moment definition, except when $n = m = 2$ and 3. Therefore, in our work the notations $\mathcal{C}_n$ and Φ^c_n are taken to specify the cumulant defined eccentricities and participant angles in Eq. (2.14) and Eq. (2.15). However, in general ϵ_n and Φ_n are still used for discussions, even in the $n \geq 4$ case when no confusion can arise.

In Eq. (2.13), $W_{3,1}$ is obtained from the third order in the cumulant expansion, which defines a novel description of the azimuthal anisotropy, the dipole asymmetry,

$$\mathcal{C}_{3,1} e^{i\Phi_{3,1}} = -\frac{W_{3,1}}{\{r^3\}}\,. \tag{2.16}$$

Dipole asymmetry describes a higher order deformation breaking the reflection symmetry of the average background, which appears in a distribution with fluctuations even though the system center is redefined. The distortion

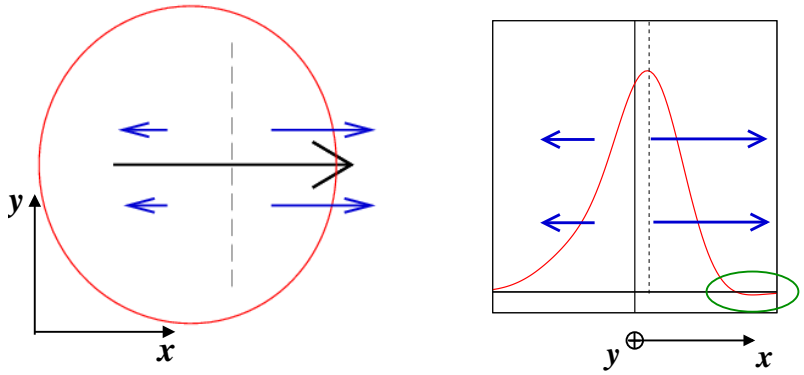

Figure 2.3: A schematic picture of the dipole asymmetry.
The schematic view from z-direction and y-direction of a distribution with only dipole asymmetry. The blue arrows indicate the direction and magnitude of gradients as usual. Note the circled part at large radius where the distribution becomes negative.

of the distribution, leaving the geometric center unaltered, results in a gradient asymmetry along the direction $\Phi_{3,1}$. Fig. 2.3 shows an initial condition with a net dipole asymmetry. In this case the maximum of the entropy distribution sits to the right of the center of entropy (see Fig. 2.3). This maximum is balanced by the left-of-center entropy so that $\{r\cos\phi\} = 0$. Due to the asymmetry in the initial distribution, the matter to the right of the maximum flows to the east with larger velocity, while the matter to the left of the maximum flows to the west with smaller velocity. Since there is more entropy to the left than to the right (relative to the maximum) the total momentum in the x direction is zero. This flow pattern leads to a $v_1(p_T)$ that satisfies a momentum conservation sum rule,

$$\int_0^\infty \frac{dN}{dp_T} v_1(p_T) p_T = 0\,. \tag{2.17}$$

At high p_T $v_1(p_T)$ is positive reflecting the fast matter to the right of the maximum, while at low p_T $v_1(p_T)$ is negative reflecting the slow (but abundant) matter to the left of the maximum. These qualitative features of the dipole flow are corroborated by numerical works [69, 88] and what has been observed in experiments [78, 89, 90], *e. g.*, seen in Fig. 3.3. Since the primary order of $m = 1$ asymmetry is eliminated, in our work the notation $\epsilon_1 = \mathcal{C}_{3,1}$ and $\Phi_1 = \Phi_{3,1}$ are used commonly for the dipole asymmetry.

2.2 Application of cumulant expansion

In the previous section we introduced a cumulant expansion to characterize the response of the system to a set of perturbations. In this section we will show the implementation of the cumulant formalism to initialize hydrodynamics, and study as well the convergence of the cumulant expansion.

Characterizing the initial energy density with cumulants

Rewriting Eq. (2.3) with cumulant expansion gives rises to the re-expression of a distribution with fluctuations, in terms of cumulants order by order.

$$\begin{aligned}\rho(\boldsymbol{x}_\perp) &= \int d^2\boldsymbol{k}_\perp e^{i\boldsymbol{k}_\perp\cdot\boldsymbol{x}_\perp} e^{\hat{W}_{2,0}+\hat{W}_{2,2}} \exp\left[\sum_{n>2,m} \hat{W}_{n,m}(\boldsymbol{k}_\perp)\right] \\ &= \rho_2(\boldsymbol{x}_\perp) + \sum_{n,m} \rho_{n,m}(\boldsymbol{x}_\perp) + \dots \,. \end{aligned} \tag{2.18}$$

In addition to the two lowest order terms $\rho_{2,0}$ and $\rho_{2,2}$, forming a background Gaussian distribution as expected,

$$\rho_2(\boldsymbol{x}_\perp) = \frac{1}{2\pi\sqrt{\{x^2\}\{y^2\}}} \exp\left[-\frac{x^2}{\{x^2\}} - \frac{y^2}{\{y^2\}}\right], \tag{2.19}$$

the terms with $n > 2$ introduce perturbations. The second equation in Eq. (2.18) is obtained by a further expansion of the exponential factor, followed by the Fourier transformation of each term. The background is determined by the quantities $\{x^2\}$ and $\{y^2\}$ or equivalently the rms radius $\{r^2\}$ and eccentricity, $\epsilon_2 = (\{x^2\} - \{y^2\})/(\{x^2\} + \{y^2\})$. Each additional term in Eq. (2.18) perturbs the background and the magnitude and type of perturbation is determined by the cumulants, i.e. ϵ_n and $\{r^n\}$. For instance, for a distribution with only dipole asymmetry with $\Phi_1 = 0$, we have

$$\rho(\boldsymbol{x}_\perp) \propto \left\{1 + \frac{\{r^3\}\epsilon_1}{8}\left[\left(\frac{\partial}{\partial x}\right)^3 + \left(\frac{\partial}{\partial y}\right)^2\left(\frac{\partial}{\partial x}\right)\right]\right\} e^{-\frac{r^2}{\{r^2\}}}, \tag{2.20}$$

and a distribution with only triangularity with $\Phi_3 = 0$,

$$\rho(\boldsymbol{x}_\perp) \propto \left\{1 + \frac{\{r^3\}\epsilon_3}{24}\left[\left(\frac{\partial}{\partial x}\right)^3 - 3\left(\frac{\partial}{\partial y}\right)^2\left(\frac{\partial}{\partial x}\right)\right]\right\} e^{-\frac{r^2}{\{r^2\}}}, \tag{2.21}$$

with an overall constant adjusted to reproduce the total initial entropy (for approximating initial entropy density) or energy (for approximating initial energy density). The trick of obtaining the differential operators in Eq. (2.20) and Eq. (2.21) is to write the spatial partial derivatives in accordance with the corresponding cumulant expansion form. Notice that each ik_x or ik_y in the cumulant expansion in Eq. (2.18) is related to a partial derivative of x or y on $e^{i\boldsymbol{k}_\perp\cdot\boldsymbol{x}_\perp}$, so that after integration by parts fluctuations of a distribution in coordinate space are expressed in terms of derivative operators on the Gaussian with a specified form.

To analyze the hydrodynamic response to a distribution with single or multiple perturbations, as we will detail in Chapter 3 for linear and nonlinear flow response, one problem encountered is that the distribution in Eq. (2.20) and (2.21) are negative for large radius. Take Eq. (2.20) as an example, the partial derivatives of a Gaussian for dipole asymmetry overwhelm the leading term when radius r grows large, resulting in a region with negative distribution, as shown schematically in Fig. 2.3. This is an unavoidable consequence of truncating a cumulant expansion at any finite order. As a result, a regulation scheme is necessary in our calculations for these fluctuation terms. Denoting the ratio of fluctuation terms in the distribution function to the background Gaussian as X, then the regulated form

$$X \to C\tanh(X/C) \tag{2.22}$$

is actually used in applications, with the constant $C = 0.95$. We have checked that the results are independent of the precise value of the constant C. The regulator here is not perfect as it (weakly) mixes different terms in the Fourier expansion, and modifies to a slight extent the input value of eccentricity and the "true" value the initial distribution actually has. However we have found this mixing to be unimportant from a practical perspective, that is, as long as the input value of eccentricity is sufficiently small. For instance if $\epsilon_3 = 0.05$ the generated flow for different orders is negligible. Meanwhile, the relative difference of the input and the "true" value of eccentricity can be constrained as small as a few percents.

Convergence of cumulant expansion for smooth Glauber

The convergence of the cumulant expansion, in particular from the point of view of applications to the fluctuating initial state and hydrodynamics, is in principle a problem beyond the scope of this work. However, in a simplified manner, a test can be carried out for one specified initial condition. For a smooth (optical) Glauber profile we replace the initial entropy distribu-

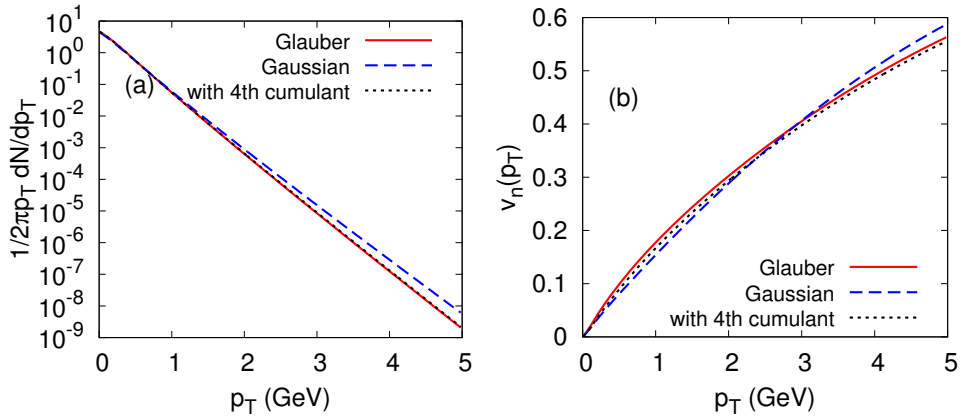

Figure 2.4: (a) Spectra in the smooth (optical) Glauber model compared to the cumulant expansion. The coefficients of the Gaussian and fourth-order cumulant expansions have been adjusted to reproduce $\{r^2\}$, $\{r^2\cos 2\phi_r\}$ and $\{r^4\cos 2\phi_r\}$, $\{r^4\cos 4\phi_r\}$, respectively. The total entropy of the cumulant expansion is also matched to the total entropy of the Glauber distribution. (b) Elliptic flow in the Glauber model compared to the cumulant expansion.

tion with an approximately Gaussian profile and cumulant corrections through fourth order, $n = 4$. The distribution of entropy in the optical Glauber model is first used to calculate $\{r^2\}$ and ϵ_2, which consequently determine the two coefficients in the Gaussian, $\{x^2\}$ and $\{y^2\}$. Also the normalization (*i. e.*, the total entropy) is the same between the Gaussian and the Glauber distribution. Taking the impact parameter to be b = 7.6 fm, with ideal hydrodynamics Fig. 2.4 compares the spectra and the elliptic flow for these two distributions. In the next approximation, the fourth cumulants to the Gaussian are adjusted as described in the previous section, so that the quantities $\{r^4\}$, $\{r^4\cos 2\phi_r\}$ and $\{r^4\cos 4\phi_r\}$ are identified to the results of the optical Glauber.

An obvious trend of convergence is presented in Fig. 2.4 as the distribution with fourth order cumulants already reproduces the flow response to the corresponding Glauber. Since ideal hydrodynamics generates the most sensitive flow response to the initial state geometry, the test here demonstrates the applicability of cumulant expansion formalism. Future test can be carried out with respect to more realistic initial density profile with random fluctuations.

2.3 Monte Carlo simulations of the initial state

Since the essence of the single-shot hydrodynamics is the assumed one to one mapping, from the initial state profile to the observed spectrum, in this section we estimate the initial state eccentricities and their correlations based on our cumulant definitions, using the PHOBOS Monte Carlo Glauber code[8].

Eccentricity

With respect to the way in which harmonic flow is measured in experiment, there are a handful of definitions of averaged initial eccentricities. For instance, corresponding to the measured harmonic flow $v_n\{2\}$ by two-particle correlation method, $\epsilon_n\{2\}$ is defined as

$$\epsilon_n\{2\} = \sqrt{\langle\langle \epsilon_n^2 \rangle\rangle}\,, \tag{2.23}$$

where $\langle\langle \ldots \rangle\rangle$ denotes the events average. In Fig. 2.5, with Monte Carlo simulations, $\epsilon_n\{2\}$ of harmonic order $n \leq 5$ are calculated, as a function of number of participants for LHC Pb-Pb collisions. To obtain a satisfactory convergence, 2 million events are accumulated in these PHOBOS MC-Glauber simulations.

The first observation of these simulations is the monotonic increase of all these eccentricities with respect to collision centrality. For ellipticity this is intuitively understandable since the overlap region becomes narrower when centrality grows, and therefore a larger ellipticity generated from the almond-shape background. However, for these very central collisions, where the background is roughly spherically symmetric, a non-zero $\epsilon_2\{2\}$ is dominantly generated from fluctuations. This non-zero $\epsilon_2\{2\}$ of central collisions results in the observed non-zero elliptic flow $v_2\{2\}$ [91, 92]. For the other eccentricities, background shape contributions to the formation of azimuthal deformations are relatively small, the rise of ϵ_n towards peripheral collisions reflects the increasing influence of fluctuations. In particular, we see that the dipole asymmetry is about a factor of 2 smaller than the triangularity but is not negligibly small. For the harmonic order $n \geq 4$, the extra underlined terms in Eq. (2.13) in the cumulant definition bring in corrections of quadratic nonlinear mixing of lower order eccentricities, leading to modifications to the simulated results. As shown in Fig. 2.5, the difference between the moment defined 4-th order and 5-th order eccentricities, and the corresponding cumulant defined ones, grows with centrality as expected. Though it is noticeable in peripheral collisions, the effect of taking cumulant definitions for the eccentricities is not significant.

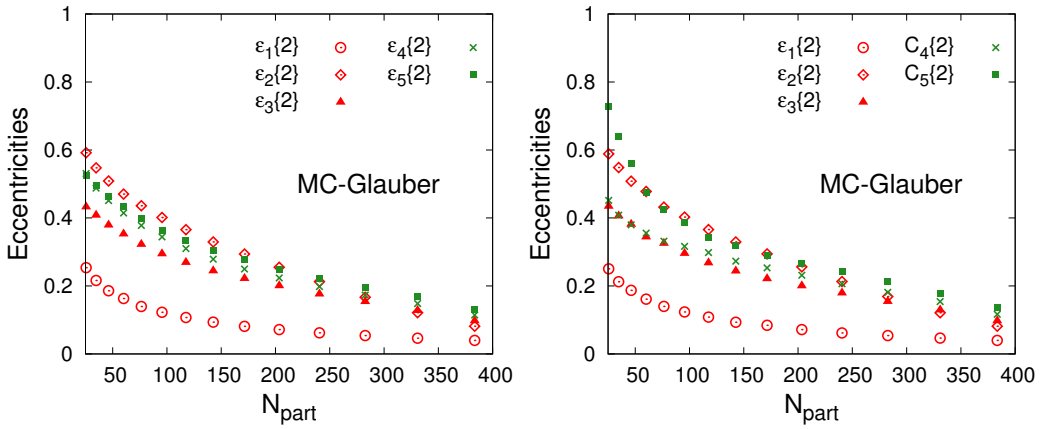

Figure 2.5: Eccentricities from Monte Carlo Glauber simulations for LHC Pb-Pb collisions. The momentum based (the left figure) and the cumulant based (the right figure) definitions result in differences that grows with centrality, for the higher order eccentricities.

Initial state participant plane correlation

In addition to the magnitude of these anisotropies, the corresponding participant angles Φ_n and their correlations, reveal another aspect of the initial state geometry with fluctuations.

As defined in Eq. (2.14), except that the associated participant angle Φ_2 of ϵ_2 are dominated by the almond shape, Φ_n are entirely determined by fluctuations. Therefore, on an event-by-event basis, the orientations of Φ_n depend on specifically the details of the initial distribution in each heavy-ion collision event. However on an event-by-event basis, as has been discussed in [93], in which initial state fluctuations are modelized as hot spots, fluctuations in the initial geometry lead to non-trivial correlations among different types of participant plane angles. Generally, to characterize the correlations among Φ_n of initial state (and Ψ_n of final state as will be stated in later sections), we analyze the event averaged cosine function $\langle\langle\cos(c_1\Phi_1 + c_2\Phi_2 + \ldots + c_l\Phi_l)\rangle\rangle$. Due to the n-fold rotational symmetry of n-th order of anisotropy, and the reflection symmetry, the integer coefficients c_l modes l, satisfying

$$c_1 + 2c_2 + \ldots + lc_l = 0\,. \tag{2.24}$$

Obviously, non-zero value of the event averaged $\langle\langle\cos(c_1\Phi_1+c_2\Phi_2+\ldots+c_l\Phi_l)\rangle\rangle$ indicates non-trivial correlations, and the closer the value to 1 (or -1 for anti-correlation), the stronger the correlation is. Note taking different convention

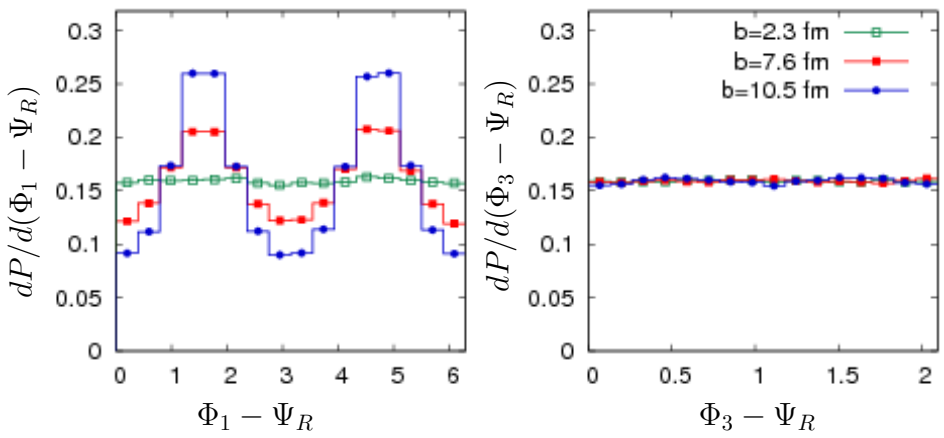

Figure 2.6: Distribution of the angles Φ_1 and Φ_3 with respect to the reaction plane for three different impact parameters

for the angle Φ_n definition, *i. e.*, taking the shorter or longer axis as the defined angle direction, leads to a minus sign for odd number plane correlations.

Without specifying an effective model as [93], in this section we try to detail the origin of these initial plane correlations by the two particular examples, two-plane correlation $\langle\langle\cos 2(\Phi_1 - \Psi_R)\rangle\rangle$ and three-plane correlation $\langle\langle\cos(\Phi_1 - 3\Phi_3 + 2\Psi_R)\rangle\rangle$. As mentioned in Section 1.3, Ψ_R defines the so-called reaction plane of collision, which precisely coincides with the participant plane of ellipticity Φ_2 for a smooth initial state. On an event-by-event basis, however, Φ_2 fluctuates around Ψ_R with finite deviations. Since the deviations are actually negligible for most of the centralities, in this work we take $\Phi_2 \equiv \Psi_R$.

In Fig. 2.6 the correlations between Φ_1 and Ψ_R, and Φ_3 and Ψ_R are exhibited in terms of the probability distribution function, at various impact parameters. The angle range is selected by taking into account the corresponding periodicity. There is a pronounced trend of increasing correlation between Φ_1 and Ψ_R, from central to non-central collisions, peaking at $\Phi_2 - \Psi_R = \pi/2$ and $3\pi/2$. As a consequence of the (Φ_1, Ψ_R) correlation, on an event-by-event basis relative to the orientation of Φ_2, the dipole asymmetry is preferred to be out-of reaction plane. If expressing the correlation in terms of a cosine function form, *i. e.* studying $\langle\langle\cos 2(\Phi_1 - \Phi_2)\rangle\rangle$, we should expect a negative result, as shown in Fig. 2.7. Naively, we can think of the non-trivial (Φ_1, Ψ_R) correlation as a pure geometric effect, since there is a larger chance for the imbalance to be induced by fluctuations on top of a smaller and narrower almond shape, along the long axis than the shorter one. For (Φ_3, Ψ_R), although the direct

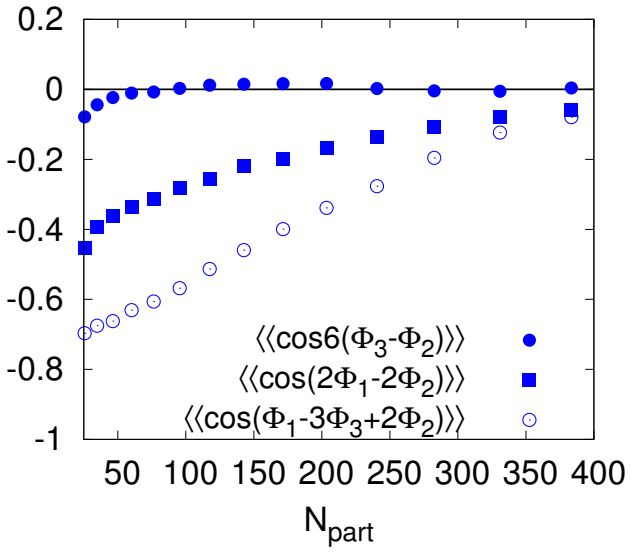

Figure 2.7: Initial participant plane correlation functions, from MC-Glaber simulations for RHIC Au-Au collisions.

two-plane correlation is mostly negligible[2], as can be seen in Fig. 2.6, through Φ_1 a strong three-plane correlation $\langle\langle\cos(\Phi_1 - 3\Phi_3 + 2\Phi_2)\rangle\rangle$ is formed, as shown in Fig. 2.7. The strong correlation may be explained physically as follows. When the dipole asymmetry is in plane then the triangular axis is at $\pi/3$, i.e. the point of the triangle is aligned with the dipole asymmetry as exhibited in Fig. 2.8(a). However, when the dipole axis is out of plane then the triangular axis is also out of plane as exhibited in Fig. 2.8(b). Note that in these special configurations, $\cos(\Phi_1 - 3\Phi_3 + 2\Phi_2) = -1$.

Fit and simple interpretations

These correlations are a reflection of the almond shape geometry and the general form can be established by symmetry arguments. First since the probability of finding a dipole asymmetry in a given quadrant of the ellipse is the same for every quadrant, the probability distributions $dP/d(\Phi_1 - \Psi_R)$ must only involve even cosine terms

$$\frac{\mathrm{d}P}{\mathrm{d}\Phi_1} = \frac{1}{2\pi}\left[1 - 2A\cos 2(\Phi_1 - \Psi_R) + \ldots\right] \tag{2.25}$$

[2]In fact, for very peripheral collisions a slight peak of the probability distribution at $\Phi_3 - \Psi_R = \pi/6$ and $\pi/2$ can be observed. However, ignoring this weak correlation will not alter the analysis in this section.

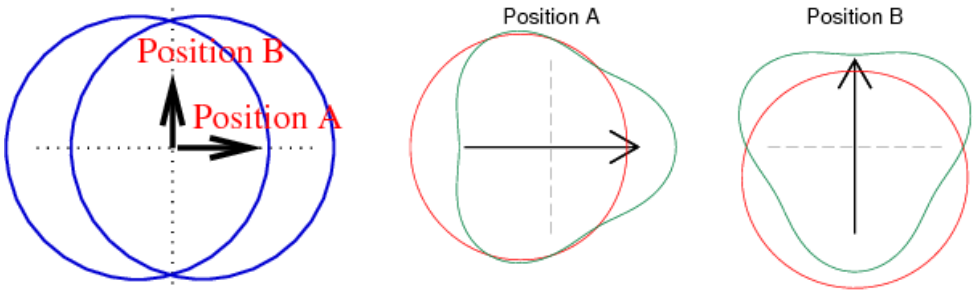

Figure 2.8: Geometric alignment of triangularity, dipole and ellipticity
When the dipole asymmetry is in plane (Position A), then the tip of triangularity is aligned with dipole asymmetry. When the dipole asymmetry is out of plane (Position B), the tip of the triangle is anti-aligned with the dipole asymmetry.

The sign has been chosen so that a positive A coefficient describes the out of plane preference seen in Fig. 2.6. The coefficient A must vanish in a cylindrically symmetric collision, and for small anisotropy we expect

$$A \propto \langle\langle \epsilon_2 \rangle\rangle \,. \tag{2.26}$$

Similarly $\mathrm{d}P/\mathrm{d}(\Phi_3 - \Psi_R)$ must involve even cossine terms and must be $2\pi/3$ periodic

$$\frac{\mathrm{d}P}{\mathrm{d}(\Phi_3 - \Psi_R)} = \frac{1}{2\pi}\left[1 + 2A_6 \cos 6(\Phi_3 - \Psi_R) + \ldots\right] \tag{2.27}$$

The relatively high Fourier number n = 6 explains the smallness of the observed asymmetry, and to the lowest order A_6 can be ignored.

For the analysis of the three-plane correlation between Φ_1, Φ_3 and Ψ_R, we need to introduce the conditional probability distribution,

$$P(\Phi_3|\Phi_1, \Psi_R) \equiv \text{The probability of } \Phi_3 \text{ given } \Phi_1 \text{ and } \Psi_R \,. \tag{2.28}$$

For any fixed value of Φ_1, the periodicity of Eq. (2.28) must follow Φ_3 to be $2\pi/3$. Thus measuring all angles with respect to the reaction plane Ψ_R, and keeping only the first nontrivial term in the Fourier series we have

$$P(\Phi_3|\Phi_1, \Psi_R) = \frac{1}{2\pi}\left\{1 + 2B\cos[3(\bar{\Phi}_3 - \Psi_R) - (\phi^* - \Psi_R)]\right\} \tag{2.29}$$

The amplitude B and the phase ϕ^* are functions of $\Phi_1 - \Psi_R$, so we can have

further expansion of B and the phase derivatives ,

$$B = B_0 + 2B_2 \cos(2\bar{\Phi}_1)\,, \tag{2.30a}$$

$$\frac{\mathrm{d}\phi^*}{\mathrm{d}\bar{\Phi}_1} = C_0 + 2C_2 \cos(2\bar{\Phi}_1)\,, \tag{2.30b}$$

where $\bar{\Phi}_1 = \Phi_1 - \Psi_R$. As the Φ_1 increases by 2π , the phase ϕ^* must change by a multiple of 2π to leave the conditional probability distribution invariant. The simplest possibility which qualitatively describes the trends illustrated in Fig. 2.8 and Fig. 2.9 is to take $C_0 = 1$. In a general Fourier series of two variables other possibilities would be allowed, for example, $C_0 = 3$. However, such correlations turn out to be small in the Glauber model. Integrating Eq. (2.30b) we find

$$\phi^* = \Phi_1 + C_2 \sin(2\bar{\Phi}_1) + \text{constant} \tag{2.31}$$

The constant required to reproduce Fig. 2.8 is π. The combination of Eq. (2.29), (2.30a), and (2.31) leads to the following parametrization,

$$P(\Phi_3|\Phi_1, \Psi_R) = \frac{1}{2\pi}\left\{1 - 2[B_0 - 2B_2 \cos 2(\Phi_2 - \Psi_R)\cos(3\Phi_3 - \phi^* - 2\Psi_R)\right\}\,, \tag{2.32}$$

in which the angle combination $\Phi_1 + 2\Phi_2 - 3\Phi_3$ indeed appears. In Eq. (2.32) we absorbed the constant phase π in ϕ^* into the leading minus sign of B_0 and B_2 and changed the sign of C_2 so that all coefficients are positive in the final fit. Fig. 2.9 shows a fit to the Monte Carlo Glauber at $b = 7.6$ fm using this parametrization. The fit does capture most of the essential features, but fails to reproduce the sharpness of the correlation band.

Finally, we can estimate the scaling of these coefficients with the average elliptic eccentricity $\langle\langle\epsilon_2\rangle\rangle$. In a central collision $P(\Phi_1, \Psi_R)$ must vanish. This can be understood by examining Fig. 2.8 and recognizing that in a central collision there is no distinguishable difference between position A and position B. The coefficient of $\cos(3\Phi_3 - \phi^* - 2\Psi_R)$ (*i. e.*, B) describes how phase between the triangular and the dipole planes changes from position A to position B. This coefficient must vanish in central collisions where position A and position B are identical. Finally the coefficients B_2 and C_2 reflect the almond shape and must involve an additional power of $\langle\langle\epsilon_2\rangle\rangle$ relative to C_0 and B_0. With these remarks we arrive at the scalings,

$$B_0 \propto \langle\langle\epsilon_2\rangle\rangle, \quad B_2 \propto \langle\langle\epsilon_2\rangle\rangle^2, \quad C_2 \propto \langle\langle\epsilon_2\rangle\rangle,. \tag{2.33}$$

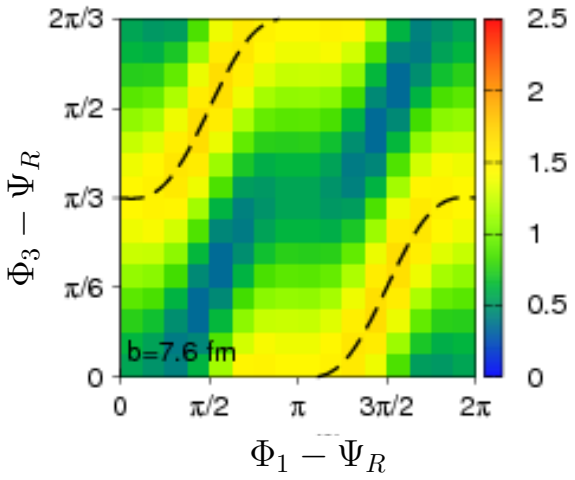

Figure 2.9: The conditional probability distribution $P(\Phi_3|\Phi_1, \Psi_R)$ for impact parameter $b = 10.5$ fm. The dashed curves are fit with parameter $C_2 = -0.53$.

Some results of initial two-plane and three-plane correlations

More systematically, as a generalization of the discussion above, we investigate the initial two-plane and three-plane correlations, with respect to the recent results of event plane correlations measured by ATLAS collaboration for Pb-Pb collisions [7]. The simulations in this section are done using PHOBOS Glauber model. Other effective models, such as MC-KLN [94] and MC-Glissando [9], can also be taken into account, but does not change our conclusions.

Shown in Fig. 2.10 and Fig. 2.11, strong correlations, such as the correlations between (Φ_4, Φ_2), are obtained from PHOBOS Glauber simulations. Except the correlation $\langle\langle\cos 6(\Phi_3 - \Phi_2)\rangle\rangle$, in which higher order anisotropies are not involved, the cumulant defined and moment defined participant plane correlations are different. For example, the negative $\langle\langle\cos(4\Phi_4 - 4\Phi_2)\rangle\rangle$ reflects a strong anti-correlation, while the corresponding correlations $\langle\langle\cos(4\Phi_4^c - 4\Phi_2)\rangle\rangle$ is positive. Similarly, a sign difference can also be found in the two-plane correlation (Φ_2, Φ_6) and three-plane correlation (Φ_2, Φ_3, Φ_5) *etc.*.

To understand the difference between the cumulant and moment definitions in terms of the angle correlations, we take (Φ_4, Φ_2) as an example. In the moment definition, this negative result can be expected because the fourth order eccentricity ϵ_4 is trivially anti-correlated with the second order eccentricity ϵ_2. These trivial geometric correlations are removed with the cumulant definition by the subtraction of the nonlinear terms. Recall the cumulant definition of

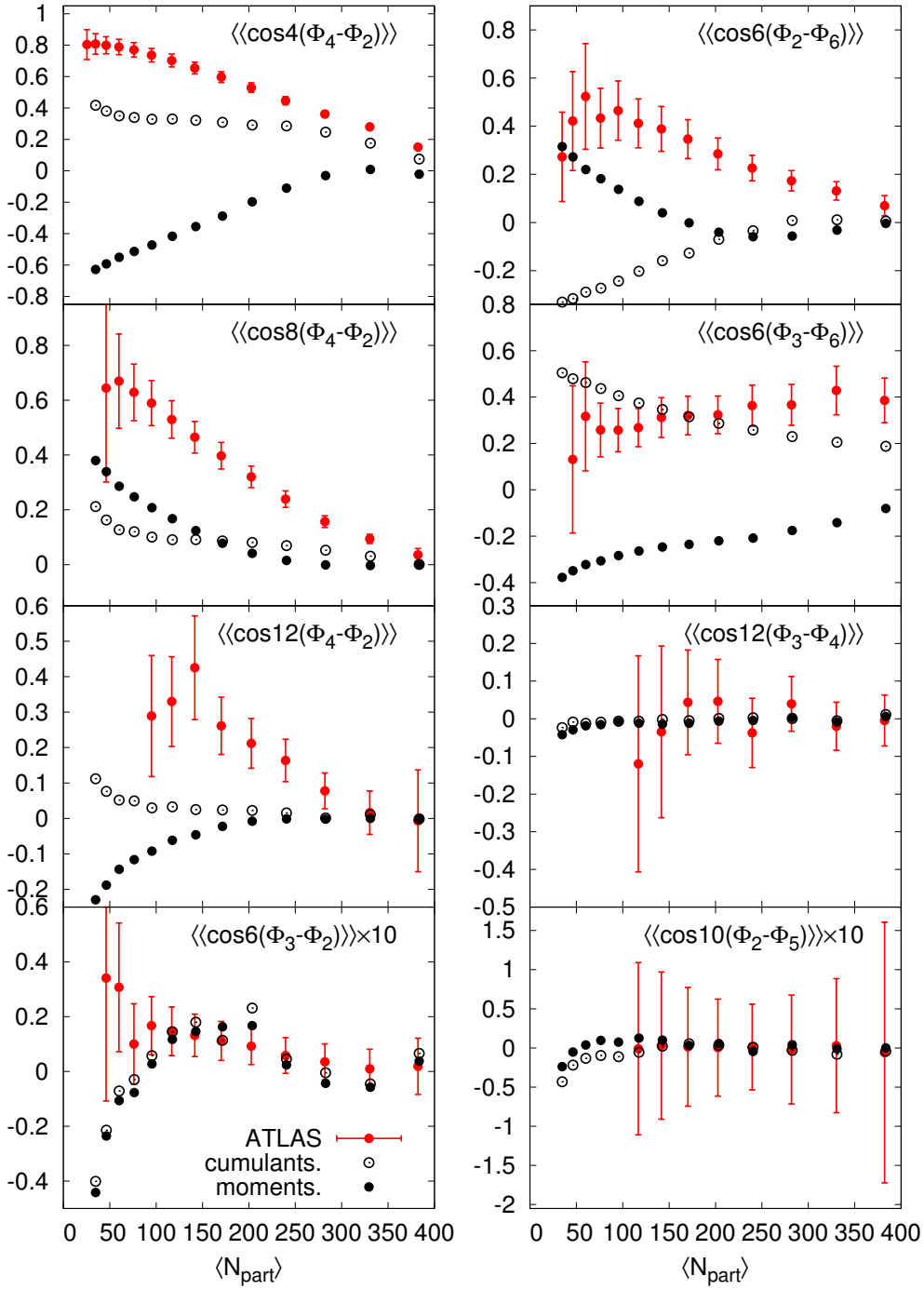

Figure 2.10: Initial state two-plane correlations of LHC Pb-Pb collisions Initial state two-plane participant plane correlations from PHOBOS MC-Glauber model. The corresponding event plane correlations measured by ATLAS collaboration [7] are shown for comparisons.

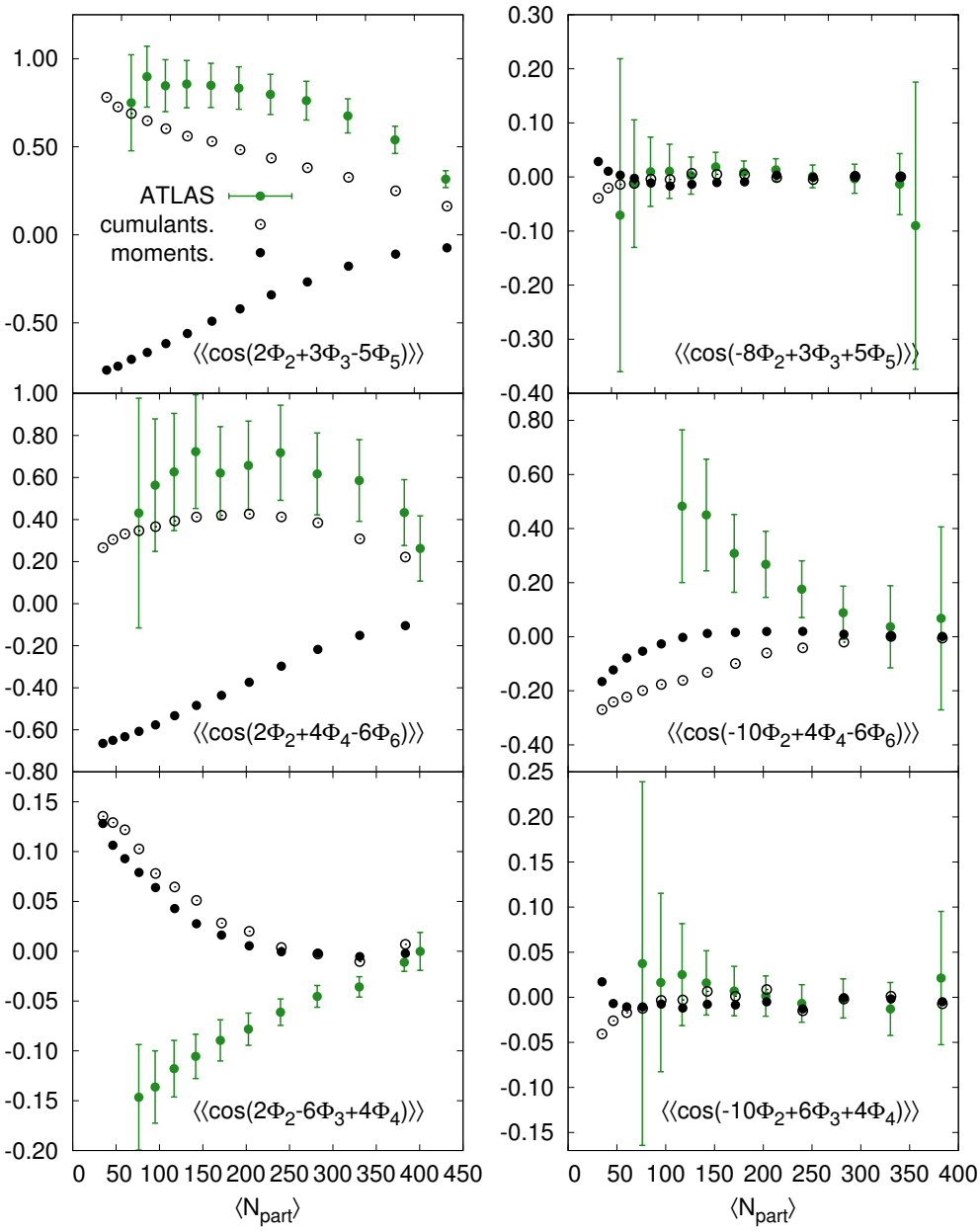

Figure 2.11: Initial state three-plane correlations of LHC Pb-Pb. Initial state three-plane participant plane correlations from PHOBOS MC-Glauber model. The corresponding event plane correlations measured by ATLAS collaboration [7] are shown for comparisons.

4-th order anisotropy,

$$\mathcal{C}_4 e^{i4\Phi_4^c} = -\frac{[\{\bar{r}^4\} - 3\{\bar{r}^2\}^2]}{\{r^4\}} = \epsilon_4 e^{i4\Phi_4} + 3\left[\epsilon_2 e^{i2\Phi_2}\right]^2 (1+\delta)\,, \tag{2.34}$$

where δ characterizes the deviation from a pure Gaussian background. In the limit of a pure Gaussian without any perturbations, Eq. (2.34) leads to $\mathcal{C}_4 = 0$ and $\epsilon_4 = 3\epsilon_2^2$, and a perfect anti-correlation $\Phi_4 - \Phi_2 = \pi$. When non-Gaussian effects are taken into account from the realistic Glauber background, we should expect the correction leads to a positive δ. As a result, non-trivial positive correlations between (Φ_4^c,Φ_2) are deduced, *i. e.*,

$$\begin{aligned}\cos 4(\Phi_4^c - \Phi_2) &\sim \epsilon_4 \cos 4(\Phi_4 - \Phi_2) + 3\epsilon_2^2(1+\delta) \\ &\sim 3\epsilon_2^2 \left[\cos 4(\Phi_4 - \Phi_2) + 1 + \delta\right]\,. \end{aligned} \tag{2.35}$$

This crude geometric analysis explains the correlation of $\langle\langle\cos 4(\Phi_2 - \Phi_4^c)\rangle\rangle$ and the anti-correlation of $\langle\langle\cos 4(\Phi_2 - \Phi_4)\rangle\rangle$. Furthermore, the sign flipping from $\langle\langle\cos 4(\Phi_2 - \Phi_4)\rangle\rangle$ to $\langle\langle\cos 8(\Phi_2 - \Phi_4)\rangle\rangle$ and $\langle\langle\cos 12(\Phi_2 - \Phi_4)\rangle\rangle$ can also be understandable in the similar way.

Nevertheless, these initial participant plane correlations are not compatible to the ATLAS measurements.

Discussion

We hope that the cumulant expansion presented in this chapter organizes and formalizes the study of initial state fluctuations in heavy-ion collisions. The convergence of the cumulant expansion is sufficiently good as illustrated in Fig. 2.4 for a smooth Glauber, test with respect to a fluctuating initial profile is left for future studies. In the cumulant expansion formalism, the anisotropies are systematically defined. In particular, we found in the third cumulant, $W_{3,1}$ describes the rapidity-even dipole asymmetry. The formulation of the cumulant expansion in Section 2.1 is constrained in the 2-dimensional transverse plane. A generalized discussion in the 3-dimensional space, containing also the η_s dependence, can be found in Appendix B.

Initial state participant plane correlations were analyzed using Monte Carlo Glauber simulations. In particular, We find that in non-central collisions the dipole asymmetry is preferentially out of plane leading to a v_1 out of plane. We also noted the strong correlation between the dipole asymmetry, ellipticity and the triangularity. A pure geometric explanation for the $\langle\langle\cos(\Phi_1 + \Phi_2 - 3\Phi_3)\rangle\rangle$ was proposed. Although the simulated magnitude of these eccentricities from the cumulant definitions are found not quite different from the moment defi-

nitions, effects of cumulant definition on initial participant plane correlations are significant. In Fig. 2.10 and Fig. 2.11, with cumulant and moment definitions, even a sign difference can be found, *e. g.* the correlation (Φ_4, Φ_2). On a geometric ground, the obtained results of these initial plane correlation can be understood. In our work, other effective models, such MC-KLN [94] and MC-Glissando [9] can also be applied for initial participant plane correlations, but still fail to explain the experiment results in Fig. 2.10 and Fig. 2.11.

Chapter 3

Flow response

In the previous chapter we discussed the initial state fluctuations. In particular we analyzed the initial state participant plane correlations using the cumulant expansion. comparing the final state correlations [7] to the initial state correlations in Fig. 2.10 and Fig. 2.11 have shown significant differences, suggesting that the medium response to the initial perturbations is nontrivial. To improve these theoretical predications, and to approach a better understanding of flow generation in heavy-ion collisions, in this chapter we will analyze the medium response in details.

The medium response to the initial state anisotropy can be characterized by flow response coefficients. As will be clarified later, the flow response coefficient,

$$\text{flow response coefficient} = \frac{\text{observed flow}}{\text{initial state information}} \tag{3.1}$$

quantifies the mapping from the initial state to the final state observations. Thus in the flow response formalism, the predicted observables, such as harmonic flow $v_n\{2\}$, can be factorized in terms of flow response coefficients (which are studied in this chapter) and initial state anisotropies (which were studied in the previous chapter). There is strong experimental and theoretical evidence that the harmonic flow, v_2 and v_3, are to a good approximation linearly proportional to the corresponding deformations in the initial entropy density in the transverse plane. In general, flow response coefficients, and thus the mapping from the initial state and the final state, can be analyzed as a function of the medium properties. In Section 3.1 we review and investigate the linear flow response formalism. The dependence of the linear flow response coefficient on collision centrality, transverse momentum and η/s are analyzed based on ideal and viscous hydrodynamic simulations of heavy-ion collisions.

In an insightful paper Gardim *et al* [95] studied the correlation between higher harmonics, v_4 and v_5, and the initial spatial deformations within ideal hydrodynamics. This work explained and quantified the extent to which the higher harmonics such as v_4 and v_5 arise predominantly from the nonlinearities of the medium response. For example, for mid-central collisions the observed v_5 is predominantly a result of the interactions between v_2 and v_3. In [85], Heinz and Qiu investigated the linear relation between harmonic flow v_n and initial eccentricity ϵ_n, using event-by-event ideal hydrodynamics. They find that the elliptic flow v_2 and triangular flow v_3 are linearly proportional to ϵ_2 and ϵ_3 from very central ($b = 0$ fm) to very peripheral collisions [1]. However, for v_4 and ϵ_4 , and v_5 and ϵ_5, a simple linear relation is not found. In addition, it is also confirmed from the comparison of the linear flow response coefficients between their event-by-event hydrodynamic and single-shot hydrodynamic calculations. These analyses suggest the necessity of considering the nonlinearities in the medium expansion.

Thereby, as an extension to the linear flow response, by considering nonlinear mode mixing of the harmonics, we construct the nonlinear flow response formalism. The nonlinear generation of harmonics can thus be described in the nonlinear flow response formalism, with the formulation shown in Section 3.2. With the nonlinear response coefficients systematized, as a function of transverse momentum, centrality and η/s, the medium response formalism is applied for realistic predictions. A simple discussion is made in Section 3.3.

3.1 Linear flow response

In this section, we briefly review the concept of linear flow response in heavy-ion collisions, and test its applicability. In linear response, a linear relation between the observed harmonic flow and the initial azimuthal anisotropy is assumed

$$v_n e^{in\Psi_n} = \frac{w_n}{\epsilon_n} \times \left(\epsilon_n e^{in\Phi_n}\right) . \tag{3.2}$$

In Eq. (3.2), the associated observables of order n, *i. e.* harmonic flow v_n and event plane angle Ψ_n, are written compactly in a complex form, which parallels the description of initial state fluctuation in the bracket on the right hand side (r.h.s.) of the equation. The linear relation in Eq. (3.2) defines a linear response coefficient, w_n/ϵ_n. Note we have specified the notation w_n for

[1] For the very peripheral bins, there is a slight deviation from the linearity between v_3 and ϵ_3.

the linearly generated n-th order harmonic flow, instead of v_n. Accordingly w_n/ϵ_n is used to symbolize the linear flow response coefficient.

Following the strategy in Section 2.2, the initial geometric deformation is characterized by the cumulant expansion form Eq. (2.18). For calculating the linear response of harmonic order n, we introduce the corresponding deformation by the input eccentricities $\epsilon_n = 0.05$ and $\epsilon_m = 0$ if $m \neq n$, on a spherically symmetric Gaussian background. Hydrodynamics describes the medium expansion with respect to the specified initial condition, and the linearly generated flow v_n is calculated. To quantify the linear flow response coefficient precisely, the output initial eccentricity $\epsilon_n^{\text{output}}$ is taken so that $w_n/\epsilon_n = v_n/\epsilon_n^{\text{output}}$. In our calculations, the participant plane angle Φ_n of the initial profile is taken to be aligned with the reaction plane Ψ_R for simplicity.

3.1.1 Flow development during the medium expansion

The medium expansion in heavy-ion collisions is a process that transform the initial state spatial anisotropy to the observed anisotropic flow in final state momentum space. The generation of the momentum anisotropy can be seen by investigating the evolution of the medium profile, especially the flow velocity profile.

Evolution of eccentricities

Driven by the gradient anisotropy, the bulk evolves with respect to a specified initial state geometry. Accordingly, the spatial anisotropy is transformed into momentum space and the harmonic flow develops. As a result, in the linear flow response formalism, for each harmonic order n, we should expect the decreasing of spatial eccentricities ϵ_{nx} and the increasing of momentum anisotropy ϵ_{np}, as a function of evolution time during the bulk expansion. In this section, we will explicitly label x in the subscript of the spatial eccentricity to distinguish it from the momentum anisotropy. Corresponding to ellipticity, the second order momentum anisotropy is traditionally defined as

$$\epsilon_{2p} = \frac{\int d^2\boldsymbol{x}\,(T^{xx} - T^{yy})}{\int d^2\boldsymbol{x}\,(T^{xx} + T^{yy})} = \frac{\int d^2\boldsymbol{x}(\varepsilon + \mathcal{P})u_r^2 \cos 2\phi_u}{\int d^2\boldsymbol{x}\,[(\varepsilon + \mathcal{P})u_r^2 + 2\mathcal{P}]}\,, \tag{3.3}$$

where $u_r = \sqrt{u_x^2 + u_y^2}$ and $\phi_u = \tan^{-1}(u^y/u^x)$ define the geometric profile in the flow velocity space. However, the numerators and denominators in Eq. (3.3) do not have manifest covariance under transverse boosts. To remedy this flaw, we first write the measure in these integrals as the fluid three volume in the local rest frame $d\Sigma_\mu u^\mu = d^2\boldsymbol{x}d\eta\tau u^0$. Then projecting to the transverse

plane, we introduce the new definition

$$\epsilon_{2p} \equiv \frac{\int d^2\boldsymbol{x}\tau u^0(\varepsilon+\mathcal{P})u_r^2\cos 2\phi_u}{\int d^2\boldsymbol{x}\tau u^0\left[(\varepsilon+\mathcal{P})u_r^2+\varepsilon\right]} = \frac{\int d^2\boldsymbol{x}\tau\left[T^{0(}u^{x)}-\text{traces}\right]}{\int d^2\boldsymbol{x}\tau\left[T^{00}u^0\right]}\,. \tag{3.4}$$

which is slightly different from Eq. (3.3). Note in the second equation of Eq. (3.4), the numerator has been re-expressed in terms of an irreducible rank two tensor out of momentum density T^{0j} and flow velocity u^j,

$$T^{0(i}u^{j)}-\text{traces} \equiv \frac{1}{2}\left(T^{0i}u^j+T^{0j}u^i-\delta^{ij}T^{0l}u_l\right)\,. \tag{3.5}$$

Eq. (3.4) and the relation Eq. (3.5) for second order anisotropy can be extended, to define any order of anisotropy in the momentum space. For example, corresponding to dipole asymmetry ϵ_{1x} and triangularity ϵ_{3x}, we have the third order tensor,

$$T^{(0i}u^ju^{l)} = \frac{1}{3!}(T^{0i}u^ju^l-\text{perms})\,, \tag{3.6}$$

The irreducible form of this tensor is used to define triangular anisotropy in momentum space,

$$\epsilon_{3p} \equiv \frac{\int d^2\boldsymbol{x}\tau\left[T^{0(x}u^xu^x)-\text{traces}\right]}{\int d^2\boldsymbol{x}\tau\left[T^{00}u^0u^0\right]} = \frac{\int d^2\boldsymbol{x}\tau u^0\left[(\varepsilon+\boldsymbol{p})u_r^3\cos 3\phi_u\right]}{\int d^2\boldsymbol{x}\tau T^{00}u^0u^0}\,, \tag{3.7}$$

The trace is used to define the dipole asymmetry in momentum space,

$$\epsilon_{1p} \equiv \frac{\int d^2\boldsymbol{x}\delta_{ij}T^{0(x}u^iu^{j)}}{\int d^2\boldsymbol{x}\tau T^{00}u^0u^0} = \frac{\int d^2\boldsymbol{x}\tau u^0\left[(\varepsilon+\boldsymbol{p})u_r^3\cos\phi_u\right]}{\int d^2\boldsymbol{x}\tau T^{00}u^0u^0}\,. \tag{3.8}$$

Armed with these definitions, Fig. 3.1 illustrates the development of the triangular flow and the dipole asymmetry as a function of time. As is familiar from studies of the elliptic flow [30, 33], the spatial anisotropy decreases leading to a growth of the momentum space anisotropy. When the spatial anisotropy crosses zero, the growth of the momentum space anisotropy stalls. The figures also indicate that the elliptic flow, the dipole asymmetry, and the triangularity all develop on approximately the same time scale $\tau \simeq \sqrt{\langle r^2\rangle}/c_s$, where c_s is the speed of sound. It is interesting to note the major contribution to the harmonic flow is from the QGP phase of the expanding medium (the first several fm/c in Fig. 3.1).

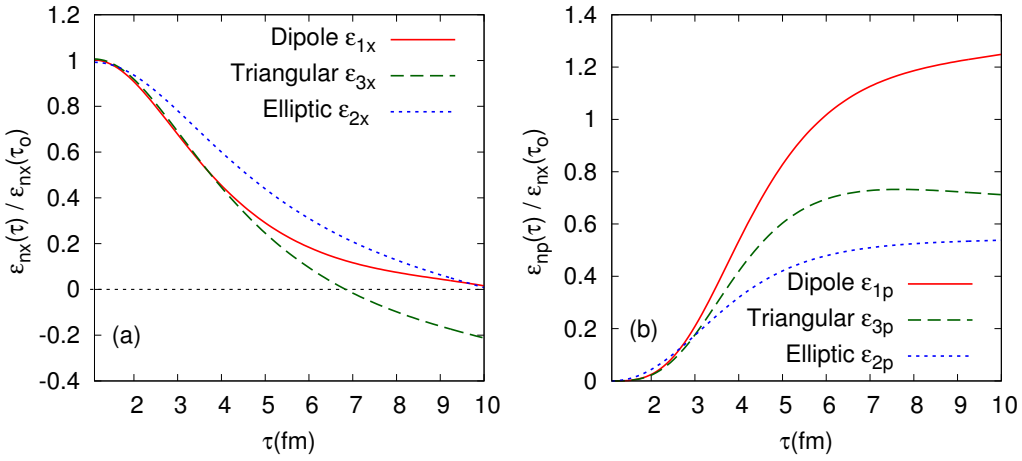

Figure 3.1: (a) The spatial anisotropy of the entropy distribution ϵ_{1x} , ϵ_{2x} , and ϵ_{3x} (see text) as a function of time for $b = 7.6$ fm. (b) The momentum anisotropy ϵ_{1p}, ϵ_{2p} , and ϵ_{3p} (see text) as a function of time. The time scale in these figures should be compared to $\sqrt{\{r^2\}}/c_s \simeq 5.4$ fm.

Evolution of flow velocity profile

Another important aspect of the flow is the radial flow profiles. To illustrate this we decompose the transverse flow velocity into harmonics [2]

$$u_r(r,\phi_r) = u_r^0(r) + u_r^{(1)}(r)\cos(\phi_r) + u_r^{(2)}(r)\cos(2\phi_r) + u_r^{(3)}(r)\cos(3\phi_r) + \dots \tag{3.9}$$

For a radially symmetric Gaussian distribution only the transverse flow $u_r^{(0)}$ is present and shows a characteristic linearly rising flow profile. When an elliptic deformation is added, the second harmonic also shows a linearly rising profile. Close to the origin, this behaviour can be understood with a linearized analysis of acoustic waves in a flowing background. The flow velocity in an acoustic analysis is the gradient of a scalar function Φ which can also be expanded in harmonics

$$\Phi(r,\phi_r) = \Phi^{(0)}(r) + \Phi^{(2)}(r)\cos 2\phi_r + \dots . \tag{3.10}$$

[2]For a initial state with random fluctuations, the corresponding flow velocity profile has non-trivial dependence on the participant plane angles Φ_n, which should be included in the decomposition as in Eq. (3.22) in a more serious manner. In this section, regarding the analysis of the development of flow velocity, neglecting the Φ_n dependence does not affect the conclusions.

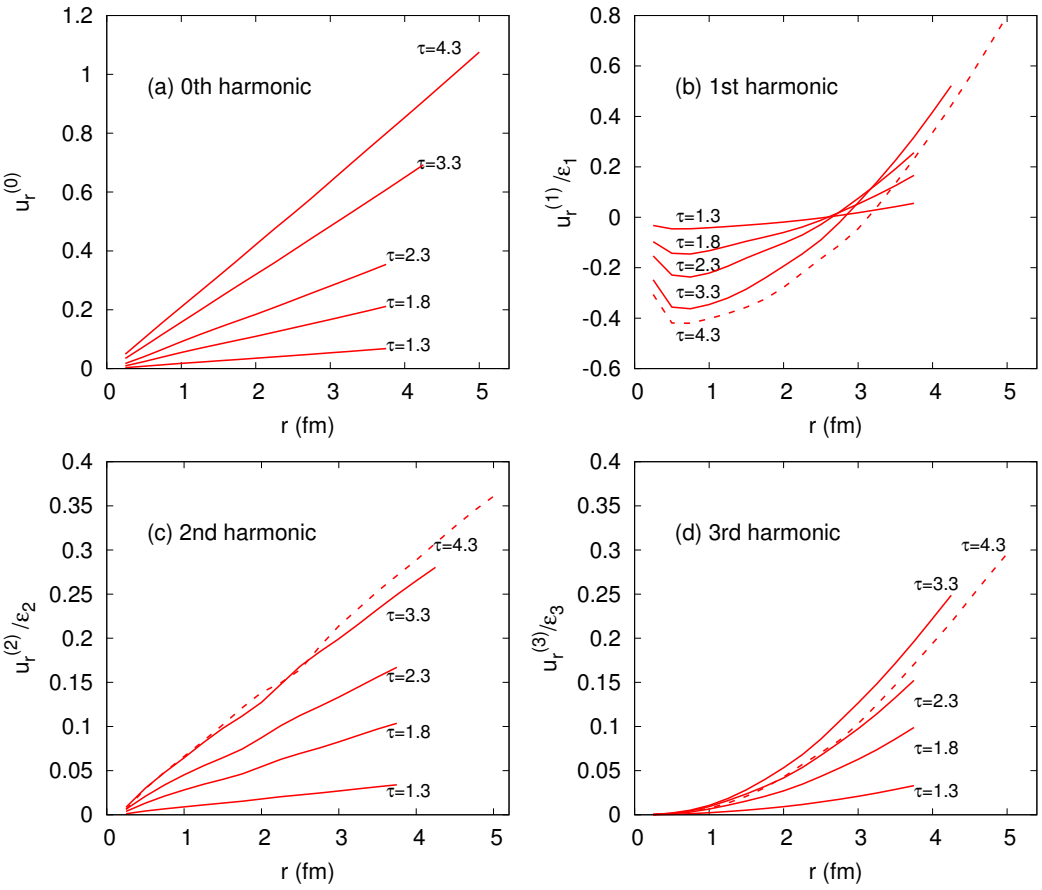

Figure 3.2: Flow profile evolution

(a) The zeroth harmonic of the flow profile (see Eq. 3.9) for the radially symmetric Gaussian adopted in this work. The root mean square radius of the Gaussian is adjusted to reproduce an impact parameter of 7.6 fm. (b) The first harmonic of the flow profile for a distribution with a net dipole asymmetry. (c) The second harmonic of the flow profile for an elliptic perturbation. (d) The third harmonic of the flow profile for a triangular perturbation

If $\Phi(r,\phi)$ is an analytic function of x and y, then $\Phi^{(2)}$ must be quadratic for small r. Consequently, the gradient of this function $u^{(2)}(r)$ will rise linearly at small r. Similarly, the triangular deformation $\Phi^{(3)}(r)$ should be cubic at small r and the flow profile $u^{(3)}(r)$ should be quadratic. These features are borne out by our numerical work as exhibited in Fig. 3.2. The first harmonic is negative at small r followed by a quadratically rising profile at larger r. This structure can be qualitatively understood using momentum conservation as discussed in the previous section for the dipole asymmetry.

As seen from Fig. 3.2, the dipole and triangular flows are biased toward the edge of the nucleus, which can be attributed to the harmonic response to the anisotropy proportional to $\{r^n\}$. Due to this bias, the more sensitivity of higher order harmonic flow is expected to the freeze-out prescription.

3.1.2 Linear flow response coefficients

To have a fully determined prediction for the final state observables,in addition to the knowledge of the initial state from Monte Carlo simulations, we require linear flow response coefficients w_n/ϵ_n. The linear response coefficients are a function of collision centrality, the properties of the medium, and the transverse momentum of the observed particles. These dependencies must reproduce the analogous dependencies observed in the data. In this work, ideal and viscous hydrodynamic calculations are used with a lattice EoS. The freeze-out is taken with respect to a constant freeze-out temperature $T_{fo} = 150$ MeV.

p_T dependence

In Fig. 3.3, the transverse momentum dependence of linear flow response coefficients of harmonic order $n \leq 5$ are obtained from ideal hydrodynamic calculations for a RHIC Au-Au collision event with $b = 7.45$ fm.

As was explained in [96] based on a saddle point approximation for the freeze-out integral for ideal hydrodynamics, and implied from flow profile in the previous section, in the regime of large enough p_T, the p_T dependence of the generated flow is, $v_n(p_T) \propto p_T$ [3]. For the small p_T range, in a very similar manner the analysis leads to the result $v_n(p_T) \propto (p_T)^n$. These two extreme p_T regions are apparent in Fig. 3.3, and especially we should note the transition region from $(p_T)^n$ to the linear p_T dependence of these flows.

Since dipole flow v_1 is constrained by the conservation of transverse momentum, as discussed in Section 2.1, correspondingly the p_T dependence of

[3]The original analysis was proposed for elliptic flow v_2, but the conclusion can be naturally extended to any harmonic order.

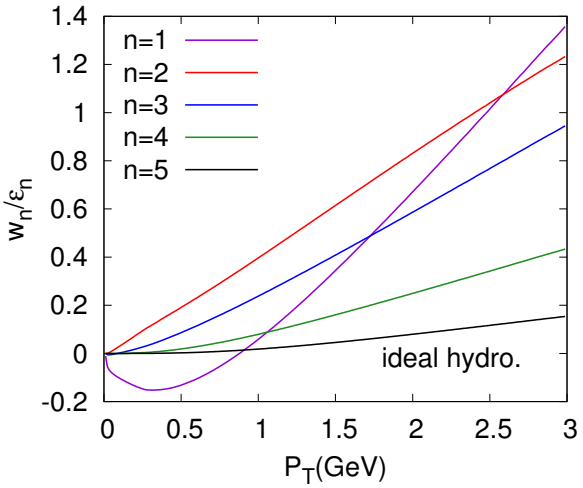

Figure 3.3: p_T dependence of linear response coefficients.
$w_n/\epsilon_n(p_T)$ from ideal hydrodynamic simulations for RHIC Au-Au collisions, with the impact parameter $b = 7.45$ fm.

linear flow response coefficient w_1/ϵ_1 is not monotonic, and w_1/ϵ_1 crosses zero at $p_T = p_T^0$. Based on the conservation of transverse momentum, and an approximated particle spectrum, it can be argued that the crossing point is related to the radial flow of the expanding medium, *i. e.* $p_T^0 \sim \langle p_T^2 \rangle / \langle p_T \rangle$.

When viscous effect of hydrodynamics is considered, the high p_T regime linear dependence is broken as a result of the viscous corrections to the freeze-out integral. We leave the detailed discussion on this issue in Chapter 5.

Centrality dependence

In Fig. 3.4, the integrated results of w_n/ϵ_n,

$$\frac{w_n}{\epsilon_n}(b) = \int dp_T \frac{dN}{dp_T} v_n(p_T, b)$$

are plotted as a function of impact parameter b, from ideal and viscous hydrodynamic calculations. Note since the integral is dominated by the low p_T region, linear dipole flow response coefficient is negative. From very central to very peripheral collisions, the primary change of the expanding system is the decrease of the fireball life-time, which is the direct result of the decreasing entropy density as well as the system size. Therefore, towards a larger collision centrality a smaller radial flow is excepted to be developed, as well as the linear flow response. As is confirmed in Fig. 3.4 from both ideal and viscous

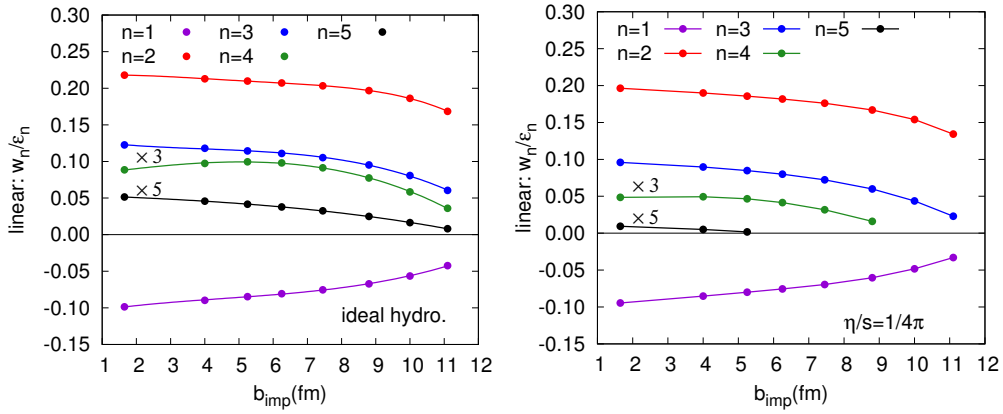

Figure 3.4: Centrality dependence of linear response coefficients w_n/ϵ_n as a function of impact parameter, from the ideal and viscous hydrodynamic simulations for RHIC Au-Au collisions. To make the response coefficients visible, a factor of 3 and 5 are multiplied for $w_4/\mathcal{C}_4$ and $w_5/\mathcal{C}_5$ respectively.

hydrodynamics, the magnitude of the flow response coefficients has a slight monotonic decrease when b increases.

Another salient feature we note in Fig. 3.4 is the systematic decrease of these linear response coefficients with the growth of harmonic order, which can also be seen in the differential spectrum in Fig. 3.3. In fact, to make $w_4/\mathcal{C}_4$ and $w_5/\mathcal{C}_5$ visible, a factor of 3 and 5 have been multiplied respectively. Viscous effect which damps these linear flow response coefficients tends to substantiate the decrease, in particular $w_4/\mathcal{C}_4$ and $w_5/\mathcal{C}_5$ become negative at larger centrality in the viscous hydrodynamics results. The viscous $w_4/\mathcal{C}_4$ and $w_5/\mathcal{C}_5$ curves in Fig. 3.4 stop abruptly as a function of centrality, since we have truncated the curves when response falls below zero to avoid physical inconsistency.

Dependence on shear viscosity

The linear flow response is damped by the viscous effects of medium, as indicated in viscous hydrodynamic calculations. Intuitively, the viscous damping of the flow response can be understandable as follows. The sensitivity of a medium response to the geometric deformation depends on the mean free path $\lambda_{\rm mfp}$, which can be roughly estimated as $\lambda_{\rm mfp} \propto \eta/s$. Therefore for a medium system with larger shear viscosity, the expected sensitivity of the medium response is reduced. In addition, a characteristic length λ^n_{ch} of harmonic order n can be assigned to the anisotropy ϵ_n, quantifying the length scale of the

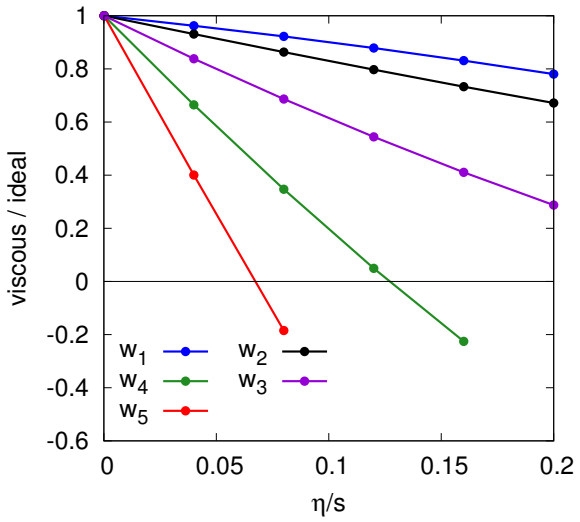

Figure 3.5: Linear flow response dependence on η/s
Linear response coefficients w_n as a function of viscosity relative to the ideal response.

spatial azimuthal deformation. Geometrically λ^n_{ch} decreases with respect to the growth of n for a system with finite size. As a result, qualitatively describing the ability of medium response to the initial state azimuthal deformation as the ratio $\lambda^n_{\rm ch}/\lambda_{\rm mfp}$, it is not difficult to expect higher order harmonic flow suffering more from viscous damping, as seen in Fig. 3.5.

For a pure conformal theory, hydrodynamics with analytical solution has been developed by Gubser and Yarom [97]. It was realized in their analysis that a coordinate transformation with respect to conformal symmetry can be applied to the Bjoken boost invariant 2+1 dimensional hydrodynamics, so that the manifold of the hydrodynamics is simplified with a $SO(1,1) \times \mathcal{Z}_2 \times SO(3)$ symmetry. Each linearized perturbation labeled by (n,m)-th cumulant is damped by a factor $\sim \exp(-\Gamma_{n,m}\, t_{\rm f})$ relative to ideal hydrodynamics, where $t_{\rm f}$ is an estimate for the duration of the event. Gubser and Yarom's solution shows that the damping coefficients $\Gamma_{n,m}$ scale as

$$\Gamma_{n,m}\, t_{\rm f} \sim \frac{\ell_{\rm mfp}}{L}\left(\frac{n-m}{2}+m\right)^2 , \tag{3.11}$$

for a conformal equation of state and a particular background flow [97]. Our numerical work (Fig. 3.5) is not limited to the conformal equation of state or the particular background flow of Ref. [97], and shows that this scaling is

reasonably generic [73, 88]. Specifically, the formal estimate given in Eq. (3.11) implies a definite pattern among the viscous corrections to v_n:

$$
\begin{aligned}
-\frac{\Delta w_1}{w_1^{\rm id}} \simeq -\frac{\Delta w_2}{w_2^{\rm id}} \propto 4\,\frac{\eta}{s}\,, \qquad -\frac{\Delta w_3}{w_3^{\rm id}} \propto 9\,\frac{\eta}{s}\,, \\
-\frac{\Delta w_4}{w_4^{\rm id}} \propto 16\,\frac{\eta}{s}\,, \qquad -\frac{\Delta w_5}{w_5^{\rm id}} \propto 25\,\frac{\eta}{s}\,.
\end{aligned} \tag{3.12}
$$

where $\Delta w = w^{\rm viscous} - w^{\rm ideal}$, and $w^{\rm id}$ is the ideal hydro response coefficient. Note, in particular that the viscous corrections v_1 and v_2 are similar since v_1 and v_2 respond to the dipole asymmetry, $W_{3,1}$, and the ellipticity, $W_{2,2}$, respectively [88]. Since the slopes of the $v_1 : v_2 : v_3 : v_4 : v_5$ curves in Fig. 3.5 have approximately the expected ratios $4 : 4 : 9 : 16 : 25$, our numerical work qualitatively confirms this pattern of viscous corrections.

When viscous effects become remarkable in hydrodynamic simulations, *e. g.* the calculation of $w_4/\mathcal{C}_4$ and $w_5/\mathcal{C}_5$ in Fig. 3.4 at very peripheral collision bins from viscous hydrodynamics, and in Fig. 3.5 with large enough η/s, a negative linear flow response is achieved. However, except the negative result of dipole flow which is natural, the flow response of medium should always be non-negative. The obtained inconsistency reflects the incompleteness of our viscous hydrodynamic simulations, which we will detail in Chapter 5.

3.1.3 Application of linear flow response

Based on the simple assumption of linear flow response, Eq. (3.2) gives rise to a direct one-to-one mapping between initial state and final state. For example, it is straightforward to estimate the magnitude of the predicted harmonic flow as linearly proportional to ϵ_n, and the angles are identified, $\Psi_n = \Phi_n$. In this spirit, considering only linear flow generation in hydrodynamics, the predicted event plane correlations are identical to their corresponding initial state participant plane correlations, see in Fig. 2.10 and Fig. 2.11, which case we refer as the 'linear limit' in our work.

As a result of linear flow response assumption, we obtain the particle spectrum from one heavy-ion collision,

$$
\frac{dN}{d\phi_p} = \frac{N}{2\pi}\left[1 + \sum_{n=1}^{\infty} e^{in\phi_p}\left(\frac{w_n}{\epsilon_n}\epsilon_n e^{-in\Phi_n}\right) + c.c.\right]\,, \tag{3.13}
$$

from which, regarding the realistic experiment measurements with specified event average process, the multi-particle correlation functions can be formu-

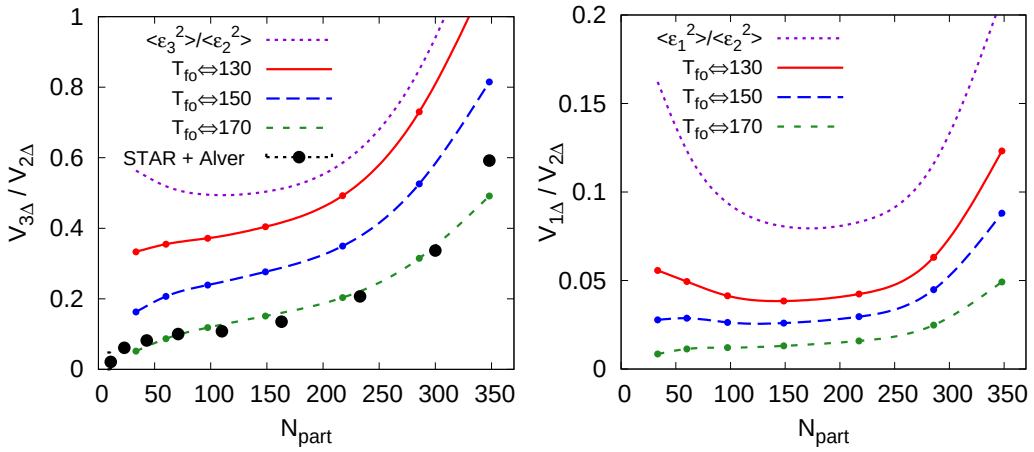

Figure 3.6: $V_{3\Delta}/V_{2\Delta}$ and $V_{1\Delta}/V_{2\Delta}$ as a function of N_{part}.
Fourier components of the two particle correlation function as a function of $N_{\rm part}$ relative to the quadrupole component. (a) The triangularity component compared to the Alver Roland fit [54] of STAR inclusive two particle correlation functions [98]. (b) The dipole compoent relative to the quadrupole component.

lated. For example, the two-particle correlation function is

$$\left\langle\!\!\left\langle \frac{dN^a dN^b}{d\phi^a d\phi^b} \right\rangle\!\!\right\rangle \simeq \frac{N^a N^b}{(2\pi)^2}\Bigg[1 + \sum_n \left(\frac{w_n^a w_n^b}{\epsilon_n^2}\right) \langle\!\langle \epsilon_n^2 \rangle\!\rangle e^{in(\phi_a-\phi_b)} + \frac{w_2^a}{\epsilon_2}\langle\!\langle \epsilon_2 \rangle\!\rangle e^{i(2\phi_a-2\Phi_2)} + \frac{w_2^a w_2^b}{\epsilon_2^2}\langle\!\langle \epsilon_2^2 \rangle\!\rangle e^{i(2\phi_a+2\phi_b-4\Phi_2)} + \frac{w_1^a w_1^b}{\epsilon_1^2}\langle\!\langle \epsilon_1^2 e^{i2(\Phi_1-\Phi_2)} \rangle\!\rangle e^{i(\phi_a+\phi_b-2\Phi_2)} + \frac{w_1^a w_3^b}{\epsilon_1\epsilon_3}\langle\!\langle \epsilon_1\epsilon_3 e^{i(\Phi_1-3\Phi_3+2\Phi_2)} \rangle\!\rangle e^{i(\phi_a-3\phi_b+2\Phi_2)} + \ldots + a \leftrightarrow b\Bigg] + c.c.\,, \tag{3.14}$$

where a and b label the particle type, and the symmetrization of a and b is applied to all terms that is not symmetric with respect to the exchange of indices (a, b). The first line in Eq. (3.14) represents the contribution from diagonal correlations, which defines the generally observed harmonic flow $v_n\{2\} = (w_n/\epsilon_n) \times \epsilon_n\{2\}$, as well as the Fourier component in a two-particle spectrum $V_{n\Delta} = (v_n\{2\})^2$. In Fig. 3.6 the linear flow response from ideal hydrodynamics

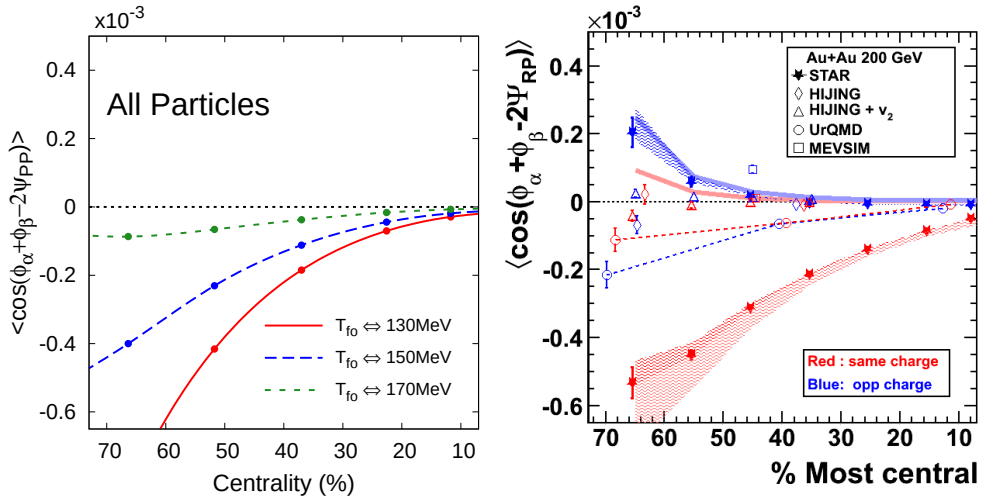

Figure 3.7: $\langle\langle\cos(\phi_a + \phi_b - 2\Psi_R)\rangle\rangle$ from hydrodynamic simulation. $\langle\langle\cos(\phi_a + \phi_b - 2\Psi_R)\rangle\rangle$ is calculated based on linear flow response formalism. The measured results are charged particle correlation from RHIC STAR collaboration[99, 100].

makes a definite prediction for the different $V_{n\Delta}$. The elliptic flow is too large in the ideal massless gas model considered here. We will therefore simply plot the ratios of the different Fourier components as was done in the Alver and Roland paper. Using just the linear response coefficients, and the Glauber estimates for $\langle\langle\epsilon_3^2\rangle\rangle/\langle\langle\epsilon_2^2\rangle\rangle$, Fig. 3.6(a) compares the strength of the triangular component to the quadrapole component.

The ideal hydrodynamic prediction (with a massless ideal gas EoS) is generally too large and fairly sensitive to the freeze-out temperature. This sensitivity reflects the fact that the triangular flow develops further toward the edge of the nucleus. Fig. 3.6(b) compares the dipole component to the quadrapole component. The dipole component is a factor of 8 smaller than the quadrapole component. This is a reflection of the fact that ϵ_1 is small, and the fact that $w_1(p_T)/\epsilon_1$ is positive and negative. The dipolar flow is also sensitive to the details of the freeze-out.

All of the survived contributions of the non-diagonal correlations from the event average are rooted in the initial state almond shape geometry, *e. g.* $\langle\langle\epsilon_2\rangle\rangle$, or correlations *e. g.* $\langle\langle\cos 2(\Phi_1 - \Phi_2)\rangle\rangle$. In Eq. (3.14), only a few terms of importance and relevant to the present discussions are displayed. However it should be emphasized that there are in principle infinite number of non-trivial observables implied in the ellipsis.

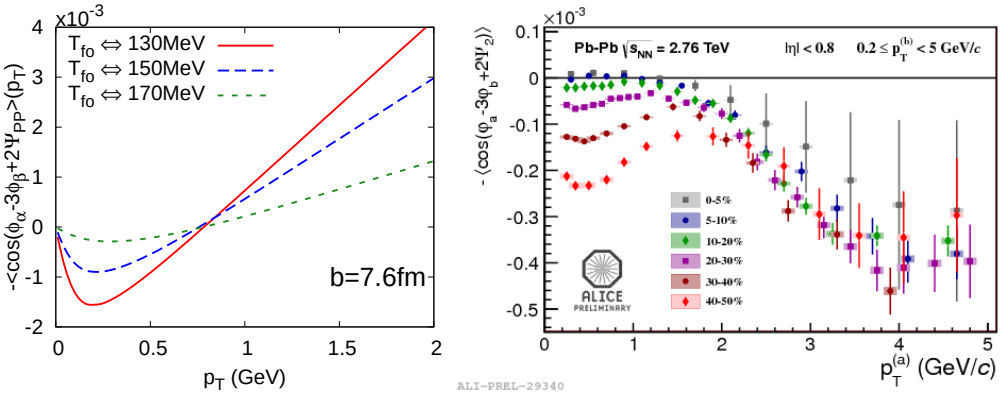

Figure 3.8: Differential $\langle\cos(\phi_a - 3\phi_b + 2\Psi_R)\rangle$ of mid-central collisions. A hydrodynamic prediction for the expectation value $\langle\cos(\phi_a - 3\phi_b + 2\Psi_R)\rangle$ and the corresponding measurement from ALICE collaboration[82].

Based on Eq. (3.14), the predictions can be made for many of the observed two-particle correlations, given the information from Monte Carlo simulation of fluctuating initial state and the linear flow response efficients from hydrodynamics. For example, the measured $\langle\cos(\phi_a + \phi_b - 2\Psi_R)\rangle$ [4] is determined by the initial state plane correlation and the linear dipole flow response w_1/ϵ_1,

$$\langle\cos(\phi_a + \phi_b - 2\Psi_R)\rangle = 2\left(\frac{w_1^a}{\epsilon_1}\right)\left(\frac{w_1^b}{\epsilon_1}\right)\langle\langle\epsilon_1^2\cos 2(\Phi_1 - \Phi_2)\rangle\rangle\,. \tag{3.15}$$

As discussed in the previous chapter, the preference of dipole angle pointing out-of reaction leads to a centrality dependent correlation between Φ_1 and Φ_2. Reflected in the expectation value of $\langle\cos(\phi_a + \phi_b - 2\Psi_R)\rangle$, as a function of centrality the prediction from ideal hydrodynamics is shown in the left panel in Fig. 3.7. Lower freeze-out temperature means a longer period of medium response, so that a larger magnitude of response value w_1/ϵ_1. In order to investigate the possibility of local parity violation in the initial stage of heavy-ion collisions, as proposed in [101] as the chiral magnetic effect, the expectation value $\langle\cos(\phi_a+\phi_b-2\Psi_R)\rangle$, and in particular the imbalance between the detailed charge components (same and opposite) was measured by STAR collaboration[99, 100]. Although was carried out for a conformal equation of state, our calculation predict the same order of magnitude, providing a background neutral correlation.

[4]The single angle brackets $\langle\ldots\rangle$ in this work is often used to notate an average with respect to the particle spectrum.

Comparing to the STAR measurement, $\langle\cos(\phi_a + \phi_b - 2\Psi_R)\rangle$ was an insightful beginning of analyzing initial state geometric information from final state particle spectrum. Focusing on the 6-th term in the bracket in Eq. (3.14), in a very similar manner, the expectation value of $\langle\cos(\phi_a - 3\phi_b + 2\Psi_R)\rangle$ is connected to the initial state correlation between Φ_1, Φ_2 and Φ_3,

$$\langle\cos(\phi_a - 3\phi_b + 2\Psi_R)\rangle = \frac{w_1^a w_3^b}{\epsilon_1\epsilon_3}\langle\langle\epsilon_1\epsilon_3\cos(\Phi_1 + 2\Phi_2 - 3\Phi_3)\rangle\rangle\,. \tag{3.16}$$

Since the combined contribution in the r.h.s. of Eq. (3.8) is of the similar order of magnitude, the expected final state correlation should also be measurable in experiment. Taking the integrated flow response for the b labeled particles, and taking a to label particles of p_T, we have the prediction of a differential correlation in the left of Fig. 3.8. As the application of Eq. (3.16), it is not difficult to realize that the differential structure of the predicted correlation is controlled by the p_T dependence of dipole flow v_1, and the magnitude partly relies on initial plane correlation $\langle\langle\cos(\Phi_1 + 2\Phi_2 - 3\Phi_3)\rangle\rangle$. Indeed, for the prediction of the mid-central collision, the correlation curve crosses zero from low p_T region to high p_T region at the same p_T value of dipole flow v_1.

Nonetheless, in spite of the comparable pattern of the correlation at low p_T from ALICE experiment, in the right panel in Fig. 3.8 a significantly different p_T dependence is observed. This inconsistency, together with the general misprediction of the 'linear limit' for the event-plane correlations, implies the unavoidable contribution beyond linear order of flow response.

3.2 Nonlinear flow response

As has been noticed in the application of linear flow response in Section 3.2, the simple factorization of the generated harmonic flow as the product of initial state eccentricity and linear flow response is problematic, in reproducing some of the observables in experiment, in particular when higher order ($n \geq 4$) harmonics is involved.

In order to go beyond the leading order flow generation from the linear response assumption, we extend the formulation Eq. (3.2) with higher order nonlinearities. For the generation of harmonic flow v_n, due to the rotational symmetry and reflection symmetry, the effective nonlinear contributions are constrained. Let us take the pentagonal flow v_5 as an example. In additional to linear response to $\mathcal{C}_5$, there exists the allowed nonlinear contribution from

the response to the coupling of ellipticity ϵ_2 and triangularity ϵ_3, *i. e.*

$$v_5 e^{-i5\Psi_5} = \frac{w_5}{\mathcal{C}_5}\left(\mathcal{C}_5 e^{-i5\Phi_5}\right) + \frac{w_{5(23)}}{\epsilon_2\epsilon_3}\left(\epsilon_2\epsilon_3 e^{-i(2\Phi_2+3\Phi_3)}\right) . \tag{3.17}$$

It is easy to check the rotational symmetry of the above expression, since the combination $2\Phi_2 + 3\Phi_3$ is also periodic in $2\pi/5$. As a result, to form this type of nonlinear mode mixing we expect an ellipticity and a triangularity simultaneously in the initial state. With respect to the initial deformation from the combined effect of $\epsilon_2\epsilon_3$, we defined the flow response coefficient as $w_{5(23)}/(\epsilon_2\epsilon_3)$. Besides w which notates the flow response in analogous to the linear flow response, the sub-indices demonstrate the formation of a 5-th order flow from the nonlinear coupling of the second and third order anisotropies. Also, it should be noticed that the nonlinear flow response coefficient $w_{5(23)}/(\epsilon_2\epsilon_3)$ roughly scales as $\sim (w_2/\epsilon_2) \times (w_3/\epsilon_3)$.

A generalization of this analysis leads to the description of flow generation from nonlinear mode mixing of any harmonic order. For example, considering nonlinear flow response to $\epsilon_2\epsilon_3$ and ϵ_2^2, we have of quadratic coupling order for dipole flow,

$$v_1 e^{-i\Psi_1} = \frac{w_1}{\epsilon_1}\left(\epsilon_1 e^{-i\Phi_1}\right) + \frac{w_{1(23)}}{\epsilon_2\epsilon_3}\left(\epsilon_2\epsilon_3 e^{-i(3\Phi_3-2\Phi_2)}\right) , \tag{3.18}$$

and quadrapole flow v_4

$$v_4 e^{-i4\Psi_4} = \frac{w_4}{\mathcal{C}_4}\left(\epsilon_4 e^{-i\Phi_4}\right) + \frac{w_{4(22)}}{\epsilon_2^2}\left(\epsilon_2^2 e^{-i4\Phi_2}\right) . \tag{3.19}$$

In principle to completely capture the flow generations, in the formulations Eq. (3.17), (3.18) and (3.19) we should have infinite number of nonlinear terms that satisfying symmetry constraints. For instance, there exists a cubic order mode mixing for the quadrapole flow $w_{4(112)}$ that responses to $\epsilon_1^2\epsilon_2$. However, since higher order nonlinear couplings decrease dramatically, we expect the flow generation to be dominated by the lowest order anisotropies and their mixing. In Table 3.1, the nonlinear terms contributing to the flow generation included in this work are listed.

In this section, we focus on the medium response to ϵ_2^2 and $\epsilon_2\epsilon_3$, from which the nonlinear flow generation of $w_{4(22)}$, $w_{5(23)}$ and $w_{1(23)}$ are analyzed. In our single-shot hydrodynamic simulations, to obtain $w_{4(22)}$ it is sufficient to deform the initial Gaussian background with only ellipticity $\epsilon_2 = 0.05$. However for $w_{5(23)}$ and $w_{1(23)}$ we have a more complicated initial profile with [5] $\epsilon_2 = \epsilon_3 = 0.05$. In analogous to the calculation of linear response coeffi-

[5]From time to time, for the specific problem we are considering, ϵ_2 of larger value is

Table 3.1: Nonlinear terms considered in this work

v_1	$w_{1(23)}/(\epsilon_2\epsilon_3)$	...	...	...
v_3	$w_{3(25)}/(\epsilon_2\mathcal{C}_5)$	...	...	...
v_4	$w_{4(22)}/(\epsilon_2^2)$	$w_{4(13)}/(\epsilon_1\epsilon_3)$	...	...
v_5	$w_{5(23)}/(\epsilon_2\epsilon_3)$	...	...	...
v_6	$w_{6(24)}/(\epsilon_2\mathcal{C}_4)$	$w_{6(33)}/(\epsilon_3^2)$	$w_{6(222)}/(\epsilon_2^3)$	...

cients, rescaled by the output value of eccentricities $\epsilon_n^{\text{output}}$, v_4, v_5 and v_1 from the corresponding hydrodynamic calculations give rise to the nonlinear response coefficients $w_{4(22)}/\epsilon_2^2$, $w_{5(23)}/(\epsilon_2\epsilon_3)$ and $w_{1(23)}/(\epsilon_2\epsilon_3)$. In particular, for the calculation of $w_{5(23)}/(\epsilon_2\epsilon_3)$ (and $w_{1(23)}/(\epsilon_2\epsilon_3)$), because two different types of deformations are simultaneously introduced in the initial state with the corresponding participant angles Φ_2 and Φ_3, there is an extra factor expected in the denominator,

$$\frac{w_{5(23)}}{\epsilon_2\epsilon_3} = \frac{v_5^c}{\epsilon_2^{\text{output}}\epsilon_3^{\text{output}}\cos(2\Phi_2+3\Phi_3)}\,, \tag{3.20}$$

where v_5^c is the x-component of the obtained flow v_5. For this case, the relative angle $\Phi_3-\Phi_2$ breaks the rotational symmetry, resulting in a potential $\Phi_3-\Phi_2$ dependence of the nonlinear flow response coefficients.

For these particular examples, in parallel to the discussions in Section 3.1.2, we investigate the dependence of transverse momentum p_T, centrality and viscous effect η/s of nonlinear flow response coefficients. Given the properties of these coefficients, predictions on an event-by-event basis can be made.

3.2.1 Nonlinear flow response coefficients

When multiple eccentricities are considered in the initial state simultaneously, *e. g.* ϵ_2 and ϵ_3 for nonlinear v_5 generation, the dependence on the relative angles needs to be examined. In Fig. 3.9, the nonlinear flow response coefficients $w_{5(23)/(\epsilon_2\epsilon_3)}$ and $w_{1(23)}/(\epsilon_2\epsilon_3)$ from one very peripheral collision event are plotted as a function of the initial relative angle $\Phi_3-\Phi_2$. The ellipticity ϵ_2 and Φ_2 in these calculations are taken naturally from the asymmetric Gaussian background. For this extreme example, although the geometry of rotational

taken from an asymmetric Gaussian background. For realistic hydrodynamic simulations, taking ϵ_2 to be a small value or generically from the Gaussian does not alter the conclusion of the obtained nonlinear flow response coefficients.

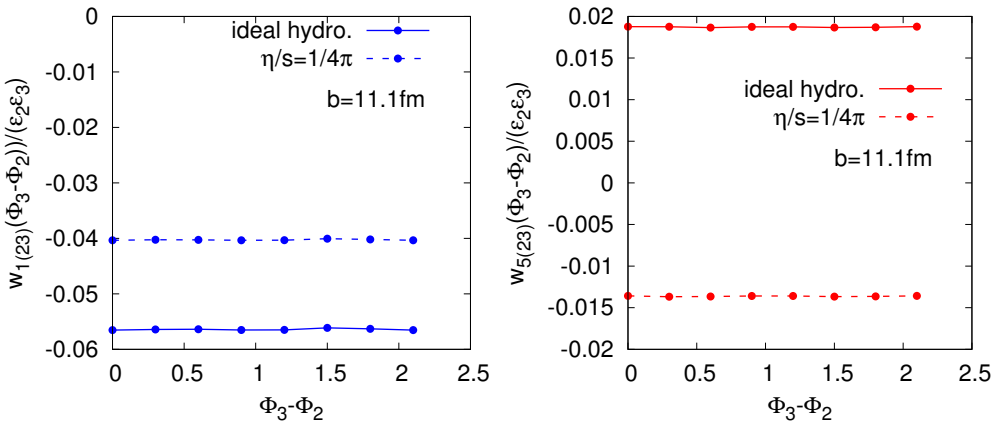

Figure 3.9: Angle dependence of nonlinear flow response coefficients. Nonlinear flow response coefficients $w_{5(23)/(\epsilon_2\epsilon_3)}$ and $w_{1(23)}/(\epsilon_2\epsilon_3)$ are calculated for a very peripheral collision event with impact paramter $b = 11.1$ fm for RHIC Au-Au, with ideal and viscous ($\eta/s = 1/4\pi$) hydrodynamics, as a function of the relative angle $\Phi_3 - \Phi_2$.

symmetry is broken apparently, negligible dependence of the relative angles of the obtained nonlinear flow response coefficients are found. As a result, in the following calculations for simplicity we can keep the relative angle $\Phi_3 - \Phi_2$ zero.

p_T dependence

The transverse momentum dependence of the nonlinear flow response is illustrated in Fig. 3.10, for $n = 4$ and $n = 5$ for one mid-central collision event of RHIC Au-Au from ideal hydrodynamic calculation. At low p_T region, nonlinear flow response coefficients present very similar p_T dependence, to the corresponding linear flow response $w_4/\mathcal{C}_4$ and $w_5/\mathcal{C}_5$. However, dramatically distinguished from the behavior of $\propto p_T$ of linear flow response coefficient in large p_T region, the obtained nonlinear flow response coefficients of the quadratic order rise as $\propto p_T^2$. This p_T^2 dependence of nonlinear flow response coefficients can be generally found in all of the quadratic couplings of flow generations, which, together with the linear p_T dependence of linear flow response coefficient, can be interpreted quantitatively by analyzing the high p_T fraction of the freeze-out integral. Viscous effects are not considered in these calculations, which we leave to the discussion in Chapter 5.

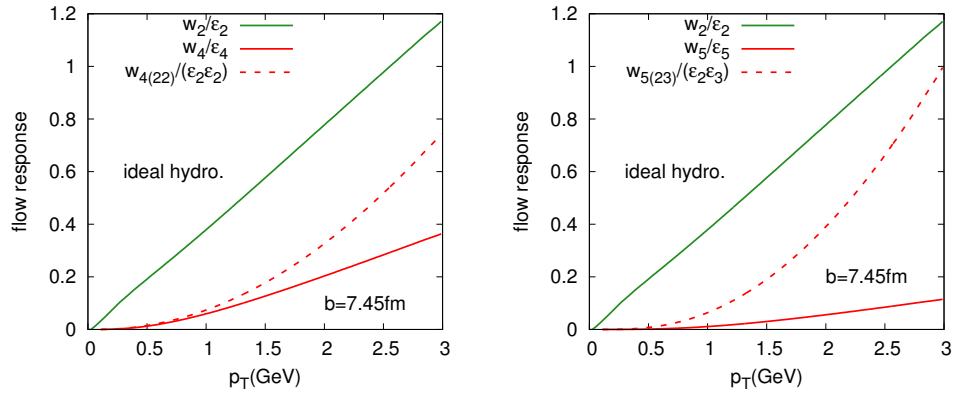

Figure 3.10: p_T dependence of nonlinear flow response coefficients. Nonlinear flow response coefficients $w_{5(23)/(\epsilon_2\epsilon_3)}(p_T)$ and $w_{4(22)}/(\epsilon_2\epsilon_2)(p_T)$ from ideal hydrodynamic simulations for RHIC Au-Au collisions with $b = 7.45$ fm. p_T dependent linear flow response coefficients w_2/ϵ_2, $w_4/\mathcal{C}_4$ and $w_5/\mathcal{C}_5$ are plotted as well for comparisons.

Centrality dependence

In analogous to the analysis for the centrality dependence of linear flow response, when the system size decreases with the increases of centrality, insufficient flow development during medium expansion also leads to a reduction of nonlinear flow response. As been confirmed in Fig. 3.11, a monotonic drop of the nonlinear flow response coefficients with respect to the growth of centrality is seen, in both of the results from ideal and viscous hydrodynamics.

Comparing to the linear flow response of dipole flow, nonlinear response to initial $\epsilon_2\epsilon_3$ gives rise to a slightly smaller value of response coefficient $w_{1(23)}/(\epsilon_2\epsilon_3)$. However, the magnitudes of nonlinear flow response coefficients $w_{4(22)}/\epsilon_2^2$ and $w_{5(23)}/(\epsilon_2\epsilon_3)$ are significantly larger than the coefficients $w_4/\mathcal{C}_4$ and $w_5/\mathcal{C}_5$ in Fig. 3.4. Especially from viscous hydrodynamic calculations this effect is even stronger. Note since the obtained coefficients $w_{4(22)}/\epsilon_2^2$ and $w_{5(23)}/(\epsilon_2\epsilon_3)$ for peripheral collisions from viscous hydrodynamics are oversuppressed, a similar cut is applied as what has been done for the linear response coefficients.

Dependence on shear viscosity

When the quantitative analysis Eq. (3.11) of viscous damping is applied to nonlinear flow response, considering the nonlinear flow generation as the product

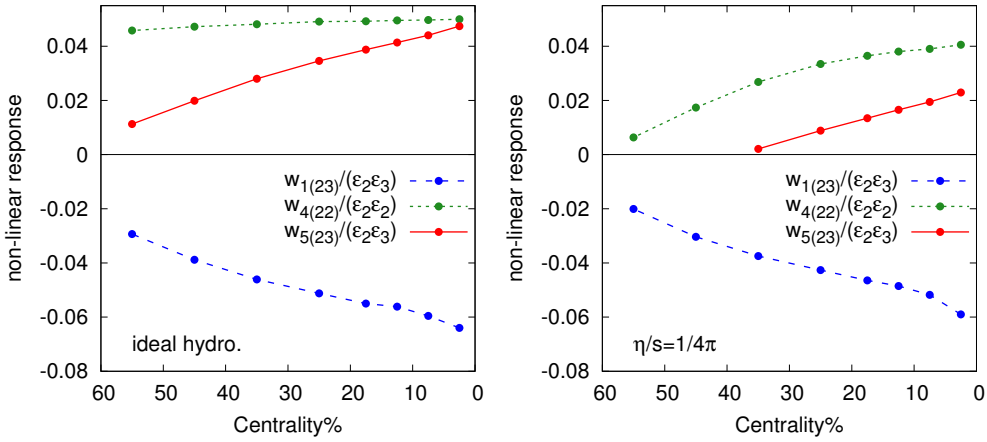

Figure 3.11: Centrality dependence of nonlinear flow response coefficients Nonlinear flow response coefficients, $w_{4(22)}/\epsilon_2^2$, $w_{5(23)}/(\epsilon_2\epsilon_3)$ and $w_{1(23)}/(\epsilon_2\epsilon_3)$ are plotted as a function of centrality. The results are obtained from ideal and viscous hydrodynamic simulations for RHIC Au-Au collisions.

of linear flow response, the damping rate of nonlinear flow response coefficients can be estimated. For example, $w_{5(23)}$ is effectively the product of w_2 and w_3. As a result, we expect the viscous damping of $w_{5(23)}/(\epsilon_2\epsilon_3)$ to be described as $\sim e^{-\Gamma_{2,2}\tau_f}e^{-\Gamma_{3,3}\tau_f}$, so that the damping rate

$$\Gamma_{5(23)}\tau_f = (\Gamma_{2,2}+\Gamma_{3,3})\tau_f \sim -\frac{\Delta w_{5(23)}}{w^{\rm ideal}_{5(23)}} \propto (4+9)\frac{\eta}{s}\,. \tag{3.21}$$

Eq. (3.21), and the generalized formulas of this type for the nonlinear flow response coefficients, quantifies the viscous damping effect. In particular, the inequality $(a+b)^2 > a^2+b^2$ and the decomposition of the nonlinear flow viscous damping rate have an significant deduction: *The effect of viscous damping on the n-th order harmonic is weaker for the nonlinear flow response than its corresponding linear flow response.*

In Fig. 3.12 the damping rates of $w_{4(22)}/\epsilon_2^2$, $w_{5(23)}/(\epsilon_2\epsilon_3)$ and $w_{1(23)}/(\epsilon_2\epsilon_3)$ are plotted as a function of η/s, for a mid-central event of RHIC Au-Au collisions. Comparing to their corresponding linear flow response coefficients, the above analysis is found to be semi-quantitatively consistent, with the exception of $w_{1(23)}$. In addition to the correct prediction of the slopes of the curves by the equations like Eq. (3.21) , a relatively stronger viscous damping of linear flow response is obtained as expected. However, as a special case, the obtained viscous effect of $w_{1(23)}$ contradicts our reasoning, *e. g.* $\Gamma_{1(23)} > \Gamma_1$.

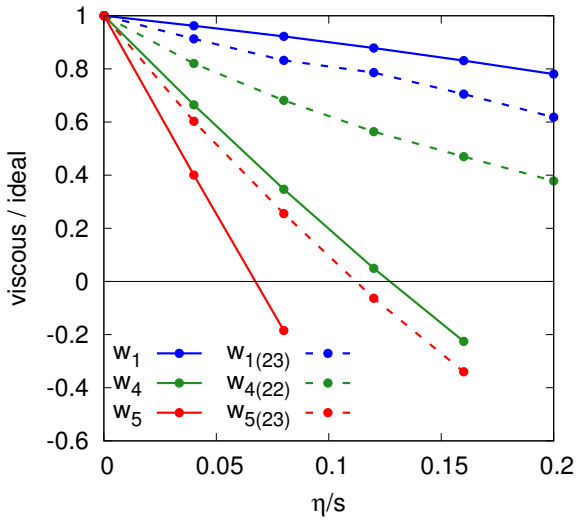

Figure 3.12: Nonlinear flow response dependence on η/s
Viscous damping rate of $w_{1(23)}$, $w_{4(22)}$ and $w_{5(23)}$ as a function of η/s. The corresponding linear flow response coefficients are plotted as well for comparisons.

The interpretation is possibly due to the extra constraint from the momentum conservation, which will have to be investigated in future studies.

In Fig. 3.12, for sufficiently large η/s the negative value of w_4, w_5 and $w_{5(23)}$ are spurious as a result of the inconsistency of viscous hydrodynamic calculations. A more systematic treatment of this issue will be discussed in Chapter 5.

3.2.2 Origins of the nonlinear flow generation

The nonlinear flow generation is confirmed from the simulations of ideal and viscous hydrodynamics, with a specified formulation the corresponding nonlinear flow response coefficients are extracted in the previous section. In this section, for the purpose of a better understanding of the flow generation mechanism, we give a tentative discussion on the origins of these nonlinear mode mixing. Taking into account the whole evolution of medium in the framework of hydrodynamic calculation, the mode mixing can exist in the fluctuating initial state, the medium expansion and the freeze-out.

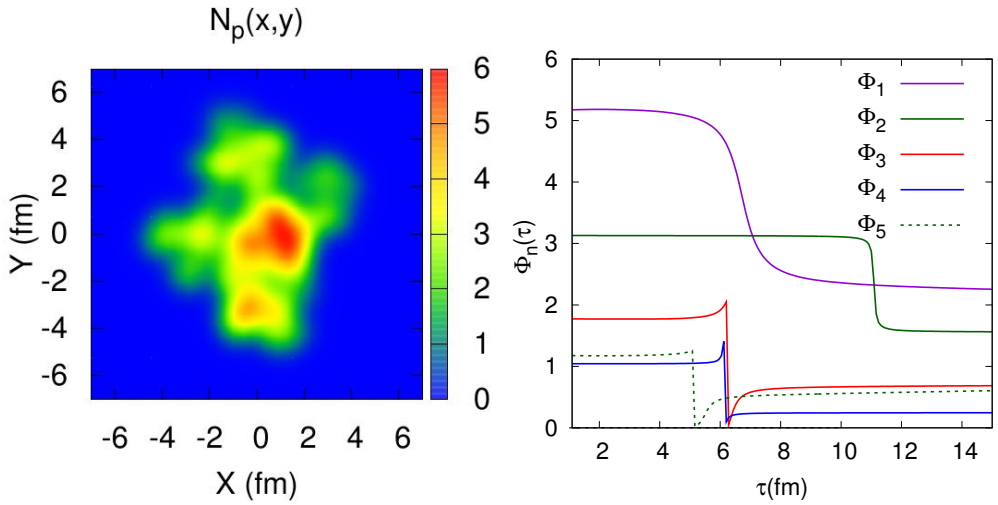

Figure 3.13: Participant plane angle time evolution
The evolution of the cumulant defined participant plane angle $\Phi_n(\tau)$, from ideal hydrodynamics for one selected event with initial state fluctuations. The angle Φ_n's change by the value π/n is associated with a natural flipping of the geometric shape.

Initial state

As detailed in Chapter 2, the initial state with fluctuations in our work is characterized by the cumulant expansion formalism. Comparing to the traditionally used momentum definition, in cumulant definition there are extra nonlinear terms coming from lower order anisotropies. For instance, in the definition of quadrapole anisotropy, the nonlinear part which is proportional to ϵ_2^2 is subtracted. This sort of subtraction ensures a essential feature of cumulant definition, that the interference between different cumulant orders is prevented, *i. e.* the omission of one term in the cumulant expansion series cannot be supplemented by the others. As a consequence, as long as cumulant expansion formalism is applied for the fluctuating initial state, and considering the medium response with respect to the cumulant defined eccentricities, initial nonlinear mode mixing can be ignored.

In medium expansion

The medium expansion is characterized by hydrodynamics, thereby the mode mixing during medium evolution can be in principle investigated based on the analysis of hydrodynamic theory, *e. g.* the Gubser-Yarom solution of conformal hydrodynamics. However, with respect to the realistic medium system

and flow generation in heavy-ion collisions, analytical description of nonlinear mode mixing in medium at present is not approachable. Alternatively, with numerical simulations of the system evolution, the mode mixing in medium can be examined.

In Fig. 3.13, selecting one particular event with initial state spatial fluctuations, we track the time evolution of the cumulant defined participant plane angle Φ_n. As a typical example on an event-by-event basis, the initial profile in the left figure in Fig. 3.13 is azimuthally deformed of all harmonic orders. Driven by this bumpy structure, the system expansion leads to a time evolving medium spatial distribution $\rho(\boldsymbol{x}, \tau)$, based on which the time evolving participant plane angle $\Phi_n(\tau)$ is calculated. As shown in the right panel of Fig. 3.13, despite the natural switch of the geometric shape of each harmonic order at a certain time, resulting in a dramatic change of $\Delta\Phi_n = \pi/n$, these angles develop independently on time. Note the non-analytical drop or rise in the change of Φ_3, Φ_4 and Φ_5 is due to an artificial effect in the numerical calculation. It is not difficult to deduce the corresponding time evolution in the momentum space, that the development of the generated momentum anisotropies does not depend on time either, indicating the absence of harmonic mode mixing during medium expansion. Since the spatial correlation, as well as the possible mode mixing, is diminished by dissipative effect of medium, the result in this example from ideal hydrodynamics strongly constraints in medium nonlinear flow coupling.

Mode mixing from freeze-out

The freeze-out process of hydrodynamic calculation transforms the space-time dependent medium distribution $f(x, \boldsymbol{p})$ into momentum anisotropy – the harmonic flow. Generally it is realized by the Cooper-Frye formula Eq. (1.33). Although the integral in Eq. (1.33) needs to be solved numerically for realistic calculations, for ideal hydrodynamics and in the large p_T region the saddle-point approximation can be applied for an analytical analysis, as proposed by Borghini and Ollitrault [96].

First let us recall the harmonic decomposition of the radial flow velocity in the transverse plane. The transverse flow vector is a function of the velocity azimuthal angle relative to the reaction plane, $\boldsymbol{u}_T = (u_r \cos\phi_u, u_r \sin\phi_u)$, in which the angle dependence of the radial flow u_r can be expressed as

$$u_r(r, \phi_u) \simeq u_r^0(r) + 2u_r^{(1)}(r)\cos(\phi_u - \Phi_1) + 2u_r^{(2)}(r)\cos 3(\phi_u - \Phi_2) + \ldots \quad (3.22)$$

Note the participant plane angles are introduced in the decomposition, since Φ_n are conserved during the medium expansion for the spatial geometry. Then

in the large p_T region, approximated by the classical Boltzmann distribution, the commonly considered constant temperature freeze-out process relies on the integrand [6],

$$e^{P\cdot u/T} = e^{-E_p u^\tau} e^{p_T/T u_r(r,\phi_u)\cos(\phi_p-\phi_u)}\,, \tag{3.23}$$

where E_p is the energy. Adopting the non-relativistic approximation $U^\tau \simeq 1$, and assuming the flow is approximately radial, so that $\phi_u \simeq \phi_r$,

$$\begin{aligned} e^{P\cdot u/T} \simeq & e^{-E_p/T} e^{p_T/T u_r^{(0)}\cos(\phi_p-\phi_r)} \left[1 + \left(\frac{2p_T}{T}\sum_{n=1} u_r^{(n)} \cos n(\phi_r - \Phi_n)\cos(\phi_p-\phi_r)\right)\right. \\ & \left. + \frac{1}{2}\left(\frac{2p_T}{T}\sum_{n=1} u_r^{(n)} \cos n(\phi_r - \Phi_n)\cos(\phi_p-\phi_r)\right)^2 + \dots\right]. \end{aligned} \tag{3.24}$$

In the Cooper-Frye formula, and for sufficiently large p_T/T, the ϕ_r integral under saddle point approximation is dominated around $\phi_r \simeq \phi_p$. As a result, in the harmonic decomposition of the particle spectrum, we arrive at the following form

$$\begin{aligned} \frac{dN}{d\phi_p} \sim 1 + & \left(\frac{2p_T}{T}\sum_{n=1} u_r^{(n)} \cos n(\phi_p - \Phi_n)\right) + \frac{1}{2}\left(\frac{2p_T}{T}\sum_{n=1} u_r^{(n)} \cos n(\phi_p - \Phi_n)\right)^2 \\ & + \dots \end{aligned} \tag{3.25}$$

Read from Eq. (3.25), the terms in the first bracket are easily recognized as the result of linear flow response $w_n(p_T) \sim u_r^{(n)} p_T/T$, which explains the linear dependence of p_T of linear flow response coefficients. When calculating v_n from the angle average of the spectrum, the integral $\int d\phi_p \cos n\phi_p dN/d\phi_p$ obtain extra contributions from the terms in the second bracket of Eq. (3.25), all of which grow quadratically with p_T. For example, for the quadrapole flow

$$v_4 = \frac{1}{2\pi}\int d\phi_p \cos 4\phi_p \frac{dN}{d\phi_p} \sim \frac{p_T}{T} u_r^{(4)} + \frac{1}{2}\left(\frac{p_T}{T} u_r^{(2)}\right)^2 + \dots\,, \tag{3.26}$$

despite the linearly generated $w_4 \sim p_T/T u_r^{(4)}$, the $(p_T)^2$ dependent term can be identified as the nonlinear flow response $w_{4(22)}$. The relation $w_{4(22)} = \frac{1}{2}w_2^2$ leads to the characteristic relation $v_4 = \frac{1}{2}v_2^2$ in Borghini-Ollitrault argument. Similar reasoning gives rise to the nonlinear flow generation $w_{5(23)} = w_2 w_3$, which leads to $v_5 = v_2 v_3$. Identifying these higher order terms as the nonlinear

[6] The rapidity dependence is neglected, since it does not affect the analysis here.

couplings in the formation of harmonic flow, Eq. (3.25) suggests the freeze-out process as the origin of the nonlinear mode mixing, and quantitative relations between these linear and nonlinear response are effectively described.

3.2.3 Application of the nonlinear flow generation

Nonlinear flow response formalism extends the applicability of single-shot hydrodynamics. With respect to the realistic heavy-ion collisions, quantifying the initial state fluctuations on an event-by-event basis with azimuthal anisotropies, the single-shot hydrodynamics framework with both linear and nonlinear flow response can make reliable predictions, for the observed harmonic flow and event plane correlations *etc.*. Furthermore, as discussed in the previous sections, there exist particular parameter domains in which nonlinear flow response actually dominates the flow generation of higher order harmonics: large transverse momentum, large centrality and large η/s, based on which the physical behavior of the observables can be explained. To complete the single-shot hydrodynamics framework with also nonlinear flow response, in this section we present the basic formulations.

Integrated harmonic flow

In realistic heavy-ion collision experiments, the measurements of harmonic flow needs to be designed in specified means so that the effects of event-by-event fluctuations are naturally contained in a events average process. For instance, as has been emphasized in the previous chapters, for the measured harmonic flow $v_n\{2\}$ from two-particle azimuthal correlations, the events average is implied in the definition, $v_n\{2\} = \langle\langle v_n^2 \rangle\rangle^{1/2}$. In our work, since the generated flow is formed in terms of linear and nonlinear flow response, as shown in the formulae Eq. (3.17), Eq. (3.18) and Eq. (3.19), the straightforward application leads to,

$$v_1\{2\} = \langle\langle |w_1 e^{-i\Phi_1} + w_{1(23)} e^{-i(3\Phi_3 - 2\Phi_2)}|^2 \rangle\rangle^{1/2} , \tag{3.27a}$$

$$v_4\{2\} = \langle\langle |w_4 e^{-i4\Phi_4} + w_{4(22)} e^{-i4\Phi_2}|^2 \rangle\rangle^{1/2} , \tag{3.27b}$$

$$v_5\{2\} = \langle\langle |w_5 e^{-i5\Phi_5} + w_{5(23)} e^{-i(3\Phi_3 + 2\Phi_2)}|^2 \rangle\rangle^{1/2} . \tag{3.27c}$$

In writing these equations, although only one type of nonlinear flow response is included for each of the harmonics, higher order corrections with more nonlinear contributions can be taken into account for better predictions. The flow response w's in Eq. (3.27) are proportional to their associated initial anisotropies, with the response coefficients extracted from hydrodynamics separately. With these analytical expressions, the detailed dependence of the predicted flow on

the transverse momentum, centrality and η/s through flow response coefficients, can be analyzed. Taking $v_4\{2\}$ for an example, squaring Eq. (3.27b) it is clear there are three terms in the average,

$$(v_4\{2\})^2 = \left(\frac{w_4}{\mathcal{C}_4}\right)^2 \langle\langle \mathcal{C}_4^2 \rangle\rangle + \left(\frac{w_{4(22)}}{\epsilon_2^2}\right)^2 \langle\langle \epsilon_2^4 \rangle\rangle + \frac{w_4}{\mathcal{C}_4}\frac{w_{4(22)}}{\epsilon_2^2} \langle\langle \mathcal{C}_4 \epsilon_2 \cos 4(\Phi_4 - \Phi_2) \rangle\rangle \,. \tag{3.28}$$

Note besides the contributions from pure linear and nonlinear flow response, there is a positive cross-term depending on the initial plane correlation. In general, the above form of the generated flow is expected for all of the harmonic orders, with pure linear and nonlinear contributions, together with cross-terms. Accordingly, the predicted behavior of the harmonic flow relies on a competition of these terms.

In Fig. 3.14, the predicted $v_n\{2\}$ for the LHC Pb-Pb collisions of harmonic order $n = 3, 4, 5$ and 6 are plotted as a function of centrality. Based on viscous hydrodynamic calculations, with respect to the lattice EOS, these curves roughly describe the behavior of harmonic flow of the observed pions. The separate contributions from linear and nonlinear terms are shown as well for comparisons.

First of all, we should notice the increasing relative contribution of nonlinear to linear flow response in the flow generation with the growth of centrality. This trend is more obvious for the higher harmonic flow. For ultra-central collisions, linear flow response is the dominant effect for v_3, v_4 and v_5, but not for v_6. As a result, for sufficiently large centrality, nonlinear flow response becomes the dominant mechanism for flow generation, as expected. When the associated initial plane correlation is negative, such as $\langle\langle \cos(\Phi_1 + 2\Phi_2 - 3\Phi_3) \rangle\rangle$ for $v_3\{2\}$, the cross-term has a negative contribution, as exhibited in Fig. 3.14. In calculating $v_4\{2\}$ and $v_6\{2\}$, we also include some higher order nonlinear terms. For $n = 4$, we take into account the contribution from $w_{4(13)}$. Shown in Fig. 3.14, the negligibly small $w_{4(13)}$ comparing to $w_{4(22)}$ makes the truncation of nonlinear flow flow generation to $w_{4(22)}$ reasonable. For $n = 6$, however, as illustrated in Fig. 3.14, in addition to the comparable nonlinear response of $w_{6(24)}$ and $w_{6(33)}$, in very peripheral collisions the cubic order contribution $w_{6(222)}$ is of considerably significance. More nonlinear terms in the calculation lead to a more complicated v_6 prediction, which will be seen later in the discussion on event plane correlations.

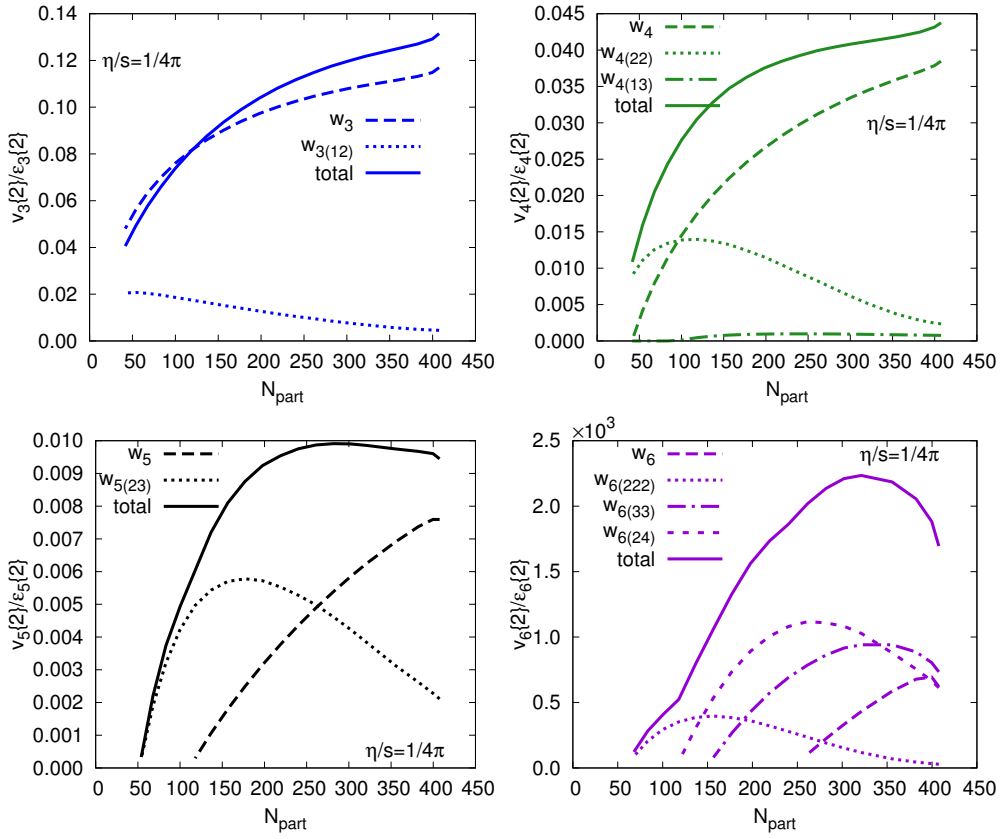

Figure 3.14: $v_n\{2\}$ as a function of centrality.

Harmonic flow $v_n\{2\}$ from two-particle correlations as a function of centrality, for $n = 3, 4, 5, 6$ for LHC Pb-Pb collisions, from viscous hydrodynamics. The contributions from linear and nonlinear terms are plotted separately. As expected, a trend of increasing contribution from nonlinear flow generation towards larger centrality is seen.

Differential harmonic flow

Let us discuss how this formalism can be used to study the p_T dependence of the flow. The particle spectra is expanded in harmonics

$$\frac{\mathrm{d}N}{\mathrm{d}p_T\mathrm{d}\phi_{\boldsymbol{p}}} \equiv \frac{\mathrm{d}N}{\mathrm{d}p_T}\left(1+\sum_{n=1}^{\infty} v_n(p_T)e^{in(\phi_{\boldsymbol{p}}-\Psi_n(p_T))}+\text{c.c.}\right), \tag{3.29}$$

where the phase, $\Psi_n(p_T)$, is in general a function of p_T. Then $v_n(p_T)\{2\}$ in the Ψ_n plane is normally defined as

$$v_n(p_T)\{2\} \equiv \begin{cases} \frac{\langle v_n(p_T)v_n\cos(n(\Psi_n(p_T)-\Psi_n))\rangle}{v_n\{2\}} & n>1 \\ -\frac{\langle v_1(p_T)v_1\cos(\Psi_1(p_T)-\Psi_1)\rangle}{v_1\{2\}} & n=1 \end{cases}, \tag{3.30}$$

where we have inserted an extra minus sign for $v_1(p_T)$, since the integrated v_1 is negative. The phase angle $\Psi_n(p_T)$ is often assumed to equal Ψ_n. Using the formalism outlined above we write $v_1(p_T)$ as a sum of the linear and nonlinear response

$$v_1(p_T)e^{-i\Psi_1(p_T)} = w_1(p_T)e^{-i\Phi_1} + w_{1(23)}(p_T)e^{-i3\Phi_3+i2\Phi_2}\,. \tag{3.31}$$

Then the numerator of $v_1(p_T)\{2\}$ is given by

$$\begin{aligned}&\langle\!\langle v_1(p_T)v_1\cos(\Psi_1(p_T)-\Psi_1)\rangle\!\rangle = \\ &\langle\!\langle w_1(p_T)w_1+w_{1(23)}(p_T)w_{1(23)}+\left[w_1(p_T)w_{1(23)}+w_{1(23)}(p_T)w_1\right]\cos(\Phi_1-3\Phi_3+2\Phi_2)\rangle\!\rangle\,,\end{aligned} \tag{3.32}$$

and the denominator is given by the integrated expression for $v_1\{2\}$, Eq. (3.27a). The corresponding result of $v_1\{2\}(p_t)$ is shown in Fig. 3.15. Similar expressions follow for $v_4\{2\}(p_T)$ and $v_5\{2\}(p_T)$.

Armed with the formulation of differential spectrum of harmonic flow, the asymptotic behavior of v_n, and in particular the Borghini-Ollitrault argument that $v_4 = \frac{1}{2}v_2^2$ and $v_5 = v_2v_3$ can be testified. Based on the analytical approximation of freeze-out Eq. (3.25), in ideal hydrodynamic calculations we expect the asymptotic relations between the linear and nonlinear flow response coefficients

$$\frac{w_{4(22)}/\epsilon_2^2}{(w_2/\epsilon_2)^2} \xrightarrow[p_T\to\infty]{} \frac{1}{2}\,, \qquad \frac{w_{5(23)}/(\epsilon_2\epsilon_3)}{(w_2/\epsilon_2)(w_3/\epsilon_3)} \xrightarrow[p_T\to\infty]{} 1\,. \tag{3.33}$$

When initial state fluctuations are considered for realistic heavy-ion collisions, corresponding to the measured harmonic flow $v_n\{2\}$, these asymptotic rela-

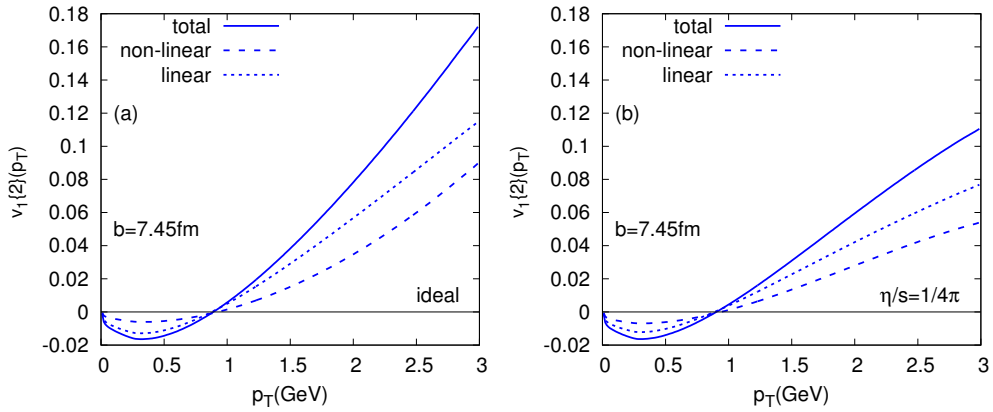

Figure 3.15: $v_1\{2\}(p_T)$ of mid-central collisions of LHC Pb-Pb experiments $v_1\{2\}(p_T)$ in ideal and viscous hydrodynamics from the linear response to ϵ_1, the nonlinear response to $\epsilon_2\epsilon_3$, and total response, as formulated in Eq. (3.30).

tions are modified [102],

$$\frac{v_4\{2\}}{v_2\{2\}^2} \xrightarrow[p_T\to\infty]{} \frac{1}{2}\left(\frac{\langle\langle\epsilon_2^4\rangle\rangle}{\langle\langle\epsilon_2^2\rangle\rangle^2}\right)^{1/2}, \quad \frac{v_5\{2\}}{v_2\{2\}v_3\{2\}} \xrightarrow[p_T\to\infty]{} \left(\frac{\langle\langle(\epsilon_2\epsilon_3)^2\rangle\rangle}{\langle\langle\epsilon_2^2\rangle\rangle\langle\langle\epsilon_3^2\rangle\rangle}\right)^{1/2}. \quad (3.34)$$

The value of these geometrical ratios are recorded as a function of centrality in Table 3.2. We have found that rather large p_T is needed to see the nonlinear limit given by Eq. (3.34). In the current framework, the linear and nonlinear response terms, and their interference, determine the full result. Fig. 3.16 shows the complete result for $v_4\{2\}/v_2\{2\}^2$ (scaled by $\langle\langle\epsilon_2^4\rangle\rangle/\langle\langle\epsilon_2^2\rangle\rangle^2$) for ideal and viscous hydrodynamics. Focusing on the ideal results, we see that full results (the solid lines) approach the nonlinear expectation of Borghini and Ollitrault (the dashed line) only very slowly. This is in large part because $w_4(p_T)$ is only qualitatively linear at sub-asymptotic p_T and increases almost quadratically at intermediate $p_T \sim 1.5\,\mathrm{GeV}$, momentarily keeping up with the nonlinear response. When viscous corrections are included, the nonlinear results become dominant in peripheral collisions. Similar results for v_5 in ideal and viscous hydrodynamics are also shown in Fig. 3.16. In the viscous case, the nonlinear result gives almost the full $v_5\{2\}$ for all centrality classes shown.

It is worth noting that the magnitude of the viscous corrections as a function of p_T for v_4 and v_5 are sensitive to ansatz used for the viscous distribution function, δf [60]. In particular, the quadratic ansatz used in this work assumes that the quasi-particle energy loss is independent of momentum, $dp/dt \propto$ const. A linear ansatz for δf is better motivated for QCD like

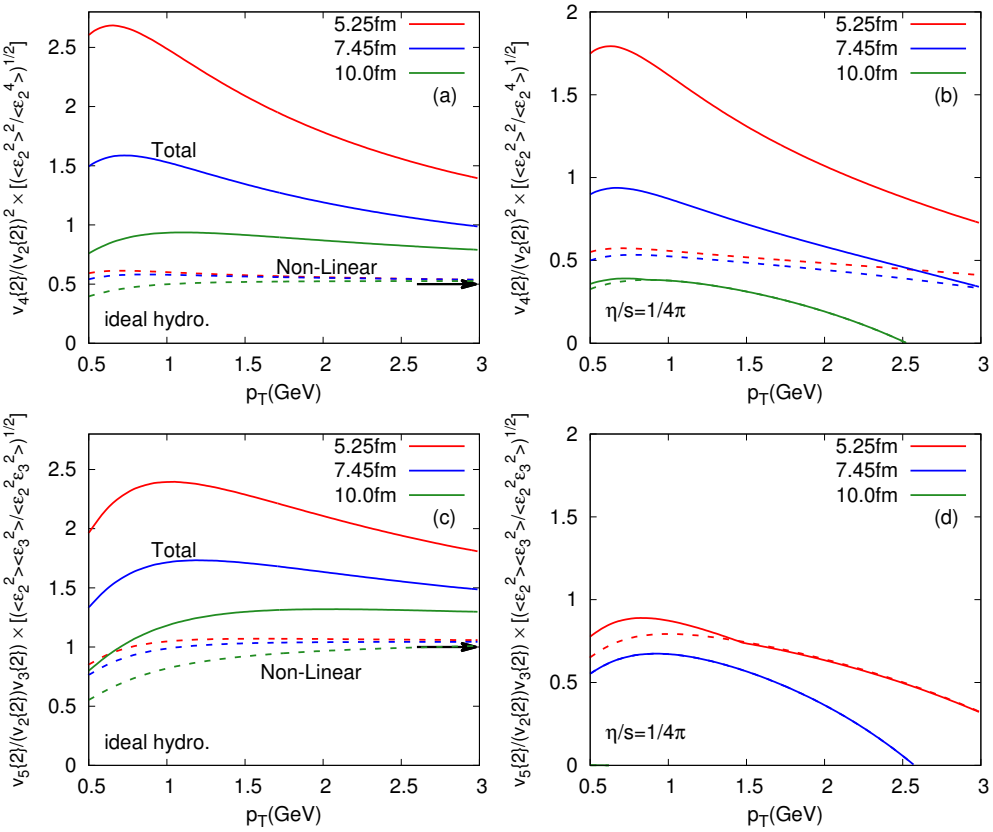

Figure 3.16: Scaling behavior of v_4 and v_5

Results for v_4 and v_5 for ideal and viscous hydrodynamics at various impact parameters. The Borghini-Ollitrault expectation is indicated by the arrows for the ideal v_4 and v_5 curves.

Table 3.2: Geometrical ratios in Eq. (3.34) as a function of centrality.

Centrality %	2.5	7.5	12.5	17.5	25.0	35.0	45.0	55.5
$\sqrt{\langle\langle\epsilon_2^4\rangle\rangle/\langle\langle\epsilon_2^2\rangle\rangle^2}$	1.40	1.33	1.26	1.22	1.20	1.18	1.17	1.16
$\sqrt{\langle\langle(\epsilon_2\epsilon_3)^2\rangle\rangle/(\langle\langle\epsilon_2^2\rangle\rangle\langle\langle\epsilon_3^2\rangle\rangle)}$	0.99	0.97	0.96	0.95	0.94	0.93	0.930	0.92
$\sqrt{\langle\langle\epsilon_2^2\rangle\rangle/\langle\langle\epsilon_1^2\rangle\rangle}$	2.12	2.78	3.22	3.46	3.56	3.40	3.04	2.64

theories and results in smaller viscous corrections for v_4 and v_5 as a function of p_T [103]. A complete discussion on this point is reserved in Chapter 5.

3.3 Discussion

We have presented a framework of medium response to understand the higher harmonics generated in heavy ion collisions. Then we extracted the linear and nonlinear response coefficients using ideal and viscous hydrodynamics and studied the dependence on the transverse momentum, centrality and shear viscosity. The pattern of viscous corrections is further analyzed in Fig. 3.5 and Fig. 3.12 and explained. Generally, when the harmonic order is large, the nonlinear response is less damped than the corresponding linear response. Thus, when viscosity is included in hydrodynamic simulations, the nonlinear response becomes increasingly important for higher harmonics. This qualitative reasoning is confirmed in Fig. 3.14. In these calculations with respect to the LHC energy, We see that the nonlinear response is essential for v_4, v_5 and v_6, and constitutes an important correction for v_3.

As long as higher order harmonics are not involved in the analyses, linear flow response formalism can be applied for realistic calculations. For instance, in Fig. 3.6 with ideal hydrodynamics and conformal EoS, the predicted $V_{3\Delta}/V_{2\Delta}$ is consistent with experiment. Since a simple one-to-one mapping is expected in the linear flow response formalism, the nont-trivial initial correlation between the dipole asymmetry and the ellipticity is found responsible for the measured correlator $\langle\cos(\phi_a+\phi_b-2\Psi_R)\rangle$ by STAR collaboration, as shown in Fig. 3.7. In addition, We noted that the strong correlation between the dipole asymmetry, ellipticity and the triangularity can be measured experimentally by measuring two-particle correlations with respect to reaction plane. The final result is a linear hydrodynamic prediction for a curious correlator $\langle\cos(\phi_a-3\phi_b+2\Psi_R)\rangle$, which is shown in Fig. 3.8.

The nonlinear response can be studied by analyzing the p_T dependence

of the flow harmonics. Fig. 3.16 exhibits scaling of $v_4\{2\}(p_T)$ and $v_5\{2\}(p_T)$. Fig. 3.15 shows the differential dipole flow $v_1\{2\}(p_T)$. In ideal hydrodynamics at large p_T we expect to find $v_4 = \frac{1}{2}v_2^2$ on an event by event basis. Our nonlinear response coefficients corroborate this nonlinear expectation for v_4 and an analogous relation for v_5, $v_5 = v_2 v_3$. However, since what is normally measured is $v_4\{2\}/(v_2\{2\})^2$ and not $\langle\langle v_4/v_2^2\rangle\rangle$, this ideal nonlinear expectation must be multiplied by $(\langle\langle\epsilon_2^4\rangle\rangle/\langle\langle\epsilon_2^2\rangle\rangle^2)^{1/2}$ when comparing to the experimental data [102]. In addition, this expectation of ideal hydrodynamics is broken by viscous corrections, and by the linear response to the fourth order cumulant $\mathcal{C}_4$ (*i.e.* ϵ_4). When all of these corrections are taken into account, we find that relations such as $v_4 = \frac{1}{2}v_2^2$ and $v_5 = v_2 v_3$ provide only a rough guide to the full result.

Throughout we have assumed perfect correlation between Ψ_2 and Φ_2 from linear flow response. This strict correlation is only approximately true. For instance the combination of a v_1 and a v_3 can yield a v_2,

$$v_2 e^{-i2\Psi_2} = w_2 e^{-i2\Phi_2} + w_{2(13)} e^{-i3\Phi_3+\Phi_1}\,. \tag{3.35}$$

This naturally provides a correlation between the Ψ_2 and Ψ_3 plane, although the geometric correlation between Φ_2 and Φ_3 is negligibly small. Indeed the (Ψ_2, Ψ_3) correlation, which was very recently observed by the ATLAS collaboration [104], is too large to be easily explained with the geometric correlations of the Glauber model. For the 6-th order harmonic flow, as illustrated in Fig. 3.14, there are more nonlinear terms that have comparable contributions to the generated flow. Therefore, in the flow response formalism to describe the v_6 flow generation with sufficient precision, we expect

$$v_6 e^{-i6\Psi_6} = w_6 e^{-i6\Phi_6} + w_{6(24)} e^{-i(4\Phi_4+2\Phi_2)} + w_{6(33)} e^{-i6\Phi_3} + w_{6(222)} e^{-i6\Phi_2}\,. \tag{3.36}$$

In particular, we note that the cubic coupling term is dominant for the very peripheral collisions.

Chapter 4

Event plane correlations

As one particular example of applying the nonlinear flow response formalism in realistic calculations, in this chapter we focus on the final state event plane correlation. Comparing to the harmonic flow v_n, which characterizes the magnitude of the azimuthal asymmetry of the expanding medium in heavy-ion collisions, final state plane correlations are related to the orientations of these asymmetries.

There are two reasons that event plane correlations demand a thorough analysis, especially theoretically. First, the non-trivial correlations of Ψ_n are essential for many of the observed signatures associated with the collective behavior of the medium. For instance, as we discussed in Section 3.1.3, the correlation $\langle\langle\cos(\Psi_1 - 3\Psi_3 + 2\Psi_2)\rangle\rangle$ plays a significant role in the expectation value of the measured two-particle correlation $\langle\cos(\phi_a+\phi_b-2\Psi_R)\rangle$. In addition, event plane correlations affect the measurement of the harmonic flow v_n in the event plane method. Taking the quadrapole flow v_4 for an example, one commonly applied measurements is to measure v_4 in the reaction plane of the second harmonic Ψ_2, which actually gives rise to a result $\propto \langle\langle\cos 4(\Psi_2 - \Psi_4)\rangle\rangle$. Second, as will be clarified later, the formation of these event plane correlations relies on the combined effect of initial state fluctuations and the flow response in medium. Therefore, not only the geometric information of the fluctuating initial state, *e. g.* the participant plane correlations in initial state, but also the properties of the medium, can be revealed by studying the event plane correlations.

With respect to the recent measurements by the ATLAS collaboration of a series of two-plane and three-plane event plane correlations [7], in this chapter, we present our predictions in the flow response formalism. A formulation of these event plane correlations in a single-shot hydrodynamics framework, based on linear and nonlinear flow response formalism is shown in Section 4.1. Comparing to the experiment data, and the results from event-by-event hydro-

dynamic simulations [87], the predicted event plane correlations for the LHC $\sqrt{s} = 2.76$ TeV Pb-Pb collisions are shown and analyzed in Section 4.2. In particular, from our formulation, the formation of these event plane correlations can be interpreted as the competing contributions from the 'linear limit' and 'nonlinear limit'.

4.1 Formulation of event plane correlations

The plane correlations in experiments are measured by event-plane method and multi-particle correlation method. We will focus on the event plane method which was used by the ATLAS collaboration. The details of this method were clarified by Luzum and Ollitrault [105] who showed that if the event plane method is used, the quantity that is measured depends on the reaction plane resolution.

For simplicity in the formulations, we make a further abbreviation for the complex form of the anisotropic flow in the particle spectrum $V_n = v_n e^{-in\Psi_n}$. We are interested in describing the correlations involving two and three event plane angles. For definiteness we will present formulas for a specific correlation, $\langle\langle\cos(4\Psi_4 - 2(2\Psi_2))\rangle\rangle$, which can be easily generalized to other harmonics (To aid the reader we have written $4\Psi_2 = 2(2\Psi_2)$ to expose the general pattern.) The 4-2 plane correlation is related to V_4 and V_2 through

$$\langle\langle\cos(4\Psi_4 - 2(2\Psi_2))\rangle\rangle = \left\langle\left\langle \frac{\mathrm{Re}\,(V_4 V_2^{*2})}{\sqrt{(V_4 V_4^*)(V_2 V_2^*)^2}} \right\rangle\right\rangle = \left\langle\left\langle \frac{w_4 \cos 4(\Phi_4 - \Psi_2) + w_{4(22)}}{|w_4 e^{-i4\Phi_4} + w_{4(22)} e^{-i4\Phi_2}|} \right\rangle\right\rangle . \tag{4.1}$$

Note that both linear and nonlinear response enter this formula for the event plane correlation.

The ATLAS collaboration quantified the event plane correlations by measuring related correlations between the experimental planes, $\hat{\Psi}_n$, as determined by the Q_n-vectors, $\boldsymbol{Q}_n = |Q_n| e^{-in\hat{\Psi}_n}$ (See the review: [106]). Further investigation showed that the measured quantity can not be directly interpreted as an event plane correlation in the form Eq. (4.1). The measured correlations correspond to Eq. (4.1) only if the event plane resolution approaches unity,

$$\langle\langle\cos(4\hat{\Psi}_2 - 2(2\hat{\Psi}_2))\rangle\rangle\{EP\} \rightarrow \left\langle\left\langle \frac{\mathrm{Re}\,(V_4 V_2^{*2})}{\sqrt{(V_4 V_4^*)(V_2 V_2^*)^2}} \right\rangle\right\rangle \qquad \text{(high resolution limit)}. \tag{4.2}$$

Here and below we have notated the experimental quantity with {EP} [7],

and the precise definition is carefully examined in [105]. We also note that the notation is misleading since the actual definition does not correspond to the average of a cosine, and can be greater than one. In the limit of low event plane resolution the measured quantities corresponds to

$$\langle\langle\cos(4\hat{\Psi}_2-2(2\hat{\Psi}_2))\rangle\rangle\{\mathrm{EP}\}\rightarrow\frac{\langle\langle\mathrm{Re}\,(V_4V_2^{*2})\rangle\rangle}{\sqrt{\langle\langle V_4V_4^*\rangle\rangle\langle\langle(V_2V_2^*)^2\rangle\rangle}}\qquad\text{(low resolution limit)}\tag{4.3}$$

Clearly Eq. (4.3) differs from Eq. (4.2) by the order of event average in these calculations. More generally the event plane measurements by ATLAS interpolate between these two limits.

As the actual resolution depends on the harmonic order and the detector acceptance, we will compute both the high resolution and low resolution limits and compare to the experimental data. In the future most of ambiguities in the measurement definition can be avoided by measuring

$$\frac{\langle\langle v_4v_2^2\cos(4\hat{\Psi}_2-2(2\hat{\Psi}_2))\rangle\rangle}{\sqrt{\langle\langle v_2^2\rangle\rangle^2\langle\langle v_4^2\rangle\rangle}}=\frac{\langle\langle\mathrm{Re}\,(V_4V_2^{*2})\rangle\rangle}{\sqrt{\langle\langle V_4V_4^*\rangle\rangle\langle\langle(V_2V_2^*)\rangle\rangle^2}}\tag{4.4}$$

as originally suggested in Ref. [107], and more recently in Ref. [105]. Such angular correlations have already been measured by the ALICE collaboration [108], but we will not address this preliminary data here. Certainly Eq. (4.4) is the most natural from the perspective of the response formalism developed in this work.

Finally, we give one additional example, $-8\Psi_2+3\Psi_3+5\Psi_5$ of how a three plane correlation function is calculated in the high and low resolution limits in order to avoid confusiion

$$\langle\langle\cos(-4(2\hat{\Psi}_2)+3\hat{\Psi}_3+5\hat{\Psi}_5)\rangle\rangle\{\mathrm{EP}\}\rightarrow\left\langle\!\!\left\langle\frac{\mathrm{Re}\,(V_2^{*4}V_3V_5)}{\sqrt{(V_2V_2^*)^4(V_5V_5^*)(V_3V_3^*)}}\right\rangle\!\!\right\rangle\qquad\text{(high resolution)}\tag{4.5}$$

$$\langle\langle\cos(-4(2\hat{\Psi}_2)+3\hat{\Psi}_3+5\hat{\Psi}_5)\rangle\rangle\{\mathrm{EP}\}\rightarrow\frac{\langle\langle\mathrm{Re}\,(V_2^{*4}V_3V_5)\rangle\rangle}{\sqrt{\langle\langle(V_2V_2^*)^4\rangle\rangle\langle\langle V_3V_3^*\rangle\rangle\langle\langle V_5V_5^*\rangle\rangle}}\qquad\text{(low resolution)}\tag{4.6}$$

In the future the quantity which is most easily compared to theoretical calculations is

$$\frac{\langle\langle v_2^4v_3v_5\cos(-4(2\hat{\Psi}_2)+3\hat{\Psi}_3-5\hat{\Psi}_5)\rangle\rangle}{\sqrt{\langle\langle v_2^2\rangle\rangle^4\langle\langle v_3^2\rangle\rangle\langle\langle v_5^2\rangle\rangle}}=\frac{\langle\langle\mathrm{Re}\,(V_2^{*4}V_3V_5)\rangle\rangle}{\sqrt{\langle\langle V_2V_2^*\rangle\rangle^4\langle\langle V_3V_3^*\rangle\rangle\langle\langle V_5V_5^*\rangle\rangle}}\tag{4.7}$$

4.2 Predictions

Fig. 4.1 and Fig. 4.2 show a comparison of the measured two and three plane correlation functions with the response formalism. From the inspection of these correlations we make the following observations. First, many of the most important correlation functions are nicely reproduced at least if the high resolution limit is used. The agreement with the low resolution limit is not as good. The ambiguities in the measurement can be avoided by taking definite moments as in Eq. (4.4) [107]. Examining the definitions of the high and low resolution limits (Eqs. 4.2 and 4.3), we see that the difference between the two measurements can be best quantified by measuring the probability distribution $P(v_n)$ [109] or the moments of this distribution, e.g. for v_2

$$(v_2\{2\})^4 \equiv \langle\langle v_2^2 \rangle\rangle \quad \text{and} \quad (v_2\{4\})^4 \equiv -\left[\langle\langle v_2^4 \rangle\rangle - 2\langle\langle v_2^2 \rangle\rangle\right] . \tag{4.8}$$

It is then a separate and important question wether the response formalism outlined here can reproduce these probability distributions. This will be addressed in future work.

There are a few correlations which are seemingly not well reproduced even for in the high resolution limit. First, one could hope for better agreement between correlations involving Ψ_6, such as $\langle\langle\cos(6\Psi_3 - 6\Psi_6)\rangle\rangle$ and $\langle\langle\cos(6\Psi_2 - 6\Psi_6)\rangle\rangle$. In Fig. 4.4 and (4.5), we have replaced the PHOBOS calculation with Glissando [9] and the agreement with the Ψ_6 correlations is somewhat better, though not markedly so. The most troubling correlation function which is not qualitatively reproduced by the response formulation is $\langle\langle\cos(2\Psi_2 - 6\Psi_3 + 4\Psi_4)\rangle\rangle$. This correlation is not independent from the other correlations that are not reproduced.

Origin of these correlations

It is important and instructive to understand the hydrodynamic origin of the correlations presented in these figures. This is best understood by examining the linear and nonlinear contributions separately. Fig. 4.3(a) and (b) illustrate this decomposition of the correlations $\langle\langle\cos(4\Psi_2 - 4\Psi_4)\rangle\rangle$ and $\langle\langle\cos(2\Psi_2 + 3\Psi_3 - 5\Psi_5)\rangle\rangle$ respectively. The naive (moment based) expectation of the Glauber model is shown in Fig. 4.3 by the dotted line and has the wrong sign. As was explained in Section 2.3, in this approach the correlation is assumed to arise from the initial state participant fluctuations and the angles associated with these moments.

In a more strict manner, the cumulant defined initial anisotropies should be taken. Then with only linear flow response formalism in hydrodynamic

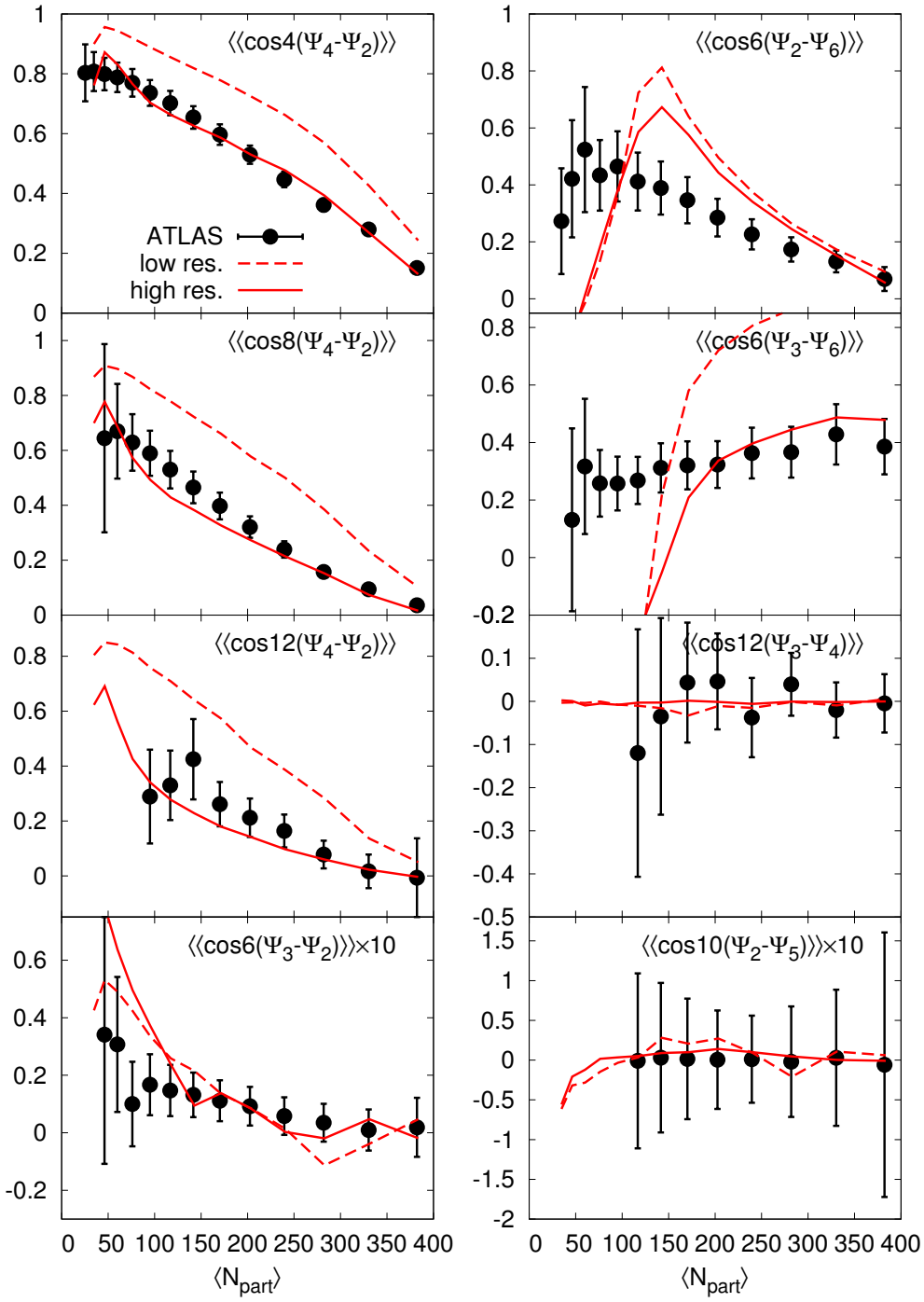

Figure 4.1: Two-plane event plane correlations. The solid curves are the predictions based on a high resolution assumption. The dashed curves are obtained in the low resolution limit. Data points are taken from the ATLAS measurements [7].

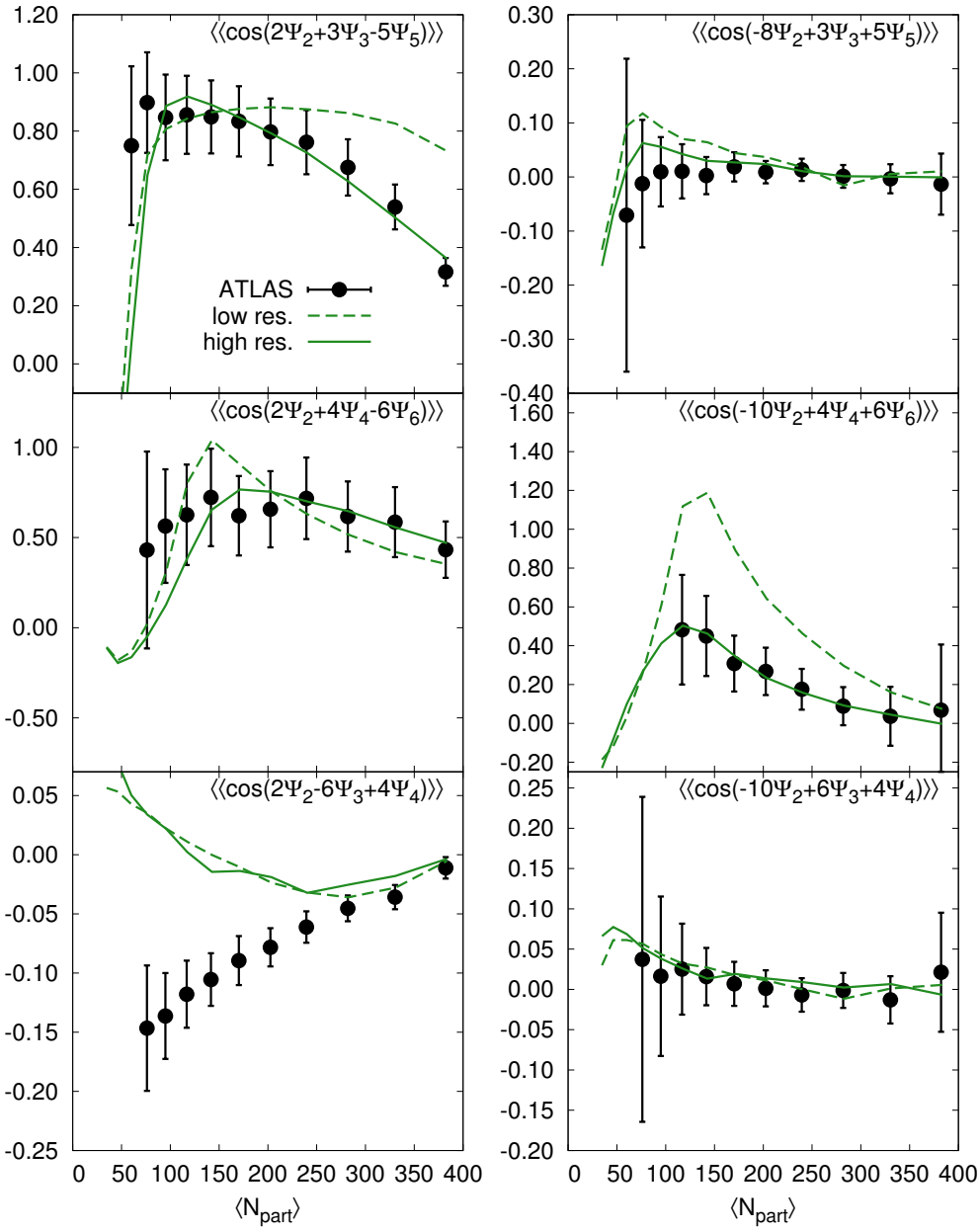

Figure 4.2: Three-plane event plane correlations. The solid curves are the predictions based on a high resolution assumption. The dashed curves are obtained in the low resolution limit. Data points are taken from the ATLAS measurements [7].

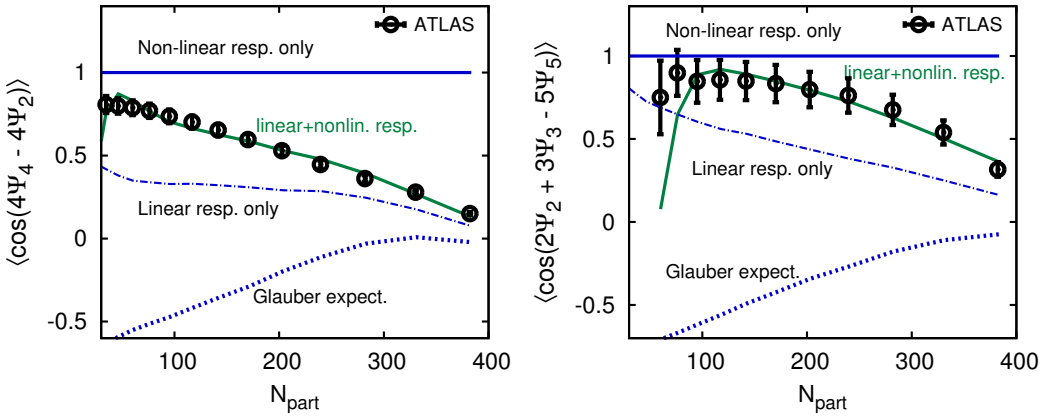

Figure 4.3: Decomposition of the event-plane correlations into the 'linear limit' and 'nonlinear limit', corresponding to the formation of event-plane correlations from initial geometry and medium expansion.

simulations, these initial participant correlations are identically transformed into event plane correlations, giving rise to these dash-dotted curves in Fig. 4.3. In the flow response formalism, this linear one-to-one mapping between the initial and final state plane correlations, which we refer as the 'linear limit', can be recognized as a result of neglecting the nonlinear response in these formulations. For example, the following results

$$\langle\langle \cos 4(\Psi_4 - \Psi_2) \rangle\rangle \xrightarrow{\frac{w_4}{w_{4(22)}} \to \infty} \langle\langle \cos 4(\Phi_4 - \Phi_2) \rangle\rangle \,, \tag{4.9a}$$

$$\langle\langle \cos(2\Psi_2 + 3\Psi_3 - 5\Psi_5) \rangle\rangle \xrightarrow{\frac{w_5}{w_{5(23)}} \to \infty} \langle\langle \cos(2\Phi_2 + 3\Phi_3 - 5\Phi_5) \rangle\rangle \,, \tag{4.9b}$$

can be achieved in both high resolution limit Eq. (4.2) and low resolution limit Eq. (4.3). The 'linear limit' of these correlations reflects the original initial state plane correlations. On the other hand, if in these formulations the linear flow response are neglected, the 'nonlinear limit' results which entirely rely on nonlinear flow response contributions are obtained. The 'nonlinear limit' reflects the formation of event plane correlation from medium evolution. For the 4-2 and 2-3-5 event plane correlations in Fig. 4.3, it is not difficult to see that the pure nonlinear flow response generates perfect correlations, *i. e.* 1. Since the two distinguished effects contribute simultaneously, the observed correlations should lie somewhere between these two limits. As known from the systematic analyses on the flow response in Chapter 3, the relative contributions to the flow generation from nonlinear flow response grows with

centrality. Consequently, starting from a correlation close to the 'linear limit' prediction, the event plane correlation is expected to approach the 'nonlinear limit' with respect to the increase of collision centrality, which explains the curves in Fig. 4.3.

Error estimate in our simulations

In reproducing these event plane correlation functions, there exists a practical issue related to the linear and nonlinear flow response coefficients from our viscous hydrodynamics. For some of the peripheral collisions we have the spurious negative flow response coefficients, as discussed in Section 3.1.2. One way of avoiding this physical inconsistency is to truncate abruptly these coefficients as a function of centrality when they cross zero. Although introducing the cut in these flow response is not a perfect solution to the problem, it is instructive to check the extent to which our hydrodynamics (also hydrodynamic simulations of most other groups) overestimates the viscous effect in these peripheral collisions.

In Fig. 4.4 and Fig. 4.5, besides our prediction with a non-cut flow response coefficients shown in the solid lines, the results with a cut on the flow response coefficients are plotted as these dashed lines. For these correlations in the LHC Pb-Pb collisions, when $\langle N_{\rm part}\rangle$ is less 200 or so, corresponds to a centrality of $\gtrsim 20\%$, the effects are noticeable. And this is the region in which our predictions miss the experimental observations. Comparing the non-cut and cut predictions, we have a rough estimate of the errors in the our viscous hydrodynamic framework. Since viscous damping effects are more significant for higher order harmonic flow, it is not surprise to expect the large uncertainties in correlations, such as $\langle\langle\cos(6\Phi_2 - 6\Phi_6)\rangle\rangle$ and $\langle\langle\cos(6\Phi_3 - 6\Phi_6)\rangle\rangle$.

4.3 Discussion

With PHOBOS MC-Glauber model, and $\eta/s = 1/4\pi$ in viscous hydrodynamics with the freeze-out temperature $T_{\rm fo} = 150$MeV, our predictions for the event-plane correlations qualitatively match the experiment, except $\langle\langle\cos(2\Psi_2 - 6\Psi_3 + 4\Psi_4)\rangle\rangle$ at non-central bins. Considering we only have nonlinear flow generations from some of the primary nonlinear terms, and for the calculations which aim mainly at interpretations, the results are acceptable. The comparison of our predictions to the event-by-event hydrodynamics as well [87] show some consistency, in particular the dependence on the medium shear viscosity. All of these verify the applicability of the nonlinear flow response formalism in heavy-ion collisions on an event-by-event basis.

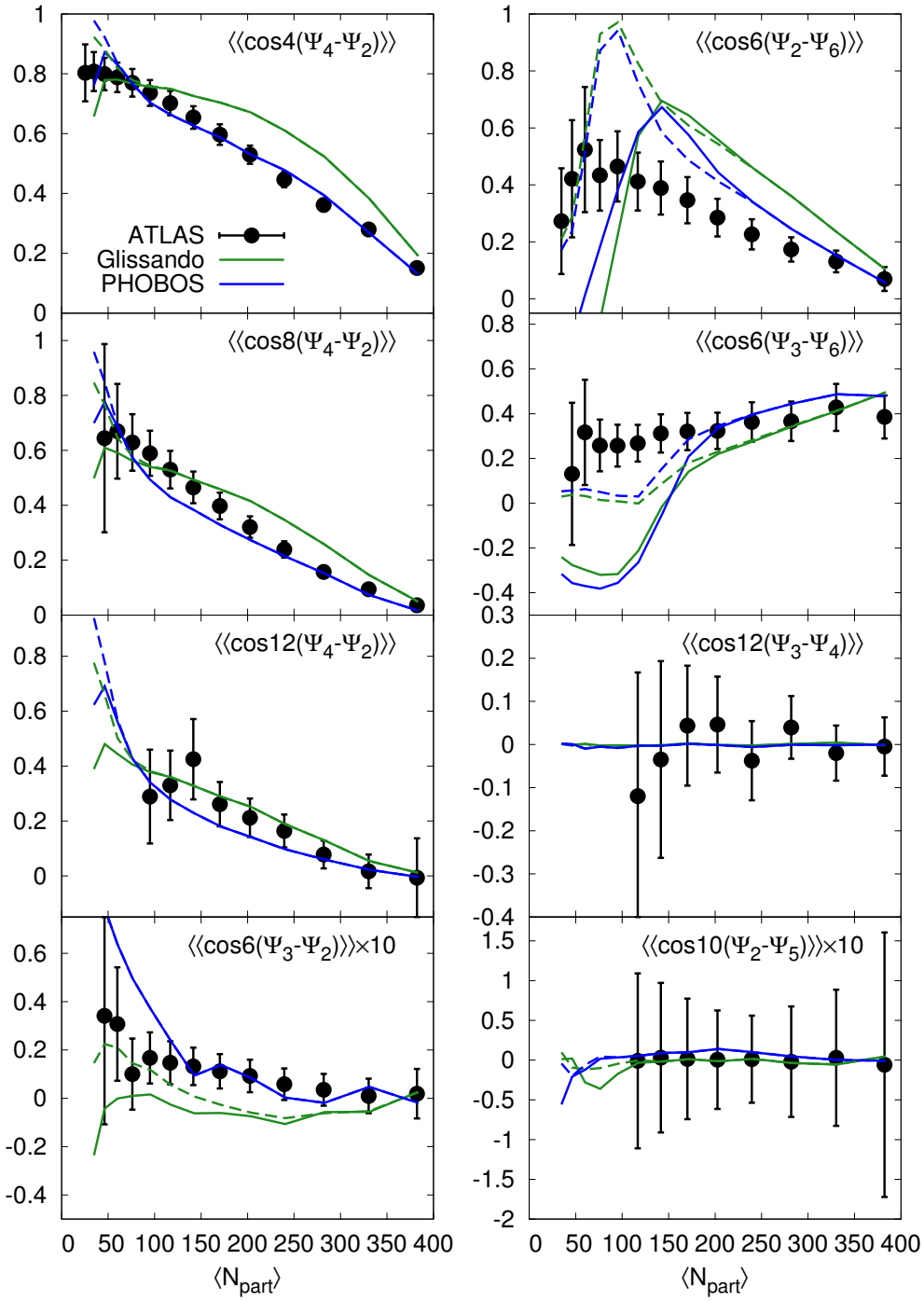

Figure 4.4: Two-plane event plane correlations based on PHOBOS Glauber [8] and Glissando Glauber [9] models. The solid curves correspond to the 'non-cut' calculations, while the dashed curves correspond to the 'cut' calculations. (See text)

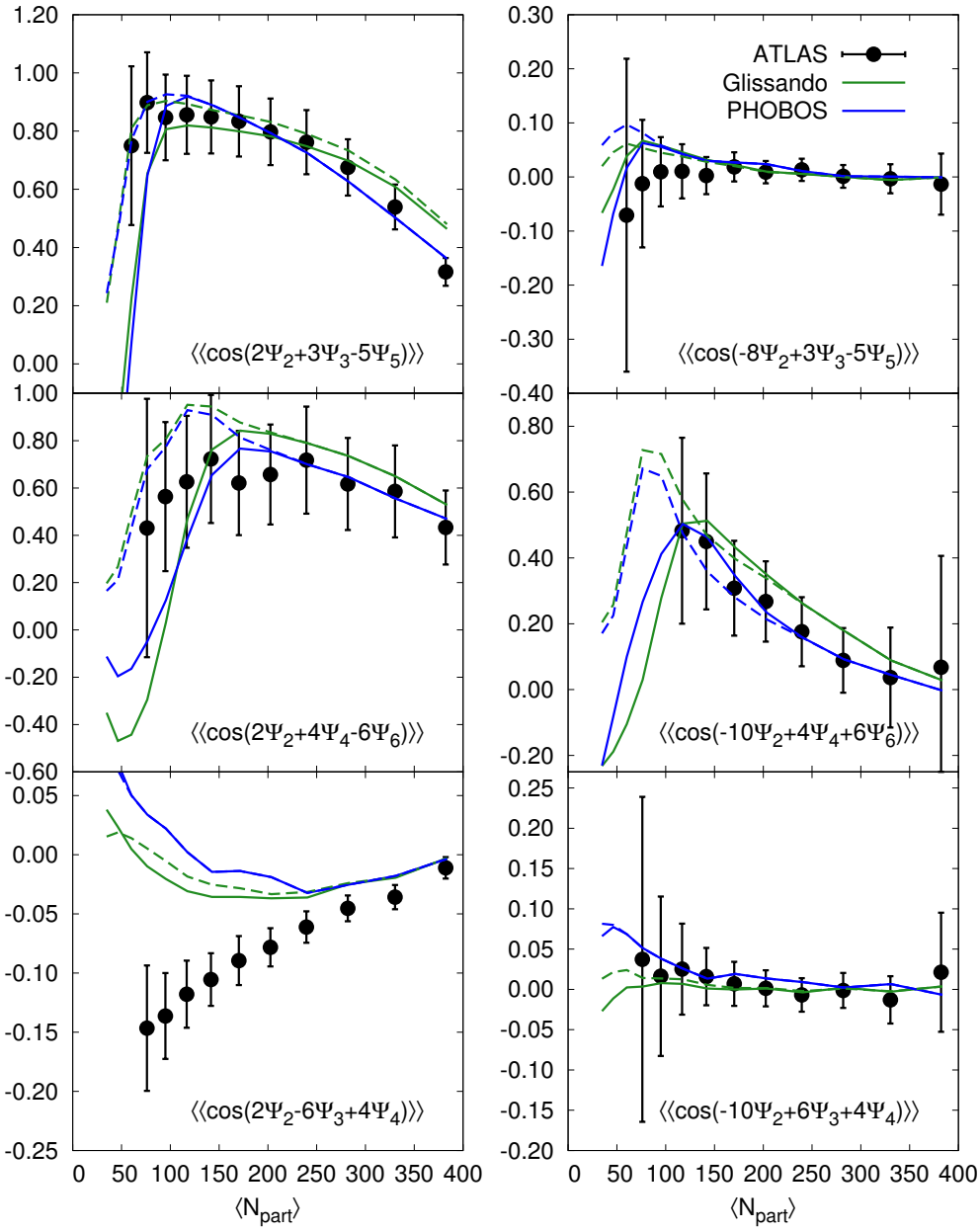

Figure 4.5: Three-plane event plane correlations based on PHOBOS Glauber [8] and Glissando Glauber [9] models. The solid curves correspond to the 'non-cut' calculations, while the dashed curves correspond to the 'cut' calculations. (See text)

The advantage of the flow response formalism is demonstrated in the analysis in Section 4.2. As the dependence on the medium property of the flow response is systematically studied in Chapter 3, the influence of the medium expansion on the observed event plane correlations can be understandable. For instance, the enhancement of the correlation $\langle\langle\cos(4\Psi_4 - 4\Psi_2)\rangle\rangle$ is well interpreted as the increase of nonlinear flow response effect. With the similar 'linear limit' and 'nonlinear limit' arguments, the patterns of the plane correlations can be related to the medium properties. Especially, since the η/s dependence of flow response is well established theoretically, extraction of shear viscosity from these plane correlations can be expected.

The viscous effect from hydrodynamics for the peripheral collisions is questionable. Since the viscous hydrodynamics framework is not consistent, which we will address in Chapter 5, there exists uncertainty of our predictions for the peripheral collision bins.

Chapter 5

Second order viscous corrections, $\delta f_{(2)}$

One of the primary goals of viscous hydrodynamic simulations with respect to the realistic heavy-ion collisions is the extraction of the transport coefficients of the QGP medium, in particular the shear viscosity to entropy ratio η/s. Progresses towards this direction have been made based on the realization of initial state fluctuations, since the observed harmonics in experiment have obtained an substantial extension, with not only elliptic flow v_2, but also v_1, v_3, up to v_6 measured quantitatively. These new signatures, *e. g.* $v_n\{2\}$ and event plane correlations, supply more constraints and thus a better determination of η/s. However, as noticed in the viscous hydrodynamic calculations, also discussed in the previous chapters, the predicted flow response of higher harmonic orders is negative as long as the viscous effects are sufficiently large, *e. g.* with large input η/s or small system size. These unphysical results reflect the over-estimates of viscous damping effect of present hydrodynamic framework.

In hydrodynamics, dissipative effects are included in two aspects: the viscous hydrodynamic equations of motion and the viscous corrections to the phase space distribution function at freeze-out $\delta f(x, \boldsymbol{p})$. Although both of the two aspects are responsible for viscous damping in hydrodynamics, the effect of $\delta f(x, \boldsymbol{p})$ is generally the dominant one [103]. In Fig. 5.1, a series of viscous hydrodynamic simulations give rise to the 4-th order linear and nonlinear flow response coefficients, as a function of transverse momentum. The formal calculations, *i. e.* considering viscous equations of motion and $\delta f(x, \boldsymbol{p})$ simultaneously, with respect to a increase of input η/s, demonstrate a substantial viscous damping. In particular, when $\eta/s = 2/4\pi$ the flow response coefficients cross zero at large p_T. Comparing to the moderate viscous suppression when effects of $\delta f(x, \boldsymbol{p})$ is neglected, the grey curves in Fig. 5.1, it is reasonable to

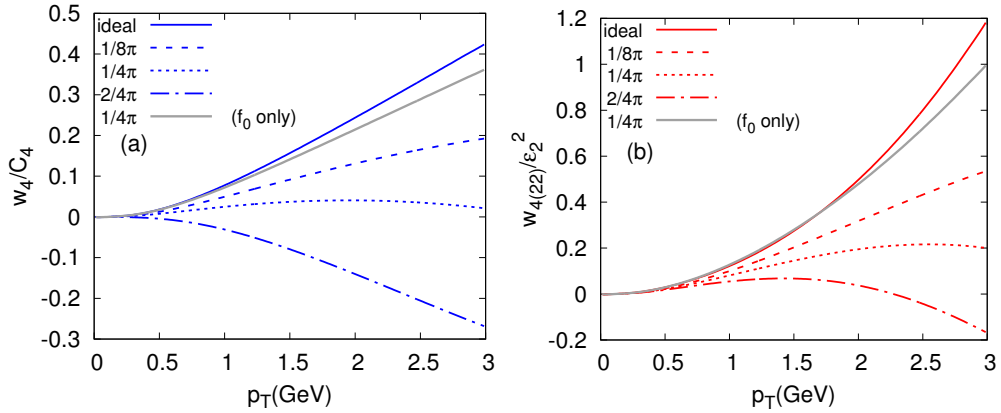

Figure 5.1: $w_4(p_T)$ and $w_{4(22)}(p_T)$ from hydrodynamics with different η/s. The p_T dependent linear and nonlinear flow response w_4 and $w_{4(22)}$ from a series hydrodynamic simulations with increasing value of η/s. To distinguish the effect of freeze-out δf, calculations with only ideal distribution f_0 are shown in the grey color.

attribute the obtained negative flow response to the inappropriate formulation of $\delta f(x, \boldsymbol{p})$.

The treatment of the viscous corrections to the phase space distribution function at freeze-out in current hydrodynamic simulations is truncated at first order, $\delta f_\pi(x, \boldsymbol{p})$, in which viscous corrections of the order of only first spatial gradient are consistently considered, in the form of Eq. (1.35). On the other hand, due to the causality problem of hydrodynamic theory, the equations of motion with viscous corrections of up to second order in gradients are used practically. For instance, the BRSSS hydrodynamics Eq. (1.32) has been found in realistic calculations with convergence, and especially to the measured harmonic flow. The inconsistency between the equations of motion and δf_π, and the consequent over-estimate of viscous damping in the calculations of higher order harmonic flow, consist the major motivation of this part of our work.

To compute the viscous corrections to the phase space distribution we will analyze kinetic theory of a conformal gas close to equilibrium in a relaxation time approximation. This extreme idealization is still useful for several reasons. First, a similar equilibrium analysis of QCD kinetic theory was used to determine the second order transport coefficients to leading order in α_s [110]. This analysis (which will be discussed further below) makes clear that the details of the collision integral hardly matter in determining the second order transport coefficients. Indeed, we will see that the structure of the second order viscous correction $\delta f_{(2)}$ is largely determined by the kinematics of free

streaming, rather than the details of the collision integral. Thus, an analysis based on a relaxation time approximation is an easy way to reliably estimate the size of such second order corrections in heavy ion collisions. Second, the overall normalization of $\delta f_{(2)}$ is constrained by the second order transport coefficients τ_π and λ_1, in much the same way that the shear viscosity constrains the normalization of $\delta f_{(1)}$. These constraints allow us to make a good estimate of the form of viscous corrections at second order for a realistic non-conformal fluid.

With this functional form we study the effect of $\delta f_{(2)}$ on the harmonic spectrum in heavy ion collisions. In Section 5.1 we outline how $\delta f_{(2)}$ is computed in kinetic theory. Then, in Section 5.2 we discuss the practical implementation of this formula in a hydrodynamic code used to simulate heavy ion collisions. These results are used to simulate the linear response to a given deformation, ϵ_n. The linear response is largely responsible for determining the v_n in central collisions. In non-central collisions the linear response *and* the quadratic response determine the harmonic flow and its correlations [57, 70, 71, 85, 95], but the quadratic response will not be discussed in this initial study. Finally, we will summarize the effects of $\delta f_{(2)}$ in Section 5.3.

5.1 2nd order corrections to $f(x, \boldsymbol{p})$

5.1.1 Hydrodynamics

In evaluating $\delta f_{(2)}$ to second order we will need the hydrodynamic equations of motion. Throughout this analysis we are working with a conformal fluid and consequently the bulk viscosity is set zero, $\zeta = 0$. For a conformal fluid the possible tensor forms of the gradient expansion for $\pi^{\mu\nu}$ through second order were established by BRSSS

$$\pi^{\mu\nu} = \pi^{\mu\nu}_{(1)} + \pi^{\mu\nu}_{(2)} + \ldots = -\eta\sigma^{\mu\nu} + \eta\tau_\pi \left[\langle D\sigma^{\mu\nu} \rangle + \frac{1}{d-1}\sigma^{\mu\nu}\partial\cdot u \right] + \lambda_1 \left\langle \sigma^{\mu}{}_{\lambda}\sigma^{\nu\lambda} \right\rangle + \lambda_2 \left\langle \sigma^{\mu}{}_{\lambda}\Omega^{\nu\lambda} \right\rangle + \lambda_3 \left\langle \Omega^{\mu}{}_{\lambda}\Omega^{\nu\lambda} \right\rangle + \ldots , \quad (5.1)$$

Rewriting hydrodynamic equations of motion, to express the time derivatives of energy density and flow velocity in terms of the spatial gradients of these

fields

$$D\varepsilon = -(\varepsilon+\mathcal{P})\nabla\cdot u + \frac{\eta}{2}\sigma_{\mu\nu}\sigma^{\mu\nu} + \dots\,, \tag{5.2a}$$

$$Du_\mu = -\frac{\Delta_\mu \mathcal{P}}{\varepsilon+\mathcal{P}} - \frac{\Delta_{\mu\lambda_2}\,\partial_{\lambda_1}\pi^{\lambda_1\lambda_2}}{\varepsilon+\mathcal{P}} \tag{5.2b}$$

$$= -\frac{\nabla_\alpha \mathcal{P}}{\varepsilon+\mathcal{P}} + \frac{\eta}{\varepsilon+\mathcal{P}}\left[(d-2)\left\langle\sigma_{\mu\lambda}\nabla^\lambda \ln T\right\rangle + \left\langle\nabla_\lambda \sigma^\lambda_{\ \mu}\right\rangle\right] + \dots\,. \tag{5.2c}$$

is crucial for the following derivations. The ellipses in Eq. (5.2) denote terms third order in the gradients. In passing from Eq. (5.2b) to Eq. (5.2c) we have used the first order expression for $\pi^{\mu\nu} = -\eta\sigma^{\mu\nu}$, the conformal temperature dependence of $\eta \propto T^{d-1}$, and the lowest order equations of motion Eq. (1.23).

In hydrodynamic simulations of heavy ion collisions the static form of the constituent relation Eq. (5.1) is not used. Rather, this equation is rewritten as a dynamical equation for $\pi_{\mu\nu}$ which is evolved numerically [111]

$$\begin{aligned}\pi^{\mu\nu} = &-\eta\sigma^{\mu\nu} - \tau_\pi\left[\left\langle D\pi^{\mu\nu}\right\rangle + \frac{d}{d-1}\pi^{\mu\nu}\nabla\cdot u\right] + \frac{\lambda_1}{\eta^2}\left\langle \pi^\mu_{\ \lambda}\pi^{\nu\lambda}\right\rangle \\ &- \frac{\lambda_2}{\eta}\left\langle \pi^\mu_{\ \lambda}\Omega^{\nu\lambda}\right\rangle + \lambda_3\left\langle \Omega^\mu_{\ \lambda}\Omega^{\nu\lambda}\right\rangle\,.\end{aligned} \tag{5.3}$$

Similarly, when constructing δf at first and second order we will systematically replace $\sigma_{\mu\nu}$ with $-\pi_{\mu\nu}/\eta$. For fluids with an underlying kinetic description, the transport coefficients are additionally constrained, with $\lambda_3 = 0$ and $\lambda_2 = -2\eta\tau_\pi$ [110], and these relations used in the simulation. The appropriate values for λ_1 and $\eta\tau_\pi$ will be discussed below.

5.1.2 Kinetics

To determine the viscous corrections to the distribution function we will solve the kinetic equations in a relaxation time approximation through second order in the gradient expansion

$$f_{\boldsymbol{p}} \equiv n_{\boldsymbol{p}} + \delta f_{\boldsymbol{p}} = n_{\boldsymbol{p}} + \delta f_{(1)} + \delta f_{(2)} + \dots\,. \tag{5.4}$$

In a relaxation time approximation the Boltzmann equation reads

$$p^\mu \partial_\mu f_{\boldsymbol{p}}(x) = -\frac{T^2}{\mathcal{C}_p}\left[f_{\boldsymbol{p}}(x) - n(-p\cdot u_*(x)/T_*(x))\right]\,, \tag{5.5}$$

where the dimensionless coefficient $\mathcal{C}_p$ is related to the canonically defined momentum dependent relaxation time

$$\mathcal{C}_p = T^2 \frac{\tau_R(E_p)}{E_p} \,. \tag{5.6}$$

Following Ref. [103], we will parametrize the momentum dependence of the relaxation time as a simple power law

$$\tau_R \propto E_{\boldsymbol{p}}^{1-\alpha} \,, \tag{5.7}$$

with α between zero and one. As we will see below, $\alpha = 0$ gives a first order a viscous correction which grows quadratically with momentum (which is known as the quadratic ansatz), while $\alpha = 1$ gives a first order viscous correction which grows linearly with momentum (and is known as the linear ansatz).

At leading order, the parameters T_* and U_*^μ which appear in the kinetic equation are equal to the Landau matched temperature and flow velocity, T and u^μ. However, starting at second order T_* and U_*^μ will differ from T and u^μ by squares of gradients:

$$T_*(x) \equiv T(x) + \delta T_*(x) \,, \tag{5.8a}$$
$$u_*^\mu(x) \equiv u^\mu(x) + \delta u_*^\mu(x) \,. \tag{5.8b}$$

δT_* and δU_*^μ will be determined at each order by the Landau matching condition:

$$T^{\mu\nu} u_\nu = e u^\mu \,.$$

Expanding $n(-p \cdot u_*/T_*)$ we have

$$n_{\boldsymbol{p}}^* \equiv n_{\boldsymbol{p}} + \delta n_p^* \qquad \delta n_{\boldsymbol{p}}^* = n'_{\boldsymbol{p}} \left[-\frac{p \cdot \delta u_*}{T} - E_p \frac{\delta T_*}{T^2} \right] + \ldots \,, \tag{5.9}$$

where we have used an obvious notation, $n_p^* \equiv n(-p \cdot u_*/T_*)$ and $n_{\boldsymbol{p}} \equiv n(-p \cdot u/T)$.

Then to determine δf we substitute the expansion (Eq. (5.4)) into the relaxation time equation and equate orders. In doing so we use the hydrodynamic equations of motion through second order to write time derivatives of $T(X)$ and $U^\mu(X)$ in terms of spatial gradients of these fields. For instance,

using the equations of motion Eq. (5.2) and the thermodynamic identities

$$c_v = \frac{d\varepsilon}{dT}\,, \qquad \frac{1}{T(\varepsilon+\mathcal{P})}d\mathcal{P} + d\left(\frac{1}{T}\right) = 0\,, \qquad c_s^2 = \frac{\varepsilon+\mathcal{P}}{Tc_v}\,, \tag{5.10}$$

and the relations $|\boldsymbol{p}|^2 = E_p^2$ and $c_s^2 = 1/(d-1)$ of a conformal gas, we have

$$p^\mu \partial_\mu n_{\boldsymbol{p}} = -n'_{\boldsymbol{p}} \frac{p^\mu p^\nu}{2T}\sigma_{\mu\nu} - \frac{n'_p}{(\varepsilon+\mathcal{P})T}\Big[-E_p p^{\mu_1}\Delta_{\mu_1\mu_2}\partial_\lambda \pi^{\lambda\mu_2} + \tfrac{1}{2}E_{\boldsymbol{p}}^2 c_s^2\,\eta\sigma^2\Big] + \dots\,. \tag{5.11}$$

The term linearly proportional to $\sigma_{\mu\nu}$ is ultimately responsible for the shear viscosity, while the nonlinear terms contribute to $\delta f_{(2)}$.

With this discussion, we find that the δf is determined by the hierarchy of equations:

$$\delta f^\sigma_{(1)} = \mathcal{C}_p n'_p \frac{p^\mu p^\nu \sigma_{\mu\nu}}{2T^3}\,, \tag{5.12}$$

and

$$\delta f^\sigma_{(2)} = \delta n^*_{\boldsymbol{p}} + \frac{\mathcal{C}_p n'_{\boldsymbol{p}}}{(\varepsilon+\mathcal{P})T^3}\Big[-E_p p^{\mu_1}\Delta_{\mu_1\mu_2}\partial_\lambda\pi^{\lambda\mu_2} + \tfrac{1}{2}E_{\boldsymbol{p}}^2 c_s^2\,\eta\sigma^2\Big] - \frac{\mathcal{C}_{\boldsymbol{p}}}{T^2}\,p^\mu\partial_\mu \delta f^\sigma_{(1)}\,. \tag{5.13}$$

Straightforward algebra uses the equations of motion to decompose $\delta f_{(2)}$ into irreducible tensors, and determines the final form of $\delta f^\sigma_{(1)}$ and $\delta f^\sigma_{(2)}$ (see Appendix C).

We have put a superscript σ in $\delta f^\sigma_{(1)}$ and $\delta f^\sigma_{(2)}$ to indicate that that we are using $\sigma_{\mu\nu}$ rather than $\pi_{\mu\nu}$ in these equations. In realistic hydrodynamic simulations of heavy ion collisions $\pi_{\mu\nu}$ is treated as a dynamic variable, and $-\eta\sigma_{\mu\nu}$ is systematically replaced by $\pi_{\mu\nu}$. This yields the following reparameterization of δf

$$\delta f_{(1)} = -\tfrac{1}{2}\mathcal{C}_p n'_p \frac{p^\mu p^\nu}{\eta T^3}\pi_{\mu\nu}\,, \tag{5.14a}$$

$$\delta f_{(2)} = \delta f^\sigma_{(2)} + \tfrac{1}{2}\mathcal{C}_p n'_p \frac{p^\mu p^\nu}{\eta T^3}\left[\pi_{\mu\nu} + \eta\sigma_{\mu\nu}\right]\,, \tag{5.14b}$$

where we have replaced $\sigma_{\mu\nu}$ with $-\pi_{\mu\nu}/\eta$ in the first order result, and appended the difference between these two tensors to the second order result so that, $\delta f_{(1)} + \delta f_{(2)} = \delta f^\sigma_{(1)} + \delta f^\sigma_{(2)}$ up to third order terms.

To record the result for $\delta f_{(2)}$, we first review the familiar first order case. At first order, $\delta f_{(1)}$ is described by a dimensionless scalar function $\chi_{0p}(E_p/T)$

$$\delta f_1 = \chi_{0p} \frac{p^{\mu_1} p^{\mu_2}}{\eta T^3} \pi_{\mu_1 \mu_2} \,, \tag{5.15}$$

which has been extensively studied in the literature, and determines the shear viscosity [103]. In the relaxation time approximation this function is related to the relaxation time

$$\chi_{0p} = -\tfrac{1}{2} \mathcal{C}_p n'_p \,. \tag{5.16}$$

One moment of this function is constrained by the shear viscosity. Indeed, from the defining relation

$$\pi^{\mu\nu} = \int_{\boldsymbol{p}} \frac{P^\mu P^\nu}{P^0} \, \delta f_{\boldsymbol{p}} \,, \tag{5.17}$$

we determine the shear viscosity

$$\eta = \frac{2}{(d-1)(d+1)T^3} \int_{\boldsymbol{p}} \frac{p^4}{E_p} \chi_{0p} \,, \tag{5.18}$$

and a constraint on $\delta f_{(2)}$

$$0 = \int_{\boldsymbol{p}} \frac{P^\mu P^\nu}{P^0} \delta f_{(2)} \,. \tag{5.19}$$

This constraint reflects the reparameterization of $\sigma^{\mu\nu}$ in the first order $\delta f_{(1)}$ with $\pi^{\mu\nu}$. For later use and comparison, we note that the enthalpy is

$$(\varepsilon + \mathcal{P}) = \frac{-1}{(d-1)T} \int_{\boldsymbol{p}} n'_p \, p^2 \,, \tag{5.20}$$

which can be obtained by comparing the stress tensor from kinetic theory for small fluid velocities (*i.e.* $u^\mu \simeq (1, \boldsymbol{v})$ with $\boldsymbol{v} \ll 1$) to ideal hydrodynamics, $T^{0i} \simeq (e + \mathcal{P}) v^i$ [112].

At second order the function $\delta f_{(2)}$ is described by two dimensionless scalar functions χ_{1p} and χ_{2p}

$$\chi_{1p} = -\tfrac{1}{2} \mathcal{C}_p \, \chi'_{0p} \,, \tag{5.21}$$

$$\chi_{2p} = \mathcal{C}_p \, \chi_{0p} \,. \tag{5.22}$$

Two moments of these scalar functions are constrained by the second order

transport coefficients $\eta\tau_\pi$ and λ_1

$$\lambda_1 + \eta\tau_\pi = \frac{8}{(d-1)(d+1)(d+3)T^6}\int_{\boldsymbol{p}} \chi_{1p}\,\frac{p^6}{E_p}\,, \tag{5.23}$$

$$\eta\tau_\pi = \frac{2}{(d-1)(d+1)T^5}\int_{\boldsymbol{p}} \chi_{2p}\,p^4\,. \tag{5.24}$$

Then the functional form of $\delta f_{(2)}$ is

$$\begin{aligned}\delta f_{(2)} =& \frac{\chi_{1p}}{\eta^2}\,\frac{p^{\mu_1}p^{\mu_2}p^{\mu_3}p^{\mu_4}}{T^6}\,\langle \pi_{\mu_1\mu_2}\pi_{\mu_3\mu_4}\rangle + \frac{\chi_{2p}}{\eta}\,\frac{p^{\mu_1}p^{\mu_2}p^{\mu_3}}{T^5}\left[(d+2)\,\langle \pi_{\mu_1\mu_2}\nabla_{\mu_3}\ln T\rangle - \langle \nabla_{\mu_1}\pi_{\mu_2\mu_3}\rangle\right] \\ &+ \frac{\xi_{1p}}{\eta^2}\,\frac{p^{\mu_2}p^{\mu_1}}{T^4}\,\langle \pi^{\lambda}{}_{\mu_2}\pi_{\mu_1\lambda}\rangle + \frac{\xi_{2p}}{\eta}\,\frac{p^{\mu_2}p^{\mu_1}}{T^3}\left[\pi_{\mu_2\mu_1} + \eta\sigma_{\mu_2\mu_1}\right] + \frac{\xi_{3p}}{\eta}\,\frac{p^{\mu_2}}{T^3}\left[\Delta_{\mu_2\lambda_2}\partial_{\lambda_1}\pi^{\lambda_1\lambda_2}\right] \\ &+ \frac{\xi_{4p}}{T^2\eta^2}\pi^2\,,\end{aligned} \tag{5.25}$$

where the four scalar functions $\xi_{1p}, \xi_{2p}, \xi_{3p}, \xi_{4p}$ are linearly related to $\chi_{0p}, \chi_{1p}, \chi_{2p}$

$$\xi_{1p} = \chi_{1p}\,\frac{4\bar{p}^2}{(d+3)} - \frac{\chi_{2p}\,\bar{E}_p}{\eta\tau_\pi}(\eta\tau_\pi + \lambda_1)\,, \tag{5.26a}$$

$$\xi_{2p} = \frac{\chi_{2p}}{T\tau_\pi}\,\bar{E}_p - \chi_{0p}\,, \tag{5.26b}$$

$$\xi_{3p} = -\chi_{2p}\frac{2\bar{p}^2}{(d+1)} + 2\chi_{0p}\frac{\eta}{s}\bar{E}_p + a_{P_*}n'_p\,, \tag{5.26c}$$

$$\xi_{4p} = \chi_{1p}\frac{2\bar{p}^4}{(d-1)(d+1)} - \chi_{2p}\frac{\bar{E}_p\bar{p}^2}{(d-1)} - \chi_{0p}\frac{\eta}{s}\bar{E}_p^2 c_s^2 + a_{E_*}n'_p\bar{E}_p\,, \tag{5.26d}$$

with $\bar{p} = |\boldsymbol{p}|/T$ and $\bar{E}_{\boldsymbol{p}} = E_{\boldsymbol{p}}/T$.

The coefficients a_{E*} and a_{p*} come from Eq. (5.9) and are adjusted so that the Landau matching conditions are satisfied. More specifically, we choose δU_* and δT_* in Eq. (5.9) so that

$$-\frac{p\cdot\delta U_*}{T} = a_{P_*}\,\frac{p^{\mu_1}}{\eta T^3}\left[\Delta_{\mu_1\lambda_2}\partial_{\lambda_1}\pi^{\lambda_1\lambda_2}\right]\,, \tag{5.27a}$$

$$-E_p\frac{\delta T_*}{T^2} = a_{E_*}\,\bar{E}_p\,\frac{\pi^2}{T^2\eta^2}\,. \tag{5.27b}$$

Then integrating over $f_{\boldsymbol{p}}(X)$ to determine the stress tensor and demanding that Eq. (5.19) (which is a restatement of the Landau matching condition),

we conclude that

$$a_{P_*} = \frac{T\eta\tau_\pi}{s} - (1+d)\left(\frac{\eta}{s}\right)^2 , \tag{5.28a}$$

$$a_{E_*} = \frac{T\eta\tau_\pi}{4s} - \frac{d+3}{d-1}\frac{T\lambda_1}{4s} + \frac{d+1}{2(d-1)}\left(\frac{\eta}{s}\right)^2 . \tag{5.28b}$$

Despite being somewhat complicated, the functional form of $\delta f_{(2)}$ is severely constrained, and is bounded by the transport coefficients η, λ_1 and $\eta\tau_\pi$ through Eqs. (5.18), (5.23), and (5.24). For a single component classical gas with the quadratic ansatz $\alpha = 0$, Eq. (5.18) shows that $\mathcal{C}_p = \frac{\eta}{s}$, and the three scalar functions which determine $\delta f_{(2)}$ can be simplified to

$$\chi_{0p} = \frac{\eta}{2s} n_p , \qquad \chi_{1p} = \frac{1}{4}\left(\frac{\eta}{s}\right)^2 n_p , \qquad \chi_{2p} = \frac{1}{2}\left(\frac{\eta}{s}\right)^2 n_p . \tag{5.29}$$

We will discuss the implementation of $\delta f_{(2)}$ in the next section.

5.2 Implementation in simulations of heavy ion collisions

In this section we will implement the $\delta f_{(2)}$ corrections in a 2+1 boost invariant hydrodynamic code. A full event-by-event simulation of heavy ion collisions with $\delta f_{(2)}$, together with a comparison to data, goes beyond the scope of this initial study. Nevertheless, the effect of $\delta f_{(2)}$ in larger simulations can be anticipated by understanding how the linear response is modified by $\delta f_{(2)}$. Indeed, the qualitative features of event-by-event hydrodynamic simulations of heavy ion collisions (including the correlations between the harmonics of different order) are reproduced by linear *and* quadratic response [70, 85, 95]. In central collisions the linear response is sufficient, and was recently used to produce one of the best estimates of the shear viscosity and its uncertainty to date [113]. We will calculate the linear response to a given deformation ϵ_n in order to estimate the influence of $\delta f_{(2)}$ on v_n.

The linear response of harmonic order n relies on the initial azimuthal deformation introduced by n-th order cumulant, in the way discussed in Section 2.2. We will focus on a typical mid-central event with the impact parameter $b = 7.45$ fm. For LHC $\sqrt{s} = 2.76$ TeV Pb-Pb collision and RHIC Au-Au $\sqrt{s} = 200$ GeV collision, the total initial entropy is adjusted by taking the constant $C_s = 28.04$ and 15.9 respectively.

After initializing the Gaussian, we evolve the system with second order hydrodynamics, Eq. (1.25) and Eq. (5.3), using a variant of the central scheme

developed previously [43, 114]. Then for a given n-th order harmonic perturbation ϵ_n we compute v_n/ϵ_n by performing the freeze-out integral at a constant temperature. This evolution requires an equation of state and specified hydrodynamic parameters at first and second order. In what follows we will consider a conformal equation of state for a single component classical gas, and a lattice motivated equation of state previously used by Romatschke and Luzum [45].

Since it is only for the conformal equation of state $p = \frac{1}{3}\epsilon$ that the analysis of Section 5.1 is strictly valid we will discuss this case first, and then discuss the necessary modifications for a lattice based equation of state. To keep the final freezeout volume of the conformal equation of state approximately equal to the much more realistic lattice based equation of state, we choose the final freezeout temperature ($T_{\rm fo} = 96\,{\rm MeV}$) so that the entropy density at freezeout $s_{\rm frz} = 1.87\,{\rm fm}^{-3}$ equals the entropy density of a hadron resonance gas at a temperature of $T = 150\,{\rm MeV}$. The relation between the temperature and energy density for the conformal equation of state is $e/T^4 = 12.2$, which is the value for a two flavor ideal quark-gluon plasma. The motivation for these choices, the parameters of the conformal equation of state, and further details about the initial conditions and freezeout we refer to our previous work – see especially Appendix B of Ref. [69].

The second order transport coefficients $\eta\tau_\pi$ and λ_1 are all constrained by the momentum dependence of the relaxation time and the shear viscosity through Eqs. (5.18), (5.23), (5.24). As discussed in Ref. [103], there are two limits for this momentum dependence which span the gamut of reasonable possibilities. In the first limit the relaxation time grows linearly with momentum, and $\alpha = 0$ in Eq. (5.7). This is known as the *quadratic ansatz*, and is most often used to simulate heavy ion collisions. In a similarly extreme limit the relaxation time is independent of momentum, and $\alpha = 1$ in Eq. (5.7). This is known as the *linear ansatz*, and this limit provides a useful foil to the more commonly adopted quadratic ansatz. Once the shear viscosity and the momentum dependence of the relaxation time are given, the collision kernel is completely specified in the relaxation time approximation, and all transport coefficients are fixed. For a linear and quadratic ansatz we record the appropriate second order transport coefficients in Table 5.1.

So far this section has detailed the initial and freezeout conditions, as well as the second order parameters which are used in the conformal equation of state. Fig. 5.2 shows the resulting elliptic flow for the quadratic and linear ansätze for a conformal equation of state including the first and second order δf. A conformal equation of state has a strong expansion, and, as a result, generally over estimates the magnitude of the δf correction. Thus the conformal analysis provides a schematic upper bound on the magnitude of the $\delta f_{(2)}$

Momentum Dependence	$\eta\tau_\pi$	λ_1
Linear Ansatz ($\alpha = 1$)	$(d+1) = 5$	$(d+1)^2/(d+3) = 25/7$
Quadratic Ansatz ($\alpha = 0$)	$(d+2) = 6$	$(d+2) = 6$

Table 5.1: Second order transport coefficients
A compilation of rescaled second order transport coefficients for a linear and quadratic ansatz in a relaxation time approximation for classical statistics [110]. All numbers in this table should be *multiplied* by $\eta^2/(e+\mathcal{P})$. In a relaxation time approximation $\lambda_2 = -2\eta\tau_\pi$ and $\lambda_3 = 0$ [110].

correction. Further discussions on these results is reserved for Section 5.3

Strictly speaking the analysis of Section 5.1 is useful only for a single component conformal gas. Nevertheless, we believe the usefulness of the analysis extends beyond this limited regime [110]. Indeed, examining the steps in the derivation one finds that only very-few non conformal terms appear at each order. For instance, if non-conformal corrections are kept in Eq. (5.12) one finds

$$\delta f^{\sigma}_{(1)-\text{non}-\text{conf}}(\boldsymbol{p}) = \mathcal{C}_p n'_p \left[\frac{p^\mu p^\nu \sigma_{\mu\nu}}{2T^3} + \left(-\frac{E^2_{\boldsymbol{p}} - |\boldsymbol{p}|^2}{3T^3} + \frac{(\frac{1}{3} - c_s^2)E^2_{\boldsymbol{p}}}{T^3} \right) \nabla_\mu u^\mu \right] , \tag{5.30}$$

which shows that non-conformal terms (the second term in Eq. (5.30)) are either suppressed by $\frac{1}{3} - c_s^2$, or are suppressed at high momentum relative to the conformal terms.

To extend our analysis to a multi-component non-conformal equation of state we have followed the simplified treatment that is used in almost all simulations of heavy ion collisions. First, we will treat all species independently

$$p^\mu \partial_\mu f^a_{\boldsymbol{p}}(x) = -\frac{T^2}{\mathcal{C}^a_p} \left[f^a_{\boldsymbol{p}}(x) - n^a(-p \cdot u_*(x)/T_*(x)) \right] , \tag{5.31}$$

where $a = \pi, K, \rho, \ldots$ is a species label[1]. We will also adopt the quadratic ansatz $\alpha = 0$, so that $\mathcal{C}^a_p$ is independent of momentum. Then for every species

[1]There have been several efforts to go beyond this extreme species independent approximation [103, 115].

we define the partial entropy and shear viscosity as in Eqs. 5.18 and 5.20

$$\eta_a = \frac{-\mathcal{C}_p^a}{(d-1)(d+1)} \left[\frac{g_a}{T^3} \int_{\boldsymbol{p}} n_p^{a\prime} \frac{p^4}{E_p} \right] , \tag{5.32a}$$

$$s_a = \frac{-1}{(d-1)} \left[\frac{g_a}{T^2} \int_{\boldsymbol{p}} n_p^{a\prime} p^2 \right] , \tag{5.32b}$$

where g_a is the spin-isospin degeneracy factor. The full shear viscosity and entropy density is a sum of the partial results, $\eta = \sum_a \eta_a$ and $s = \sum_a s_a$. We require that η_a/s_a is equal to η/s for each species, and thus the relaxation time parameter $\mathcal{C}_p^a$ is, in principle, different for each species. However, for a classical gas the two integrals in square brackets are equal upon integrating by parts, and thus $\mathcal{C}_p^a = \eta_a/s_a = \eta/s$ is independent of the mass and species label. For fermi-dirac and bose statistics these integrals are very nearly equal (to 4% accuracy) for all values of the mass, and $\mathcal{C}_{\boldsymbol{p}}^a$ is approximately equal to η/s for all species independent of mass and statistics.

Now that the relaxation time parameter $\mathcal{C}_p^a$ is fixed for each species, the corresponding second order δf for each species is found by appending a species label, $n_p \to n_p^a$ and $\mathcal{C}_p \to \mathcal{C}_p^a$, to previous results. For a multi-component gas with a quadratic ansatz we find

$$\eta\tau_\pi + \lambda_1 = \sum_a (\mathcal{C}_p^a)^2 \left[\frac{2g_a}{(d-1)(d+1)(d+3)T^6} \int_{\boldsymbol{p}} n_p^{a\prime\prime} \frac{p^6}{E_p} \right] , \tag{5.33a}$$

$$\eta\tau_\pi = \sum_a (\mathcal{C}_p^a)^2 \left[\frac{-g_a}{(d-1)(d+1)T^5} \int_{\boldsymbol{p}} n_p^{a\prime} p^4 \right] . \tag{5.33b}$$

For classical statistics $\mathcal{C}_p^a = \eta/s$, and integrating the first integral in square brackets by parts yields a simple relation noted previously [110]

$$\lambda_1 = \eta\tau_\pi \qquad (\text{for } \alpha = 0) . \tag{5.34}$$

The remaining thermodynamic integrals are most easily done numerically; summing over all hadronic species with mass less than 1.5 GeV we find

$$\lambda_1 = \eta\tau_\pi = \frac{\eta^2}{(\varepsilon + \mathcal{P})} 8.9 . \tag{5.35}$$

Thus, $T\tau_\pi/(\eta/s) = 8.9$ would seem to be the most consistent value for the 2nd order transport coefficients during the hydrodynamic evolution of the hadronic phase. However, this value for $T\tau_\pi$ is somewhat too large to be used comfortably in the simulation (see for example, [44]). Further, $T\tau_\pi$ decreases as

temperature increases, and $T\tau_\pi/(\eta/s) \simeq 5$ is good approximation in the QGP phase [110]. We have therefore taken $\lambda_1 = \eta\tau_\pi = 5\eta^2/(\varepsilon + \mathcal{P})$ throughout the evolution. This means that there is a small inconsistency between the second order δf at freezeout, and the second order parameters used to simulate the bulk of the hydrodynamic evolution. Similar inconsistencies are found in all attempts to consistently couple hydrodynamic codes with hadronic cascades [116].

To summarize, in this section we have specified precisely the initial conditions, the equation of state, the transport coefficients at first and second order, and the first and second order corrections to the distribution functions. We have used this setup to compute the linear response coefficients v_n/ϵ_n for RHIC and LHC initial conditions for the first six harmonics. Our results are displayed in Fig. 5.3 and Fig. 5.4. We will discuss the physics of these curves in the next section.

5.3 Discussion

This work computed the second order viscous correction to the thermal distribution function, $\delta f_{(2)}$, and used this result to estimate the effect of second order corrections on the harmonic spectrum. Our principle results are shown in Fig. 5.2 for a conformal equation of state, and Fig. 5.3, and Fig. 5.4 for a lattice based equation of state. First, examine the v_2 curves for the conformal EOS shown in Fig. 5.2. The most important remark is that even for a conformal equation of state, where the expansion is most violent, the derivative expansion converges acceptably for $p_T \lesssim 1.5\,\text{GeV}$, *i.e.* the second order correction is small compared to the first order correction. Not surprisingly, when a linear ansatz is used for δf (rather than the more popular quadratic ansatz) the convergence of the derivative expansion is improved at high p_T. Typically in hydrodynamic simulations of heavy ion collisions, the strictly first order $\delta f^\sigma_{(1)}$ is replaced by the $\delta f_{(1)}$ which incorporates some, but not all, second order terms[2]. Examining Fig. 5.2, and also Fig. 5.3 and Fig. 5.4, we see that, while the sign of the second order correction is correctly reproduced by this incomplete treatment, the magnitude of the correction is generally significantly underestimated, and the p_T dependence of the second order correction is qualitatively wrong.

Most of these observations remain true for the more realistic lattice equation of state shown in Fig. 5.3 and Fig. 5.4. Generally, second order corrections are quite small for the first three harmonics, v_1 to v_3, and become increasingly

[2]As discussed above, $\delta f_{(1)}$ uses $\pi^{\mu\nu}$ in place of $-\eta\sigma^{\mu\nu}$ when calculating the first order correction.

important as the harmonic number increases. Indeed, for v_6 at RHIC and the LHC, the second order viscous correction is of order one, and the hydrodynamic estimate can no longer be trusted. It is also instructive to note that the sign of the second order viscous correction for $p_T \lesssim 1.5\,\mathrm{GeV}$ is positive, *i.e.* second order corrections bring the $v_n(p_T)$ curves closer to the ideal results. Generally, when the first order correction, becomes so large as to make $v_n(p_T)$ negative at first order, the second order correction conspires to keep v_n positive. When constraining η/s with hydrodynamic simulations, the second order corrections are most important for v_4 and v_5. Indeed, at RHIC these corrections are quite important for v_5 even in central collisions.

For a practical perspective, using $\delta f_{(2)}$ in a hydrodynamic simulation is not particularly more difficult than using $\delta f_{(1)}$, and Eq. 5.13 can be readily implemented in most hydro codes. The functional form of $\delta f_{(2)}$ and its magnitude is about as well constrained as $\delta f_{(1)}$, and consistency with the second order hydrodynamic evolution would seem to mandate its use. At very least $\delta f_{(2)}$ should be taken into consideration when estimating the uncertainty in the η/s extracted from heavy ion collisions. Finally, when trying to use hydrodynamics in very small systems such as proton-nucleus collisions at RHIC and the LHC [40, 117–122], second order corrections to δf should be used in order to monitor the convergence of the gradient expansion.

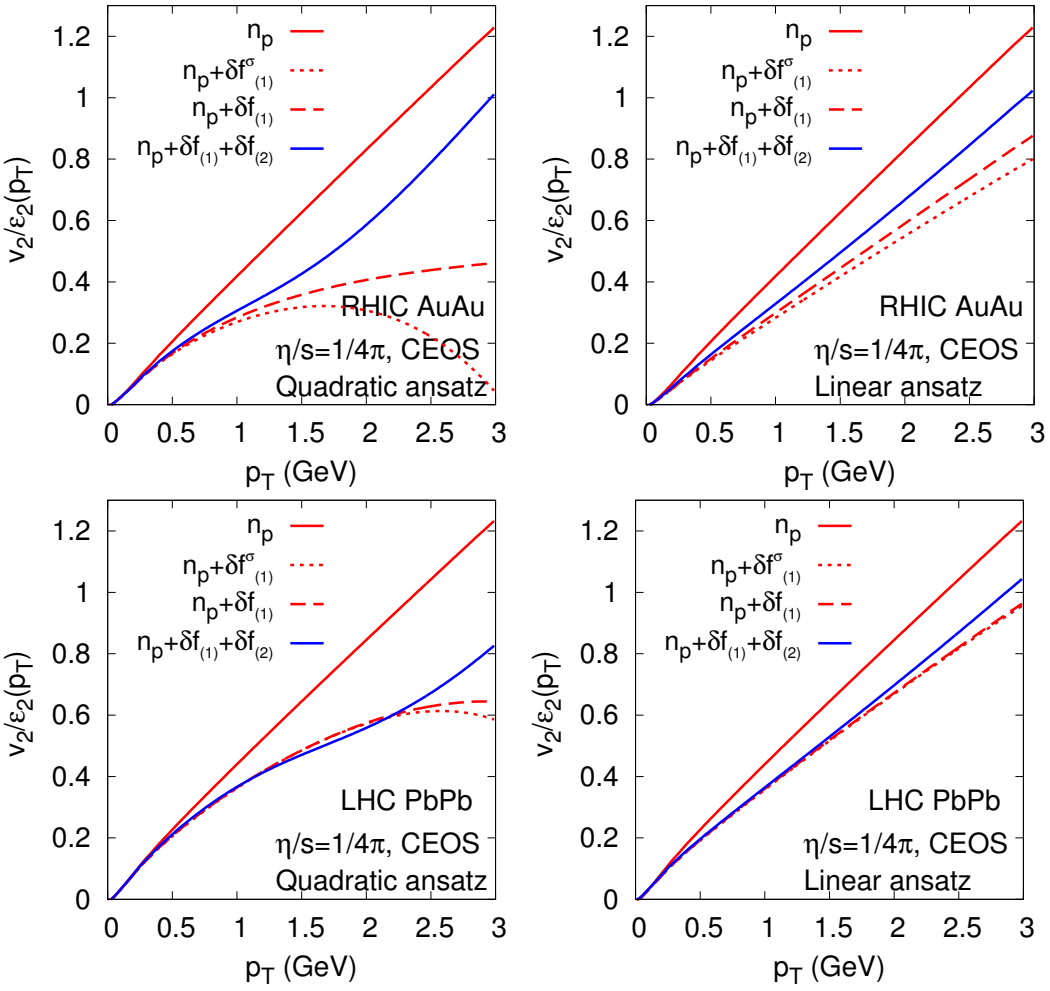

Figure 5.2: Differential $v_2(p_T)/\epsilon_2$ at RHIC and LHC, with CEOS and LEOS Differential $v_2(p_T)/\epsilon_2$ for RHIC and LHC initial conditions, for a linear and quadratic ansatz, and a conformal equation equation of state (CEOS). The n_p curves shows the flow from second order hydrodynamics without the viscous correction to the distribution function; $\delta f_{(1)}$ and $\delta f_{(1)} + \delta f_{(2)}$ show the flow with the viscous correction at first and second order; and finally, the $\delta f^{\sigma}_{(1)}$ result uses $-\eta\sigma^{\mu\nu}$ instead of $\pi^{\mu\nu}$ in the first order result (see Eq. (5.12)). The freezeout temperature is chosen so that the freezeout entropy density of the conformal gas equals that of a hadronic resonance gas at a temperature of $T = 150\,\mathrm{MeV}$.

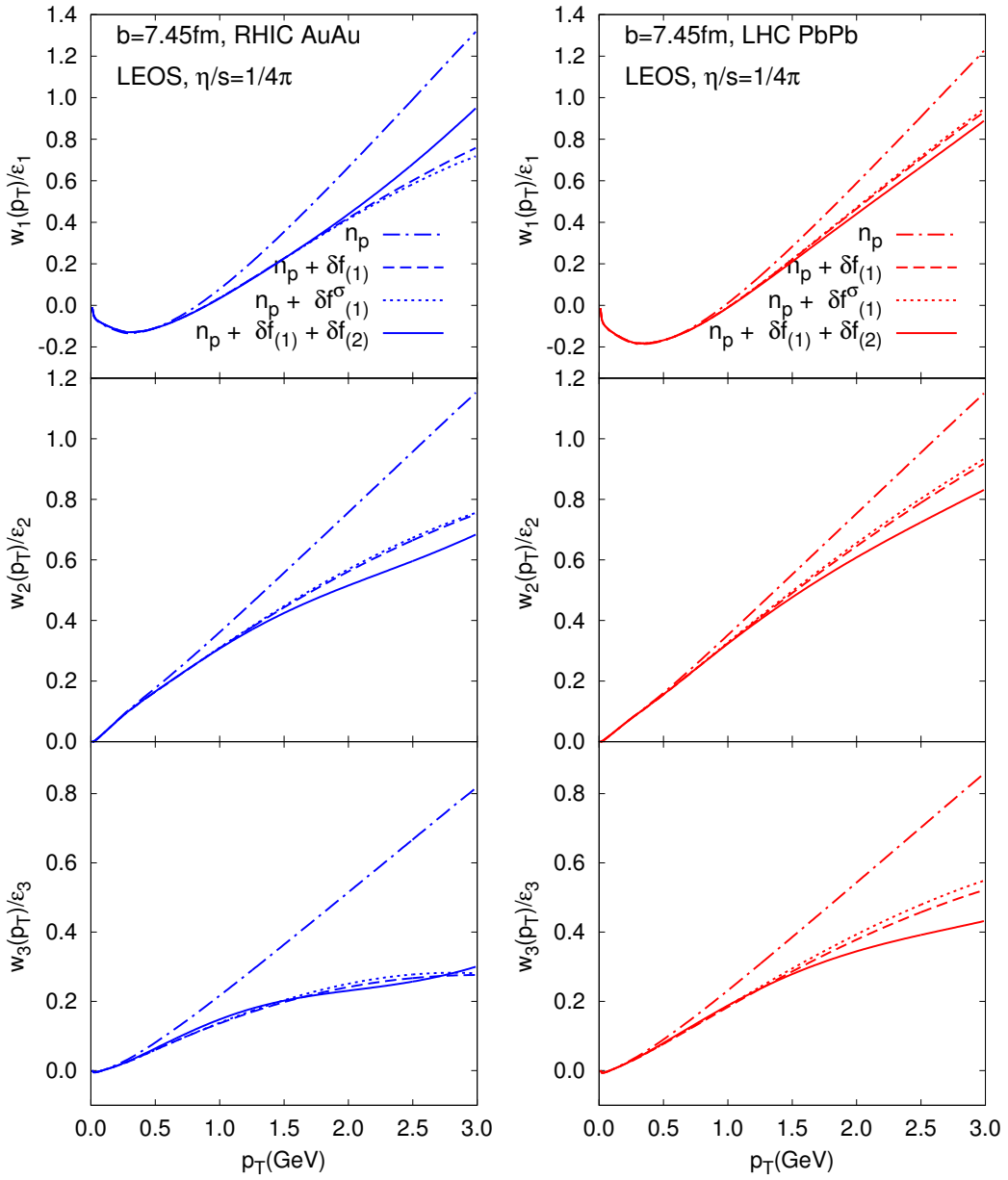

Figure 5.3: Differential v_n/ϵ_n at RHIC and LHC

Differential v_n/ϵ_n from various viscous hydrodynamic simulations at $b = 7.45\,\mathrm{fm}$ for RHIC and LHC initial conditions, and a lattice equation of state (LEOS) with $T_{\mathrm{fo}} = 150\,\mathrm{MeV}$. Here the n_p curve shows the flow from second order hydrodynamics without the viscous correction to the distribution function; $\delta f_{(1)}$ and $\delta f_{(1)} + \delta f_{(2)}$ show the flow with the viscous correction at first and second order respectively; and finally, the $\delta f^{\sigma}_{(1)}$ curve uses $-\eta\sigma^{\mu\nu}$ instead of $\pi^{\mu\nu}$ in the first order viscous correction (see Eq. (5.12)).

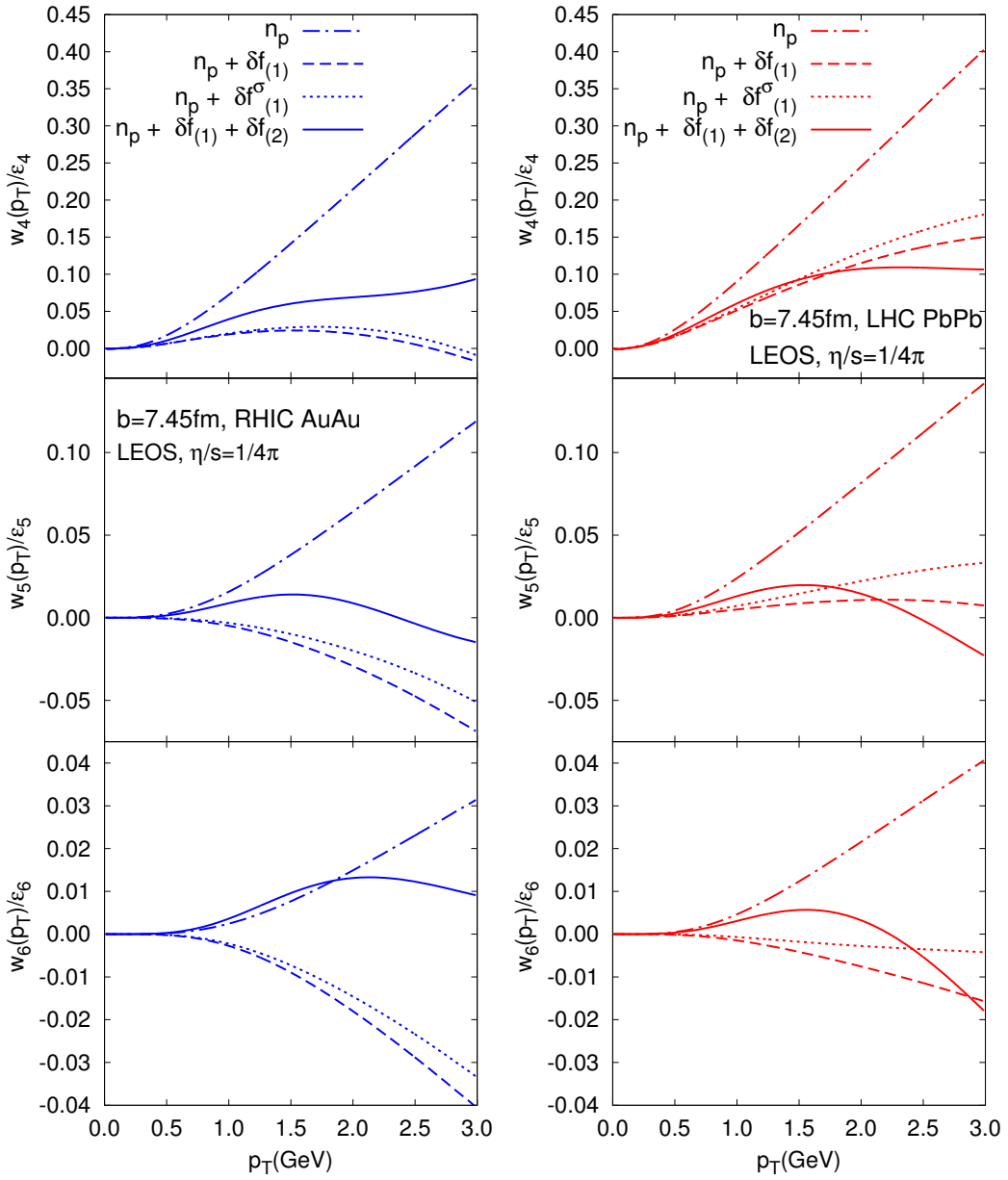

Figure 5.4: Differential v_n/ϵ_n at RHIC and LHC

Differential v_n/ϵ_n from various viscous hydrodynamic simulations at $b = 7.45\,\mathrm{fm}$ for RHIC and LHC initial conditions, and a lattice equation of state (LEOS) with $T_{\mathrm{fo}} = 150\,\mathrm{MeV}$. Here the n_p curve shows the flow from second order hydrodynamics without the viscous correction to the distribution function; $\delta f_{(1)}$ and $\delta f_{(1)} + \delta f_{(2)}$ show the flow with the viscous correction at first and second order respectively; and finally, the $\delta f^{\sigma}_{(1)}$ curve uses $-\eta\sigma^{\mu\nu}$ instead of $\pi^{\mu\nu}$ in the first order viscous correction (see Eq. (5.12)).

Chapter 6

Conclusions and outlook

In this dissertation work, we have developed a linear and nonlinear response formalism to describe the correlations observed in heavy ion collisions. This serves as an alternative to event-by-event calculations for the observed harmonic flows and plane correlations. Accordingly, with respect to the initial state fluctuations in heavy-ion collisions, several improvements for the hydrodynamic description of the medium expansion have been discussed.

First of all, we introduced the cumulant expansion formalism to analyze the fluctuating initial state. Regarding initial state fluctuations as perturbations on top of a smooth background, the azimuthal anisotropies are defined in terms of a series of cumulants. Cumulant defined initial anisotropies are distinguished from the traditionally used moments definitions in several ways. First, for each harmonic order n, we found that there exists an extra index that naturally takes into account of the fluctuations along the radial direction. Second, in the cumulant definition for the higher order azimuthal deformations a subtraction of nonlinearities is implied. Although the cumulant definition is more complex, the initial state anisotropies are characterized more systematically. In particular, we described the dipole asymmetry, a rapidity-even asymmetry in the initial state of heavy-ion collisions on an event-by-event basis. From Monte Carlo simulations of the initial state, we found that the magnitude of the dipole asymmetry is relatively small compared to the other eccentricities. However, the dipole asymmetry induces a noticeable rapidity-even dipole flow v_1, whose unique p_T dependence has been confirmed in experiments from both RHIC Au-Au collisions and LHC Pb-Pb collisions.

In addition, based on the cumulant formalism, we noticed the significance of initial state participant plane correlations. For example, the $\langle\langle \cos 2(\Phi_1 - \Phi_2)\rangle\rangle$ provides a background for the observed $\langle \cos(\phi_a + \phi_b - 2\Psi_R)\rangle$ of inclusive two-particle correlations. Since these initial state participant plane correlations are dominated by the initial geometry, studying the corresponding event plane

correlations is expected to be the best way to understand these initial geometric effects. Therefore, we proposed signatures in the observables, such as the $\langle\cos(\phi_a-3\phi_b+2\Psi_R)\rangle$ to test the initial anti-correlation $\langle\langle\cos(\Phi_1-3\Phi_3+2\Phi_2)\rangle\rangle$. We also examined a number of two-plane and three-plane correlations, with respect to the recent ATLAS measurement. From Monte Carlo simulations, these initial plane correlations are found different with the cumulant based definitions or the moment based definitions. Nevertheless, the disagreement of the initial simulations with experimental data suggest the insufficiency of the linear flow response of medium expansion, which inspired us the work on nonlinear flow response formalism.

We investigated the linear flow generation, with the cumulant description of initial state anisotropy. We found the normal process of flow development, with respect to the fluctuating initial state, that all of the initial spatial eccentricities are transformed into momentum space in a similar manner. And the linearly generated harmonic flows rise linearly in p_T in the large transverse momentum region, from ideal hydrodynamic calculations. The viscous effects on the linear flow response are found crucial for higher order harmonics, as we expected. The viscous damping follows a semi-quantitative pattern that the damping rate is proportional to the square of harmonic order. And as long as higher order harmonic flow is not involved in the problem, the predicted results are consistent with experimental observations to a large extent. For example, even with ideal hydrodynamics and conformal EoS for a massless gas, the predicted $V_{3\Delta}/V_{2\Delta}$ is consistent with experimental data on this ratio.

However, for higher order harmonic flow we need to go beyond the leading order of flow response. The nonlinear flow response formalism is formulated in analogous to the linear flow response, with nonlinear flow response coefficients proposed to relate nonlinearly coupled initial anisotropies and the nonlinearly generated flow. We systematically investigated some typical nonlinear flow response coefficients, as a function of transverse momentum, centrality and the shear viscosity to entropy ratio. The nonlinear response gives $v_n(p_T)$ a characteristic quadatic dependence on p_T for large p_T. Further the nonlinear flow response is found to significantly affect the harmonic flow for large harmonic order, large centrality, and large input η/s. These properties of nonlinear flow generation play a crucial role in our further predictions, in particular the final state event plane correlations.

The ATLAS collaboration systematically measured the two-plane and three-plane event plane correlations, using the so-called event-plane method. With our linear and nonlinear flow response formalism, the single-shot hydrodynamic framework reproduced most of the observed correlation patterns. In particular, by separately calculating the correlation in the 'linear limit' and

the 'nonlinear limit', we can give analytical interpretation for the formation of these correlations, and understand the dependence of these correlations on centrality, and also η/s. Since in non-central collisions viscous effects are important, the flow generation is dominated by the nonlinear response, and the observed event plane correlations consequently approaches the 'nonlinear limit'. Since the analysis on event plane correlations relies on the medium property, the knowledge of their dependence on η/s is useful for future endeavors of extracting of the transport coefficients of the QCD medium.

Finally, we developed the consistent description of freeze-out with second viscous corrections to the phase space distribution function. It is well known that second order viscous hydrodynamic equations of motion are indispensable in applications to avoid causality problem, and to take into account dissipations in the expanding medium. However, the widely used freeze-out phase space distribution function is only self-consistent to first order in viscous corrections. This inconsistency theoretical framework used to describe heavy-ion collisions needs to be remedied. Relying on the kinetic theory, in which hydrodynamics at freeze-out is constrained with certain forms, we solve the Boltzmann equation in a relaxation time approximation, and determine the second order viscous correction, $\delta f_{(2)}$. Although the theory is strict in a conformal system, we applied the obtained $\delta f_{(2)}$ for more realistic calculations with lattice EoS. For RHIC and LHC energies, the effects of $\delta f_{(2)}$ is seen as corrections to the differential harmonic flow, and are important for higher harmonic flow at high p_T.

This research can be extended in several directions. First, the initial anisotropies have been studied in the transverse plane, with cumulant expansion. This should be generalized to a full 3+1 dimensional system. The extended version of the cumulant expansion, and the characterization of fluctuations in such 3+1 dimensional systems is briefed in Appendix B. In the longitudinal correlations of harmonic flows can be expected. For example, the new cumulant term $\mathcal{W}_{2,2,1}$ implies a rapidity-odd elliptic flow, which should be studied and measured.

Second, the second order viscous corrections are expected to be more significant for systems with stronger dissipative effects. In particular systems with much smaller system size, such as the recent pA collision at LHC. Considering the higher sensitivity of viscous hydrodynamic calculations with $\delta f_{(2)}$, the applicability of hydrodynamics can be examined in these small systems.

Appendix A

Notations and conventions

We take the natural units throughout this thesis work, so that $\hbar = c = 1$ is ignored in these formulas unless necessary. As a result, the unit of energy, mass and momentum are taken to be GeV, while length and time are characterized in fm.

The matrix $\eta^{\mu\nu} = (-1, 1, 1, 1)$ is used for the general coordinate systme (t, x, y, z) with the Greek indices running over $0, 1, 2, 3$. When Bjorken boost invariance is taken into account, it is convenient to work in the coordinate system (τ, x, y, η_s), so that the η_s dependence of the system is trivial and hydrodynamics is simplified accordingly to a 2+1 dimensional problem. Note the matrix in this coordinate system is not trivial. Four-vectors, such as flow four-velocity u^μ, are denoted by the ordinary type of lower case letters, while the boldface type is used for three-vectors, *e. g.* $\boldsymbol{x}$ and $\boldsymbol{p}$.

Brackets around a scalar are used in this work to denote several different types of averages. The script brackets $\{\ldots\} = \int \rho(\tau_0, \boldsymbol{x}_\perp) \ldots$ is defined with respect to the initial normalized entropy density, reflecting the geometric information of the initial state. Single angle brackets $\langle \ldots \rangle$ is the average regarding the final state (multi-)particle spectrum. Double angle brackets $\langle\langle \ldots \rangle\rangle$ notates results from the event average.

Brackets around indices of a tensor structure, especially seen in Chapter 5, are introduced for the convenience of theoretical derivations, with particular meanings. For example, with the help of the projection operator, $\Delta^{\mu\nu} = u^\mu u^\nu + \eta^{\mu\nu}$,

$$\langle A^{\mu\nu} \rangle = \frac{1}{2} \Delta^\mu_{\ \rho} \Delta^\nu_{\ \sigma} \left(A^{\rho\sigma} + A^{\sigma\rho} \right) - \frac{1}{(d-1)} \Delta^{\mu\nu} \Delta_{\rho\sigma} A^{\rho\sigma} \,, \tag{A.1}$$

is constructed as symmetric-traceless and orthogonal to u^μ, *i. e.*,

$$\langle A^{\mu\nu}\rangle = \langle A^{\nu\mu}\rangle, \quad \langle A^{\mu\nu}\rangle \Delta_{\mu\nu} = 0, \quad \langle A^{\mu\nu}\rangle u_\mu = 0\,. \tag{A.2}$$

Such tensors transform irreducibly under rotation in the local rest frame. If without imposing the traceless condition, we have

$$\{A^{\mu\nu}\}_{\rm sym} = \frac{1}{2}\Delta^\mu_{\ \rho}\Delta^\nu_{\ \sigma}\left(A^{\rho\sigma} + A^{\sigma\rho}\right) = \Delta^\mu_{\ \rho}\Delta^\nu_{\ \sigma}(A^{\mu\nu})\,, \tag{A.3}$$

denoting a symmetric tensor structure that is orthogonal to u^μ. In Eq. (A.3) the bracketed $(A^{\mu\nu})$ is just the general symmetric tensor. A more elaborate example using $\sigma_{\mu\nu} = 2\langle\nabla_\mu u_\nu\rangle$ which appears in Appendix C is

$$\begin{aligned}\{\sigma_{\mu_1\mu_2}\sigma_{\mu_3\mu_4}\}_{\rm sym} = \langle\sigma_{\mu_1\mu_2}\sigma_{\mu_3\mu_4}\rangle &+ \frac{4}{d+3}\left\{\Delta_{\mu_1\mu_2}\left\langle\sigma^\lambda_{\ \mu_3}\sigma_{\mu_4\lambda}\right\rangle\right\}_{\rm sym} \\ &+ \frac{2}{(d-1)(d+1)}\left\{\Delta_{\mu_1\mu_2}\Delta_{\mu_3\mu_4}\right\}_{\rm sym}\sigma^2\,,\end{aligned} \tag{A.4}$$

where the symmetrized spatial tensor is denoted with curly brackets:

$$\{\sigma_{\mu_1\mu_2}\sigma_{\mu_3\mu_4}\}_{\rm sym} = \frac{1}{3}\left[\sigma_{\mu_1\mu_2}\sigma_{\mu_3\mu_4} + \sigma_{\mu_1\mu_3}\sigma_{\mu_3\mu_4} + \sigma_{\mu_1\mu_4}\sigma_{\mu_2\mu_3}\right]\,. \tag{A.5}$$

These structures defined here are helpful for the decomposition of the tensors in $\delta f_{(2)}$, which is detailed in Appendix C.

The equilibrium distribution function is $n_{\boldsymbol{p}} \equiv n(-P\cdot u(x)/T(x))$ where $n(z) = 1/(e^z \mp 1)$, and $f_{\boldsymbol{p}}(x)$ denotes the full non-equilibrium distribution. The rest frame integrals are abbreviated $\int_{\boldsymbol{p}} \equiv \int \mathrm{d}^{d-1}p/(2\pi)^{d-1}$, with $d = 4$ denotes the space-time dimension. Primes (such as n'_p) denote derivatives with respect to $-p\cdot u/T$, so that $n'_{\boldsymbol{p}} = -n_{\boldsymbol{p}}(1 \pm n_{\boldsymbol{p}})$. The energy and squared three momentum in the rest frame are, $E_{\boldsymbol{p}} = -p\cdot u$ and $|\boldsymbol{p}|^2 = p^\mu p^\nu \Delta_{\mu\nu}$, respectively.

Appendix B

3-dimensional cumulant analysis

Due to the approximated Bjorken boost invariance of the medium system in heavy-ion collisions, it is convenient to work in the coordinate system $(\tau, r, \phi_r, \eta_s)$. Note the space-time rapidity is denoted with η_s, however, we will drop the 's' in the sub-indices when confusion can not arise. For a given 3-dimensional distribution $\rho(\boldsymbol{x}_\perp, \eta_s)$, we extend the aforementioned cumulant expansion,

$$\rho(\tau_0, \boldsymbol{x}_\perp, \eta_s) = \int d^2\boldsymbol{k}_\perp dk_\eta e^{i(\boldsymbol{k}_\perp\cdot\boldsymbol{x}_\perp + k_\eta\eta_s)}\hat{\rho}(\tau_0, \boldsymbol{k}_\perp, k_\eta) \tag{B.1}$$

$$\hat{\rho}(\tau_0, \boldsymbol{k}_\perp, k_\eta) = \int d^2\boldsymbol{x}_\perp d\eta_s e^{-i(\boldsymbol{k}_\perp\cdot\boldsymbol{x}_\perp + k_\eta\eta_s)}\rho(\tau_0, \boldsymbol{x}_\perp, \eta_s). \tag{B.2}$$

The exponential factor now becomes

$$e^{-i(\boldsymbol{k}_\perp\cdot\boldsymbol{x}_\perp + k_\eta\eta_s)} = \left[\sum_{n=0}^{\infty}\sum_{l=0}^{n}\frac{(-i)^n C_n^l}{n!2^n}(\bar{k}\bar{r}^*)^l(\bar{k}^*\bar{r})^{n-l}\right] e^{-ik_\eta\eta_s}, \tag{B.3}$$

so to the lowest order in k_η, we obtain a trivial extension of the 2-dimensional transverse plane case Eq. (2.8), while the average is now defined as

$$\{\bar{r}^n(\bar{r}^*)^{n-l}\} = \int d^2\boldsymbol{x}_\perp d\eta_s \bar{r}^n(\bar{r}^*)^{n-l}\rho(\tau_0, \boldsymbol{x}_\perp, \eta_s) = \int d\eta\{\bar{r}^n(\bar{r}^*)^{n-l}\}_\perp(\eta_s) \tag{B.4}$$

To be consistent, we impose

$$\{\bar{r}\}_\perp(\eta = 0) = \{\bar{r}^*\}_\perp(\eta = 0) = 0\,, \tag{B.5}$$

so that the system center is not changed from the 2-dimensional case to the 3-dimensional system. To the first order in k_η, we have

$$\hat{\rho}(\tau_0, \boldsymbol{k}_\perp, k_\eta) = \hat{\rho}(\tau_0, \boldsymbol{k}_\perp, k_\eta = 0) + k_\eta \sum_{n=0}^{\infty} \sum_{l=0}^{n} \frac{(-i)^{n+1} C_n^l}{n! 2^n} \bar{k}^l (\bar{k}^*)^{n-l} \{(\bar{r}^*)^l r^{n-l} \eta_s\} + O(k_\eta^2) \tag{B.6}$$

The expansion in k_η reflects the similar argument of long-wavelength expansion in the longitudinal direction. Generally we have

$$\hat{\rho}(\tau_0, \boldsymbol{k}_\perp, k_\eta) = \sum_{j=0}^{\infty} \sum_{n=0}^{\infty} \sum_{l=0}^{n} \frac{(-i)^{n+j} C_n^l}{n! 2^n} \bar{k}^l (\bar{k}^*)^{n-l} k_\eta^j \{(\bar{r}^*)^l r^{n-l} \eta_s^j\} \,. \tag{B.7}$$

If we adhere to the strategy and conventions used before, the 3-dimensional cumulant $\mathcal{W}(\boldsymbol{k}_\perp, k_\eta)$ can be introduced,

$$\begin{aligned} \mathcal{W}(\boldsymbol{k}_\perp, k_\eta) &= \sum_{n,m,j} (-i)^{n+j} \mathcal{W}_{n,m,j}(\boldsymbol{k}_\perp, k_\eta) = \ln \rho(\tau_0, \boldsymbol{k}_\perp, k_\eta) \\ &= \underbrace{\hat{W}(\boldsymbol{k}_\perp)}_{\sum_{n,m} \mathcal{W}_{n,m,j=0}} \underbrace{-k_\eta \sum_{n=0}^{\infty} \sum_{l=0}^{n} \frac{(-i)^{n+1} C_n^l}{n! 2^n} \bar{k}^l (\bar{k}^*)^{n-l} \{(\bar{r}^*)^l r^{n-l} \eta_s\} e^{-\hat{W}(\boldsymbol{k}_\perp)}}_{\sum_{n,m} \mathcal{W}_{n,m,j=1}} + O(k_\eta^2). \end{aligned} \tag{B.8}$$

The 3-dimensional cumulant $\mathcal{W}_{n,m,j}$ is used to characterize the deformations of the whole 3-dimensional system. We note the non-trivial mode mixing of deformations between the longitudinal direction and transverse direction, due to the non-zero value of $\mathcal{W}_{n,m,j\neq 0}$. The lowest order cumulants, *i.e.*, those with $n \leq 3$ and $j = 1$ will generate the dominant initial state mixing between the longitudinal deformation and the azimuthal anisotropies. For instance, we find the rapidity-odd correlation of ϵ_1, $\epsilon_{3,1}$ $\epsilon_{2,2}$ and $\epsilon_{3,3}$, through

$$\mathcal{W}_{1,1,1} = -\frac{1}{2} k_\eta \bar{k} \{\bar{r}^* \eta_s\} + c.c. \tag{B.9}$$

$$\mathcal{W}_{3,1,1} = -\frac{1}{3! 2^3} k_\eta \bar{k} (\bar{k}^*)^2 \left[\{\bar{r}^* \bar{r}^2 \eta_s\} - 3\{\bar{r}^2\}\{\bar{r}^* \eta_s\}\right] + c.c. \tag{B.10}$$

$$\mathcal{W}_{2,2,1} = -\frac{1}{2! 2^2} k_\eta (\bar{k}^*)^2 \{\bar{r}^2 \eta_s\} + c.c. \tag{B.11}$$

$$\mathcal{W}_{3,3,1} = -\frac{1}{3! 2^3} k_\eta (\bar{k}^*)^3 \left[\{\bar{r}^3 \eta_s\} - 3\{\bar{r} \eta_s\}\{\bar{r}^2\}\right] + c.c. \tag{B.12}$$

Appendix C

Tensor decomposition of $\delta f_{(2)}$

The goal of this appendix is to compute $\delta f_{(2)}$ and to record how this results transforms under rotations in the local rest frame. Our starting point is Eqs. (5.13) which we rewrite in terms of irreducible tensors under rotations in the local rest frame.

A systematic strategy decomposes all derivatives into temporal and spatial components

$$\partial_\mu = -u_\mu D + \nabla_\mu \,, \tag{C.1}$$

where the spatial component ∇_μ is orthogonal to u_μ. When differentiating a quantity that is already first order (*i.e.* $P^\mu \partial_\mu \delta f^\sigma_{(1)}$), we can use the lowest order conformal equations of motion to rewrite time derivatives in terms of spatial derivatives

$$D\ln T = -\, c_s^2 \nabla \cdot u \,, \tag{C.2}$$

$$D u_\mu = -\, \nabla_\mu \ln T \,, \tag{C.3}$$

where $c_s^2 = (\varepsilon + \mathcal{P})/(T c_v) = 1/(d-1)$. Finally, the resulting tensors can be decomposed into symmetric, traceless, and spatial tensors as in Eq. (A.4), which transform irreducibly under rotations in the local rest frame. To illustrate the procedure, we record the decomposition of $D\sigma_{\alpha\beta}$

$$D\sigma_{\alpha\beta} = D(\sigma^{\mu\nu}\Delta_{\mu\alpha}\Delta_{\nu\beta}) = \Delta_{\mu\alpha}\Delta_{\nu\beta} D\sigma^{\mu\nu} + \sigma^{\mu\nu} D(\Delta_{\mu\alpha}\Delta_{\nu\beta}) \,, \tag{C.4}$$

$$= \langle D\sigma_{\alpha\beta} \rangle - (\sigma^\mu_{\ \beta} u_\alpha \nabla_\mu \ln T + u_\beta \sigma^\nu_{\ \alpha} \nabla_\nu \ln T) \,. \tag{C.5}$$

Similarly, the symmetrized spatial tensor $\{\nabla_\mu \sigma_{\alpha\beta}\}_{\rm sym}$ that arises when differ-

entiating $\delta f^{\sigma}_{(1)}$ is decomposed as

$$\{\nabla_\mu \sigma_{\alpha\beta}\}_{\rm sym} = \langle \nabla_\mu \sigma_{\alpha\beta}\rangle + \Big\{ \frac{2}{d+1}\Delta_{\mu\alpha}\nabla_\gamma \sigma^{\gamma}_{\ \beta} + u_\alpha \left\langle \sigma^{\rho}_{\ \beta}\sigma_{\mu\rho}\right\rangle + u_\alpha \frac{\Delta_{\mu\beta}}{d-1}\sigma^2 + 2u_\alpha \left\langle \sigma^{\rho}_{\ \beta}\Omega_{\mu\rho}\right\rangle + 2u_\alpha \frac{\sigma_{\mu\beta}}{d-1}\nabla\cdot u\Big\}_{\rm sym}\,, \quad \text{(C.6)}$$

where we have used

$$\nabla_\mu u_\rho = \frac{1}{2}\sigma_{\mu\rho} + \Omega_{\mu\rho} + \frac{\Delta_{\mu\rho}}{d-1}\nabla\cdot u\,. \quad \text{(C.7)}$$

Finally, we note that

$$\left\langle \partial_\lambda \pi^{\lambda}_{\ \mu}\right\rangle = \Delta_{\mu\lambda_2}\,\partial_{\lambda_1}\pi^{\lambda_1\lambda_2} = -\eta\left[(d-2)\left\langle \sigma_{\mu\lambda}\nabla^\lambda \ln T\right\rangle + \left\langle \nabla_\lambda \sigma^{\lambda}_{\ \mu}\right\rangle\right]\,, \quad \text{(C.8)}$$

where we have used the first order expression, $\pi^{\mu\nu} = -\eta\sigma^{\mu\nu}$, the conformal temperature dependence of $\eta \propto T^{d-1}$, and the lowest order equations of motion.

With this automated set of steps, we start with Eq. (5.13) and place $\delta f^{\sigma}_{(2)}$ into its canonical form

$$\begin{aligned}\delta f^{\sigma}_{(2)} =& \chi_{1p}\frac{p^{\mu_1}p^{\mu_2}p^{\mu_3}p^{\mu_4}}{T^6}\left\langle \sigma_{\mu_1\mu_2}\sigma_{\mu_3\mu_4}\right\rangle + \chi_{2p}\frac{p^{\mu_1}p^{\mu_2}p^{\mu_3}}{T^5}\left[\left\langle \nabla_{\mu_1}\sigma_{\mu_2\mu_3}\right\rangle - 3\left\langle \sigma_{\mu_1\mu_2}\nabla_{\mu_3}\ln T\right\rangle\right] \\ &+ \left(\chi_{1p}\frac{4\bar{p}^2}{d+3} - \chi_{2p}\bar{E}_p\right)\frac{p^{\mu_2}p^{\mu_1}}{T^4}\left\langle \sigma^{\lambda}_{\ \mu_2}\sigma_{\mu_1\lambda}\right\rangle \\ &+ \chi_{2p}\bar{E}_p\frac{p^{\mu_2}p^{\mu_1}}{T^4}\Big[\left\langle D\sigma_{\mu_2\mu_1}\right\rangle + \frac{\sigma_{\mu_2\mu_1}}{d-1}\nabla\cdot u - 2\left\langle \sigma^{\lambda}_{\ \mu_2}\Omega_{\mu_1\lambda}\right\rangle\Big] \\ &+ \xi_{3p}\frac{p^{\mu_2}}{T^3}\left[-\left\langle \nabla_\lambda \sigma^{\lambda}_{\ \mu_2}\right\rangle - (d-2)\left\langle \sigma_{\mu_2\lambda}\nabla^\lambda \ln T\right\rangle\right] + \frac{\xi_{4p}}{T^2}\sigma^2\,,\end{aligned} \quad \text{(C.9)}$$

where the functions χ_{0p}, χ_{1p}, χ_{2p} and ξ_{3p} and ξ_{4p} are recorded in the text, Eq. (5.26).

In this form it is easy to integrate over the phase space to determine the viscous stress

$$\pi^{\mu\nu} = \pi^{\mu\nu}_{(1)} + \pi^{\mu\nu}_{(2)} = \int_p \frac{p^\mu p^\nu}{p^0}\left(\delta f^{\sigma}_{(1)} + \delta f^{\sigma}_{(2)}\right)\,, \quad \text{(C.10)}$$

where $\pi^{\mu\nu}_{(1)}$ and $\pi^{\mu\nu}_{(2)}$ are given by static form of the constituent relation Eq. (5.1).

Rotational invariance in the rest frame reduces these tensor integrals, *e.g.*

$$\int_{\boldsymbol{p}} \chi_{0p} \frac{p^{\mu_1} p^{\mu_2} p^{\mu_3} p^{\mu_4}}{p^0} \langle O_{\mu_3\mu_3} \rangle = \left[\frac{2}{(d-1)(d+1)} \int_p \chi_{0p} \frac{p^4}{E_{\boldsymbol{p}}} \right] \langle O^{\mu_1\mu_2} \rangle \,, \tag{C.11}$$

yielding the equations for the transport coefficients written in the text, Eqs. (5.18), (5.23), and (5.24). In addition, we see that independent of the collision integral one finds the kinetic theory expectations identified in Ref. [110]

$$\lambda_2 = -2\eta\tau_\pi \,, \qquad \text{and} \qquad \lambda_3 = 0 \,. \tag{C.12}$$

Finally, in presenting these results in the text, and in implementing the results in a realistic hydrodynamic simulation, we have used the dynamic form of second order hydrodynamics, where $\pi^{\mu\nu}$ is treated as a dynamic variable. This choice amounts to using $-\pi_{\mu\nu}/\eta$ in place of $\sigma_{\mu\nu}$. In $\delta f^{\sigma}_{(2)}$ this reparameterization yields the replacements:

$$\langle D\sigma_{\mu_1\mu_2} \rangle + \frac{\sigma_{\mu_1\mu_2}}{d-1} \nabla \cdot u - 2 \left\langle \sigma^{\lambda}{}_{\mu_1} \Omega_{\mu_2\lambda} \right\rangle \to \frac{1}{\eta\tau_\pi} [\pi_{\mu_1\mu_2} + \eta\sigma_{\mu_1\mu_2}] - \frac{\lambda_1}{\eta\tau_\pi} \frac{1}{\eta^2} \left\langle \pi^{\lambda}{}_{\mu_1} \pi_{\mu_2\lambda} \right\rangle \,, \tag{C.13}$$

$$\langle \nabla_{\mu_1} \sigma_{\mu_2\mu_3} \rangle - 3 \langle \sigma_{\mu_1\mu_2} \nabla_{\mu_3} \ln T \rangle \to \frac{1}{\eta} \left[(d+2) \langle \pi_{\mu_1\mu_2} \nabla_{\mu_3} \ln T \rangle - \langle \nabla_{\mu_1} \pi_{\mu_2\mu_3} \rangle \right] \,, \tag{C.14}$$

and Eq. (C.8). In addition, when replacing $\sigma_{\mu\nu}$ with $-\pi_{\mu\nu}/\eta$ in the first order result, the difference $\frac{1}{\eta}(\pi_{\mu\nu} + \eta\sigma_{\mu\nu})$ must be appended to the second order result – see Eq. (5.14). The full result for $\delta f_{(1)}$ and $\delta f_{(2)}$ is given in Eqs. (5.15) and (5.25) respectively.

Appendix D

Convergence check of viscous hydrodynamic simulations

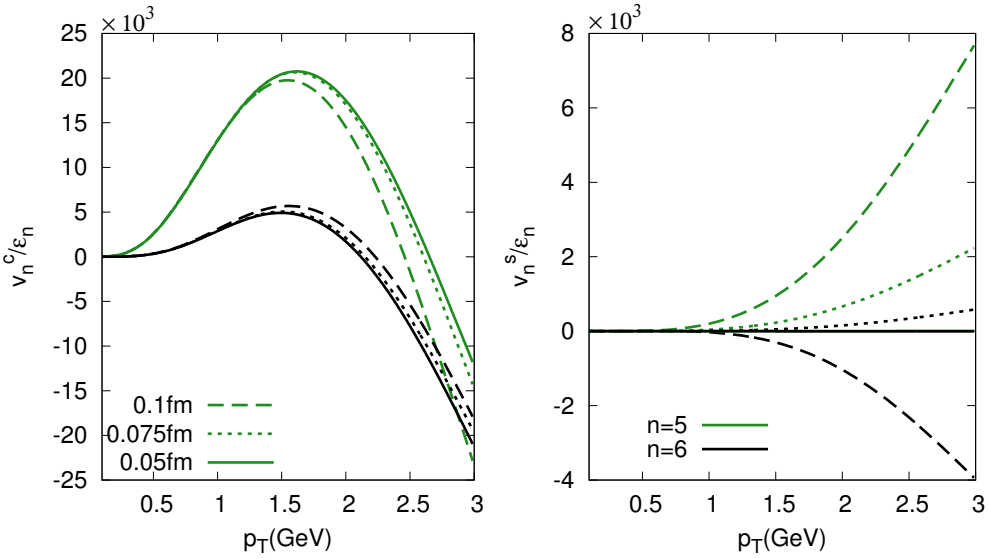

Figure D.1: Convergence of harmonic flow v_5 and v_6 in our numerical calculations. The grid sizes are set to be 0.1 fm, 0.075 fm and 0.05 fm for these three simulations. While v_n^c tends to converge (the left figure), the v_n^s approaches zero (the right figure).

To numerically solve the viscous hydrodynamic equations of motion Eq. (1.25) and (1.32), the medium system is simulated on grids, with $x_{i,j}^n$ referring the value of field x at discrete time t^n and grid point $(x, y) = (x_i, y_j)$. With a variant of central scheme discussed in [43, 114], the evolution of the hydrody-

namic system is reflected as the space-time description of hydrodynamic fields on these grids. In evaluating $\delta f_{(2)}$, unlike $\pi^{\mu\nu}$ is determined as the dynamic variable from the direct solutions, $\sigma^{\mu\nu}$ needs to be calculated as the derivatives of flow velocity. Consequently, the grid size Δx in our simulations largely affects the effect of $\delta f_{(2)}$ in the obtained harmonic flows, and the errors of our predictions.

In Fig. D.1, we carried out three different hydrodynamic simulations, with Δx varying from 0.1 fm, 0.075 fm to 0.05 fm, for the linear response of harmonic order $n = 5$ and $n = 6$. $v_n^c = \langle \cos n(\phi_p - \Psi_n) \rangle$ and $v_n^s = \langle \sin n(\phi_p - \Psi_n) \rangle$ are the generated flow projections into x-axis and y-axis. For these linear flow response, our initial state is deformed by cumulant with participant angle $\Phi_n = 0$. It is thus expect idealistically the generated flow is trivially aligned with $\Psi_n = 0$, *i. e.* $v_n^s = 0$. However, in Fig. D.1, only when Δx is reduced to 0.05 fm, the calculations are reliable in the sense that v_5^s and v_6^s approach zero. Also, this can be seen from the convergence of v_5^c and v_6^c as Δx decreases.

For a certain system size considered in the analysis, *e. g.* $\{r^2\}^{1/2} \sim 5$ fm for a mid-central Pb-Pb collision at LHC, the smaller grid size means more grid point involved in the simulation, which demands a much longer calculation time.

Bibliography

[1] J. Wambach, "Medium modification of hadrons," *Prog.Part.Nucl.Phys.* **61** (2008) 290–296.

[2] D. d'Enterria, "Perturbative probes of QCD matter at the Large Hadron Collider," *PoS* **QNP2012** (2012) 018, arXiv:1207.4362 [nucl-ex].

[3] **ALICE Collaboration** Collaboration, B. Abelev *et al.*, "Anisotropic flow of charged hadrons, pions and (anti-)protons measured at high transverse momentum in Pb-Pb collisions at $\sqrt{s_{NN}}$=2.76 TeV," *Phys.Lett.B* **719** (2013) 18–28, arXiv:1205.5761 [nucl-ex].

[4] C. Aidala, N. Ajitanand, Y. Akiba, Y. Akiba, R. Akimoto, *et al.*, "sPHENIX: An Upgrade Concept from the PHENIX Collaboration," arXiv:1207.6378 [nucl-ex].

[5] **ALICE Collaboration** Collaboration, K. Aamodt *et al.*, "Centrality dependence of the charged-particle multiplicity density at mid-rapidity in Pb-Pb collisions at $\sqrt{s_{NN}} = 2.76$ TeV," *Phys.Rev.Lett.* **106** (2011) 032301, arXiv:1012.1657 [nucl-ex].

[6] P. Huovinen and P. Petreczky, "QCD Equation of State and Hadron Resonance Gas," *Nucl.Phys.* **A837** (2010) 26–53, arXiv:0912.2541 [hep-ph].

[7] **ATLAS Collaboration** Collaboration, J. Jia, "Measurement of Event Plane Correlations in Pb-Pb Collisions at $\sqrt{s_{\rm NN}}$=2.76 TeV with the ATLAS Detector," arXiv:1208.1427 [nucl-ex].

[8] M. L. Miller, K. Reygers, S. J. Sanders, and P. Steinberg, "Glauber modeling in high energy nuclear collisions," *Ann.Rev.Nucl.Part.Sci.* **57** (2007) 205–243, arXiv:nucl-ex/0701025 [nucl-ex].

[9] W. Broniowski, M. Rybczynski, and P. Bozek, "GLISSANDO: GLauber Initial-State Simulation AND mOre.," *Comput. Phys. Commun.* **180** (2009) 69–83, arXiv:0710.5731 [nucl-th].

[10] D. Gross and F. Wilczek, "Ultraviolet Behavior of Nonabelian Gauge Theories," *Phys.Rev.Lett.* **30** (1973) 1343–1346.

[11] H. D. Politzer, "Reliable Perturbative Results for Strong Interactions?," *Phys.Rev.Lett.* **30** (1973) 1346–1349.

[12] S. Bethke, "Experimental tests of asymptotic freedom," *Prog.Part.Nucl.Phys.* **58** (2007) 351–386, arXiv:hep-ex/0606035 [hep-ex].

[13] J. Bjorken, "Asymptotic Sum Rules at Infinite Momentum," *Phys.Rev.* **179** (1969) 1547–1553.

[14] S. Scherer, "Introduction to chiral perturbation theory," *Adv.Nucl.Phys.* **27** (2003) 277, arXiv:hep-ph/0210398 [hep-ph].

[15] F. Karsch, "Lattice QCD at high temperature and density," *Lect.Notes Phys.* **583** (2002) 209–249, arXiv:hep-lat/0106019 [hep-lat].

[16] M. Stephanov, "QCD phase diagram: An Overview," *PoS* **LAT2006** (2006) 024, arXiv:hep-lat/0701002 [hep-lat].

[17] M. G. Alford, A. Schmitt, K. Rajagopal, and T. Schfer, "Color superconductivity in dense quark matter," *Rev.Mod.Phys.* **80** (2008) 1455–1515, arXiv:0709.4635 [hep-ph].

[18] E. Shuryak, "Physics of Strongly coupled Quark-Gluon Plasma," *Prog.Part.Nucl.Phys.* **62** (2009) 48–101, arXiv:0807.3033 [hep-ph].

[19] F. Karsch and E. Laermann, "Thermodynamics and in medium hadron properties from lattice QCD," arXiv:hep-lat/0305025 [hep-lat].

[20] D. J. Schwarz, "The first second of the universe," *Annalen Phys.* **12** (2003) 220–270, arXiv:astro-ph/0303574 [astro-ph].

[21] **STAR Collaboration** Collaboration, J. Adams *et al.*, "Experimental and theoretical challenges in the search for the quark gluon plasma: The STAR Collaboration's critical assessment of the evidence from RHIC collisions," *Nucl.Phys.* **A757** (2005) 102–183, arXiv:nucl-ex/0501009 [nucl-ex].

[22] B. Back, M. Baker, M. Ballintijn, D. Barton, B. Becker, *et al.*, "The PHOBOS perspective on discoveries at RHIC," *Nucl.Phys.* **A757** (2005) 28–101, arXiv:nucl-ex/0410022 [nucl-ex].

[23] **PHENIX Collaboration** Collaboration, K. Adcox *et al.*, "Formation of dense partonic matter in relativistic nucleus-nucleus collisions at RHIC: Experimental evaluation by the PHENIX collaboration," *Nucl.Phys.* **A757** (2005) 184–283, arXiv:nucl-ex/0410003 [nucl-ex].

[24] **BRAHMS Collaboration** Collaboration, I. Arsene *et al.*, "Quark gluon plasma and color glass condensate at RHIC? The Perspective from the BRAHMS experiment," *Nucl.Phys.* **A757** (2005) 1–27, arXiv:nucl-ex/0410020 [nucl-ex].

[25] N. Armesto, N. Borghini, S. Jeon, U. Wiedemann, S. Abreu, *et al.*, "Heavy Ion Collisions at the LHC - Last Call for Predictions," *J.Phys.* **G35** (2008) 054001, arXiv:0711.0974 [hep-ph].

[26] **Particle Data Group** Collaboration, S. Eidelman *et al.*, "Review of particle physics. Particle Data Group," *Phys.Lett.* **B592** (2004) 1.

[27] J. Bjorken, "Highly Relativistic Nucleus-Nucleus Collisions: The Central Rapidity Region," *Phys.Rev.* **D27** (1983) 140–151.

[28] A. Accardi, F. Arleo, N. Armesto, R. Baier, D. G. d'Enterria, *et al.*, "Hard probes in heavy ion collisions at the LHC: Jet physics," arXiv:hep-ph/0310274 [hep-ph].

[29] M. Bedjidian, D. Blaschke, G. T. Bodwin, N. Carrer, B. Cole, *et al.*, "Hard probes in heavy ion collisions at the LHC: Heavy flavor physics," arXiv:hep-ph/0311048 [hep-ph].

[30] J.-Y. Ollitrault, "Anisotropy as a signature of transverse collective flow," *Phys. Rev.* **D46** (1992) 229–245.

[31] D. Teaney, J. Lauret, and E. V. Shuryak, "Flow at the SPS and RHIC as a quark gluon plasma signature," *Phys.Rev.Lett.* **86** (2001) 4783–4786, arXiv:nucl-th/0011058 [nucl-th].

[32] P. F. Kolb and U. W. Heinz, "Emission angle dependent HBT at RHIC and beyond," *Nucl.Phys.* **A715** (2003) 653–656, arXiv:nucl-th/0208047 [nucl-th].

[33] P. F. Kolb, J. Sollfrank, and U. W. Heinz, "Anisotropic transverse flow and the quark hadron phase transition," *Phys.Rev.* **C62** (2000) 054909, arXiv:hep-ph/0006129 [hep-ph].

[34] **PHOBOS Collaboration** Collaboration, B. Alver *et al.*, "System size dependence of cluster properties from two-particle angular correlations in Cu+Cu and Au+Au collisions at s(NN)**(1/2) = 200-GeV," *Phys.Rev.* **C81** (2010) 024904, arXiv:0812.1172 [nucl-ex].

[35] **STAR Collaboration** Collaboration, B. Abelev *et al.*, "Long range rapidity correlations and jet production in high energy nuclear collisions," *Phys.Rev.* **C80** (2009) 064912, arXiv:0909.0191 [nucl-ex].

[36] **STAR Collaboration** Collaboration, B. Abelev *et al.*, "Three-particle coincidence of the long range pseudorapidity correlation in high energy nucleus-nucleus collisions," *Phys.Rev.Lett.* **105** (2010) 022301, arXiv:0912.3977 [hep-ex].

[37] **CMS Collaboration** Collaboration, S. Chatrchyan *et al.*, "Measurement of the elliptic anisotropy of charged particles produced in PbPb collisions at nucleon-nucleon center-of-mass energy = 2.76 TeV," *Phys.Rev.* **C87** (2013) 014902, arXiv:1204.1409 [nucl-ex].

[38] **ATLAS Collaboration** Collaboration, G. Aad *et al.*, "Measurement of the pseudorapidity and transverse momentum dependence of the elliptic flow of charged particles in lead-lead collisions at $\sqrt{s_{NN}} = 2.76$ TeV with the ATLAS detector," *Phys.Lett.* **B707** (2012) 330–348, arXiv:1108.6018 [hep-ex].

[39] **CMS Collaboration** Collaboration, S. Chatrchyan *et al.*, "Multiplicity and transverse-momentum dependence of two- and four-particle correlations in pPb and PbPb collisions," arXiv:1305.0609 [nucl-ex].

[40] **CMS Collaboration** Collaboration, S. Chatrchyan *et al.*, "Observation of long-range near-side angular correlations in proton-lead collisions at the LHC," *Phys.Lett.* **B718** (2013) 795–814, arXiv:1210.5482 [nucl-ex].

[41] D. Teaney, J. Lauret, and E. Shuryak, "A Hydrodynamic description of heavy ion collisions at the SPS and RHIC," arXiv:nucl-th/0110037 [nucl-th].

[42] P. F. Kolb and U. W. Heinz, "Hydrodynamic description of ultrarelativistic heavy ion collisions," arXiv:nucl-th/0305084 [nucl-th]. Invited review for 'Quark Gluon Plasma 3'. Editors: R.C. Hwa and X.N. Wang, World Scientific, Singapore.

[43] K. Dusling and D. Teaney, "Simulating elliptic flow with viscous hydrodynamics," *Phys.Rev.* **C77** (2008) 034905, arXiv:0710.5932 [nucl-th].

[44] H. Song and U. W. Heinz, " Causal viscous hydrodynamics in 2+1 dimensions for relativistic heavy-ion collisions," *Phys.Rev.* **C77** (2008) 064901, arXiv:0712.3715 [nucl-th].

[45] M. Luzum and P. Romatschke, "Conformal Relativistic Viscous Hydrodynamics: Applications to RHIC results at $\sqrt{s} = 200\,\mathrm{GeV}$," *Phys. Rev.* **C78** (2008) 034915, arXiv:0804.4015 [nucl-th].

[46] P. Danielewicz and M. Gyulassy, "Dissipative Phenomena in Quark Gluon Plasmas," *Phys.Rev.* **D31** (1985) 53–62.

[47] H.-T. Ding, A. Francis, O. Kaczmarek, F. Karsch, E. Laermann, *et al.*, "Thermal dilepton rate and electrical conductivity: An analysis of vector current correlation functions in quenched lattice QCD," *Phys.Rev.* **D83** (2011) 034504, arXiv:1012.4963 [hep-lat].

[48] G. Policastro, D. Son, and A. Starinets, "The Shear viscosity of strongly coupled N=4 supersymmetric Yang-Mills plasma," *Phys.Rev.Lett.* **87** (2001) 081601, arXiv:hep-th/0104066 [hep-th].

[49] P. Kovtun, D. Son, and A. Starinets, "Viscosity in strongly interacting quantum field theories from black hole physics," *Phys.Rev.Lett.* **94** (2005) 111601, arXiv:hep-th/0405231 [hep-th].

[50] D. Kharzeev and M. Nardi, "Hadron production in nuclear collisions at RHIC and high density QCD," *Phys.Lett.* **B507** (2001) 121–128, arXiv:nucl-th/0012025 [nucl-th].

[51] D. Kharzeev and E. Levin, "Manifestations of high density QCD in the first RHIC data," *Phys.Lett.* **B523** (2001) 79–87, arXiv:nucl-th/0108006 [nucl-th].

[52] D. Kharzeev, E. Levin, and M. Nardi, "The Onset of classical QCD dynamics in relativistic heavy ion collisions," *Phys.Rev.* **C71** (2005) 054903, arXiv:hep-ph/0111315 [hep-ph].

[53] S. A. Voloshin, "Two particle rapidity, transverse momentum, and azimuthal correlations in relativistic nuclear collisions and transverse radial expansion," *Nucl.Phys.* **A749** (2005) 287–290, arXiv:nucl-th/0410024 [nucl-th].

[54] B. Alver and G. Roland, "Collision geometry fluctuations and triangular flow in heavy-ion collisions," *Phys.Rev.* **C81** (2010) 054905, arXiv:1003.0194 [nucl-th].

[55] J. Takahashi *et al.*, "Topology studies of hydrodynamics using two particle correlation analysis," *Phys. Rev. Lett.* **103** (2009) 242301, arXiv:0902.4870 [nucl-th].

[56] P. Romatschke, "New Developments in Relativistic Viscous Hydrodynamics," *Int. J. Mod. Phys.* **E19** (2010) 1–53, arXiv:0902.3663 [hep-ph].

[57] U. W. Heinz and R. Snellings, "Collective flow and viscosity in relativistic heavy-ion collisions," arXiv:1301.2826 [nucl-th].

[58] L. D. Landau and E. M. Lifshits, *Fluid mechanics*. Pergamon Press, Oxford, England; New York, 1987.

[59] M. Laine and Y. Schroder, "Quark mass thresholds in QCD thermodynamics," *Phys.Rev.* **D73** (2006) 085009, arXiv:hep-ph/0603048 [hep-ph].

[60] M. Luzum and J.-Y. Ollitrault, "Constraining the viscous freeze-out distribution function with data obtained at the BNL Relativistic Heavy Ion Collider (RHIC)," *Phys.Rev.* **C82** (2010) 014906, arXiv:1004.2023 [nucl-th].

[61] S. De Groot, e. Van Leeuwen, W.A., and C. Van Weert, "Relativistic Kinetic Theory. Principles and Applications,".

[62] W. Israel, "Nonstationary irreversible thermodynamics: A Causal relativistic theory," *Annals Phys.* **100** (1976) 310–331.

[63] R. Baier, P. Romatschke, D. T. Son, A. O. Starinets, and M. A. Stephanov, "Relativistic viscous hydrodynamics, conformal invariance, and holography," *JHEP* **0804** (2008) 100, arXiv:0712.2451 [hep-th].

[64] D. Teaney, "Chemical freezeout in heavy ion collisions," arXiv:nucl-th/0204023 [nucl-th].

[65] F. Cooper and G. Frye, "Comment on the Single Particle Distribution in the Hydrodynamic and Statistical Thermodynamic Models of Multiparticle Production," *Phys.Rev.* **D10** (1974) 186.

[66] D. Teaney, "The Effects of viscosity on spectra, elliptic flow, and HBT radii," *Phys.Rev.* **C68** (2003) 034913, arXiv:nucl-th/0301099 [nucl-th].

[67] J. Sollfrank, P. Koch, and U. W. Heinz, "The Influence of resonance decays on the P(t) spectra from heavy ion collisions," *Phys.Lett.* **B252** (1990) 256–264.

[68] J. Sollfrank, P. Koch, and U. W. Heinz, "Is there a low p(T) 'anomaly' in the pion momentum spectra from relativistic nuclear collisions?," *Z.Phys.* **C52** (1991) 593–610.

[69] D. Teaney and L. Yan, "Triangularity and Dipole Asymmetry in Heavy Ion Collisions," *Phys.Rev.* **C83** (2011) 064904, arXiv:1010.1876 [nucl-th].

[70] D. Teaney and L. Yan, "Non linearities in the harmonic spectrum of heavy ion collisions with ideal and viscous hydrodynamics," *Phys.Rev.* **C86** (2012) 044908, arXiv:1206.1905 [nucl-th].

[71] D. Teaney and L. Yan, "Non-linear flow response and reaction plane correlations," *Nucl.Phys.A904-905* **2013** (2013) 365c–368c, arXiv:1210.5026 [nucl-th].

[72] D. Teaney and L. Yan, "Second order viscous corrections to the harmonic spectrum in heavy ion collisions," arXiv:1304.3753 [nucl-th].

[73] B. H. Alver, C. Gombeaud, M. Luzum, and J.-Y. Ollitrault, "Triangular flow in hydrodynamics and transport theory," *Phys. Rev.* **C82** (2010) 034913, arXiv:1007.5469 [nucl-th].

[74] **STAR** Collaboration, P. Sorensen, "Higher Flow Harmonics in Heavy Ion Collisions from STAR," *J. Phys.* **G38** (2011) 124029, arXiv:1110.0737 [nucl-ex].

[75] **PHENIX** Collaboration, A. Adare *et al.*, "Measurements of Higher-Order Flow Harmonics in Au+Au Collisions at $\sqrt{s_{\rm NN}} = 200\,\text{GeV}$," *Phys. Rev. Lett.* **107** (2011) 252301, arXiv:1105.3928 [nucl-ex].

[76] **ALICE Collaboration** Collaboration, F. Noferini, "Anisotropic flow of identified particles in Pb-Pb collisions at $\sqrt{s_{NN}} = 2.76$ TeV measured with ALICE at the LHC," *Nucl.Phys.A904-905* **2013** (2013) 483c–486c, arXiv:1212.1292 [nucl-ex].

[77] **ALICE** Collaboration, K. Aamodt *et al.*, "Higher harmonic anisotropic flow measurements of charged particles in Pb-Pb collisions at 2.76 TeV," *Phys. Rev. Lett.* **107** (2011) 032301, arXiv:1105.3865 [nucl-ex].

[78] **ATLAS Collaboration** Collaboration, G. Aad *et al.*, "Measurement of the azimuthal anisotropy for charged particle production in $\sqrt{s_{NN}} = 2.76$ TeV lead-lead collisions with the ATLAS detector," *Phys.Rev.* **C86** (2012) 014907, arXiv:1203.3087 [hep-ex].

[79] B. Schenke, S. Jeon, and C. Gale, "Elliptic and triangular flow in event-by-event (3+1)D viscous hydrodynamics," *Phys. Rev. Lett.* **106** (2011) 042301, arXiv:1009.3244 [hep-ph].

[80] H. Petersen, G.-Y. Qin, S. A. Bass, and B. Muller, "Triangular flow in event-by-event ideal hydrodynamics in Au+Au collisions at $\sqrt{s_{\rm NN}} = 200A$ GeV," *Phys. Rev.* **C82** (2010) 041901, arXiv:1008.0625 [nucl-th].

[81] J. Xu and C. M. Ko, "Triangular flow in heavy ion collisions in a multiphase transport model," *Phys.Rev.* **C84** (2011) 014903, arXiv:1103.5187 [nucl-th].

[82] **ALICE Collaboration** Collaboration, S. A. Voloshin, "Results on flow from the ALICE Collaboration," *Nucl.Phys.A904-905* **2013** (2013) 90c–97c, arXiv:1211.5680 [nucl-ex].

[83] J. Jia and D. Teaney, "Study on initial geometry fluctuations via participant plane correlations in heavy ion collisions: part II," arXiv:1205.3585 [nucl-ex].

[84] J. Jia and S. Mohapatra, "A Method for studying initial geometry fluctuations via event plane correlations in heavy ion collisions," arXiv:1203.5095 [nucl-th].

[85] Z. Qiu and U. W. Heinz, "Event-by-event shape and flow fluctuations of relativistic heavy-ion collision fireballs," *Phys.Rev.* **C84** (2011) 024911, arXiv:1104.0650 [nucl-th].

[86] B. Schenke, P. Tribedy, and R. Venugopalan, "Fluctuating Glasma initial conditions and flow in heavy ion collisions," *Phys.Rev.Lett.* **108** (2012) 252301, arXiv:1202.6646 [nucl-th].

[87] Z. Qiu and U. Heinz, "Hydrodynamic event-plane correlations in Pb+Pb collisions at $\sqrt{s} = 2.76$ATeV," *Phys.Lett.* **B717** (2012) 261–265, arXiv:1208.1200 [nucl-th].

[88] E. Retinskaya, M. Luzum, and J.-Y. Ollitrault, "Directed flow at midrapidity in $\sqrt{s_{NN}} = 2.76$ TeV Pb+Pb collisions," *Phys.Rev.Lett.* **108** (2012) 252302, arXiv:1203.0931 [nucl-th].

[89] **ALICE Collaboration** Collaboration, B. Abelev *et al.*, "Directed flow of charged particles at mid-rapidity relative to the spectator plane in Pb-Pb collisions at $\sqrt{s_{NN}}$=2.76 TeV," arXiv:1306.4145 [nucl-ex].

[90] **STAR Collaboration** Collaboration, Y. Pandit, "Dipole asymmetry at $\sqrt{s_{NN}} = 200$ GeV Au+Au Collisions from STAR experiment at RHIC," arXiv:1211.7162 [nucl-ex].

[91] J. Jia, "Measurement of elliptic and higher order flow from ATLAS experiment at the LHC," *J. Phys.* **G38** (2011) 124012, arXiv:1107.1468 [nucl-ex].

[92] P. Staig and E. Shuryak, "The Fate of the Initial State Fluctuations in Heavy Ion Collisions. III The Second Act of Hydrodynamics," *Phys.Rev.* **C84** (2011) 044912, arXiv:1105.0676 [nucl-th].

[93] R. S. Bhalerao, M. Luzum, and J.-Y. Ollitrault, "Understanding anisotropy generated by fluctuations in heavy-ion collisions," *Phys.Rev.* **C84** (2011) 054901, arXiv:1107.5485 [nucl-th].

[94] H.-J. Drescher and Y. Nara, "Eccentricity fluctuations from the Color Glass Condensate at RHIC and LHC," *Phys. Rev.* **C76** (2007) 041903, arXiv:0707.0249 [nucl-th].

[95] F. G. Gardim, F. Grassi, M. Luzum, and J.-Y. Ollitrault, "Mapping the hydrodynamic response to the initial geometry in heavy-ion collisions," *Phys.Rev.* **C85** (2012) 024908, arXiv:1111.6538 [nucl-th].

[96] N. Borghini and J.-Y. Ollitrault, "Momentum spectra, anisotropic flow, and ideal fluids," *Phys.Lett.* **B642** (2006) 227–231, arXiv:nucl-th/0506045 [nucl-th].

[97] S. S. Gubser and A. Yarom, "Conformal hydrodynamics in Minkowski and de Sitter spacetimes," *Nucl.Phys.* **B846** (2011) 469–511, arXiv:1012.1314 [hep-th].

[98] **STAR Collaboration** Collaboration, B. Abelev *et al.*, "Charge Independent(CI) and Charge Dependent(CD) correlations as a function of Centrality formed from Delta phi imum Delta eta Charged Pair Correlations in Minimum Bias Au+Au Collisions at s(NN)**(1/2) = 200-GeV," arXiv:0806.0513 [nucl-ex].

[99] **STAR Collaboration** Collaboration, B. Abelev *et al.*, "Azimuthal Charged-Particle Correlations and Possible Local Strong Parity Violation," *Phys.Rev.Lett.* **103** (2009) 251601, arXiv:0909.1739 [nucl-ex].

[100] **STAR Collaboration** Collaboration, B. Abelev *et al.*, "Observation of charge-dependent azimuthal correlations and possible local strong parity violation in heavy ion collisions," *Phys.Rev.* **C81** (2010) 054908, arXiv:0909.1717 [nucl-ex].

[101] D. Kharzeev, R. Pisarski, and M. H. Tytgat, "Possibility of spontaneous parity violation in hot QCD," *Phys.Rev.Lett.* **81** (1998) 512–515, arXiv:hep-ph/9804221 [hep-ph].

[102] C. Gombeaud and J.-Y. Ollitrault, "Effects of flow fluctuations and partial thermalization on v_4," *Phys. Rev.* **C81** (2010) 014901, arXiv:0907.4664 [nucl-th].

[103] K. Dusling, G. D. Moore, and D. Teaney, "Radiative energy loss and v(2) spectra for viscous hydrodynamics," *Phys.Rev.* **C81** (2010) 034907, arXiv:0909.0754 [nucl-th].

[104] T. A. Collaboration, "Measurement of reaction plane correlations in Pb-Pb collisions at $\sqrt{s_{\rm NN}}$=2.76 TeV," May, May, 2012. ATLAS-CONF-2012-049. See also https://cdsweb.cern.ch/record/1451882.

[105] M. Luzum and J.-Y. Ollitrault, "The event-plane method is obsolete," *Phys.Rev.* **C87** (2013) 044907, arXiv:1209.2323 [nucl-ex].

[106] S. A. Voloshin, A. M. Poskanzer, and R. Snellings, "Collective phenomena in non-central nuclear collisions," arXiv:0809.2949 [nucl-ex].

[107] R. S. Bhalerao, M. Luzum, and J.-Y. Ollitrault, "Determining initial-state fluctuations from flow measurements in heavy-ion collisions," *Phys.Rev.* **C84** (2011) 034910, arXiv:1104.4740 [nucl-th].

[108] **ALICE Collaboration** Collaboration, A. Bilandzic, "Anisotropic flow measured from multi-particle azimuthal correlations for Pb-Pb collisions at 2.76 TeV by ALICE at the LHC," *Nucl.Phys.A904-905* **2013** (2013) 515c–518c, arXiv:1210.6222 [nucl-ex].

[109] **ATLAS Collaboration** Collaboration, J. Jia, "Measurement of the distributions of event-by-event flow harmonics in Pb-Pb Collisions at $\sqrt{s_{\rm NN}}$=2.76 TeV with the ATLAS detector," arXiv:1209.4232 [nucl-ex].

[110] M. A. York and G. D. Moore, "Second order hydrodynamic coefficients from kinetic theory," *Phys.Rev.* **D79** (2009) 054011, arXiv:0811.0729 [hep-ph].

[111] R. Baier, P. Romatschke, D. T. Son, A. O. Starinets, and M. A. Stephanov, "Relativistic viscous hydrodynamics, conformal invariance, and holography," *JHEP* **0804** (2008) 100, arXiv:0712.2451 [hep-th].

[112] D. Teaney, "Finite temperature spectral densities of momentum and R-charge correlators in N=4 Yang Mills theory," *Phys.Rev.* **D74** (2006) 045025, arXiv:hep-ph/0602044 [hep-ph].

[113] M. Luzum and J.-Y. Ollitrault, "Extracting the shear viscosity of the quark-gluon plasma from flow in ultra-central heavy-ion collisions," *Nucl.Phys.A* (2012) , arXiv:1210.6010 [nucl-th].

[114] L. Pareschi, "Central differencing based numerical schemes for hyperbolic conservation laws with relaxation terms," *SIAM Journal on Numerical Analysis* **39** no. 4, (2001) 1395–1417, http://epubs.siam.org/doi/pdf/10.1137/S0036142900375906. http://epubs.siam.org/doi/abs/10.1137/S0036142900375906.

[115] G. Denicol and H. Niemi, "Derivation of transient relativistic fluid dynamics from the Boltzmann equation for a multi-component system," arXiv:1212.1473 [nucl-th].

[116] H. Song, S. A. Bass, U. Heinz, T. Hirano, and C. Shen, "Hadron spectra and elliptic flow for 200 A GeV Au+Au collisions from viscous

hydrodynamics coupled to a Boltzmann cascade," *Phys.Rev.* **C83** (2011) 054910, arXiv:1101.4638 [nucl-th].

[117] **ALICE Collaboration** Collaboration, B. Abelev *et al.*, "Long-range angular correlations on the near and away side in p-Pb collisions at $\sqrt{s_{NN}} = 5.02$ TeV," *Phys.Lett.* **B719** (2013) 29–41, arXiv:1212.2001 [nucl-ex].

[118] **ATLAS Collaboration** Collaboration, G. Aad *et al.*, "Observation of Associated Near-side and Away-side Long-range Correlations in $\sqrt{s_{NN}} = 5.02$ TeV Proton-lead Collisions with the ATLAS Detector," arXiv:1212.5198 [hep-ex].

[119] P. Bozek and W. Broniowski, "Correlations from hydrodynamic flow in p-Pb collisions," *Phys.Lett.* **B718** (2013) 1557–1561, arXiv:1211.0845 [nucl-th].

[120] **PHENIX Collaboration** Collaboration, A. Adare *et al.*, "Quadrupole anisotropy in dihadron azimuthal correlations in central d+Au collisions at $\sqrt{s_{NN}} = 200$ GeV," arXiv:1303.1794 [nucl-ex].

[121] E. Shuryak and I. Zahed, "High Multiplicity pp and pA Collisions: Hydrodynamics at its Edge and Stringy Black Hole," arXiv:1301.4470 [hep-ph].

[122] A. Bzdak, B. Schenke, P. Tribedy, and R. Venugopalan, "Initial state geometry and the role of hydrodynamics in proton-proton, proton-nucleus and deuteron-nucleus collisions," arXiv:1304.3403 [nucl-th].